Analysis of the molecular and physiological influence of WNT1 on the skeleton

Dissertation

zur Erlangung des akademischen Grades eines

PhD

an der

Medizinischen Fakultät der Universität Hamburg

vorgelegt von

Wenbo Zhao

aus

Kunming, Volksrepublik China

2024

Betreuer:in / Gutachter:in der Dissertation: Prof. Dr. Thorsten Schinke

Gutachter:in der Dissertation: PD Dr. Dr. Tim Rolvien

Vorsitz der Prüfungskommission: Prof. Dr. Thorsten Schinke

Mitglied der Prüfungskommission: PD Dr. Dr. Tim Rolvien

Mitglied der Prüfungskommission: Prof. Dr. Meliha Karsak

Datum der mündlichen Prüfung: 19.12.2024

Contents

1. Introduction

In the bodies of vertebrate animals, bone is a highly specialized tissue with complex developmental and metabolic processes. Bone modeling and remodeling are critical to the integrity of skeleton and are tightly integrated with many biological functions within the skeleton as well as other organs [1-4].

1.1 Bone remodeling

Bone remodeling is an essential physiological activity for maintaining the skeleton. During bone remodeling, old or damaged bone packets that need to be replaced are resorbed by osteoclasts, a cell type that originates from the fusion of progenitor cells of the monocyte/macrophage lineage. This is followed by the subsequent synthesis of fresh bone matrix by osteoblasts, cells that derive from the mesenchymal lineage [5-7]. Bone remodeling is occurring continuously throughout the life of the organism, thus ideally maintaining a constant bone quality. During bone remodeling, bone resorption and formation are coupled and balanced. A disturbance of this balance can lead to skeletal disorders such as osteoporosis [8-10]. Based on previous studies [11-13] and our findings described in detail below, WNT1 is a key regulator of bone remodeling.

1.2 WNT-signaling and bone metabolism

WNT-signaling is a highly complex signaling pathway that will only be briefly summarized in the following passage. For a more detailed description, readers are referred to the following references including my medical doctoral dissertation [14-17].

Generally, WNT-signaling is classified into three distinct pathways: the canonical WNT-signaling pathway and the noncanonical pathways including the WNT-planar cell polarity (WNT-PCP) pathway and the WNT-calcium (WNT-Ca^{2+}) pathway [15,18].

Canonical WNT-signaling is initiated by the binding of a WNT ligand with a transmembrane co-receptor from the low-density lipoprotein receptor-related protein (LRP) family and a main receptor of the frizzled (FZD) family. Upon activation of canonical WNT-signaling, degradation of β-catenin is inhibited and it accumulates in cytoplasm. Subsequently, β-catenin translocates into the nucleus, where it activates the TCF/LEF transcription factors, thus enabling the transcription of WNT-signaling target genes [15,19].

Noncanonical WNT-signaling requires the binding of WNT ligands to FZD receptors as well. However, the intracellular signal transduction is independent of β-catenin [15]. The planar cell polarity pathway (WNT-PCP pathway) is able to regulate cellular behaviours such as planar cell polarity, cell movement during gastrulation and neural crest cell migration [15]. The WNT-calcium pathway (WNT/Ca^{2+} pathway) is characterized by release of calcium from endoplasmic reticulum to cytoplasma, subsequently regulating cellular activities such as cell adhesion and migration [15,17].

There are extracellular factors regulating WNT-signaling. For instance, the secreted frizzled-related proteins (SFRPs) and WNT inhibitory factor 1 (WIF1) are able to directly sequester WNT ligands to inhibit WNT signaling [15]. Other antagonists, such as SOST and DKK1, can bind the transmembrane co-receptor LRP5/6, preventing the formation of the receptor complex and thus suppressing WNT-signaling [15,20].

Dysfunctions of WNT-signaling can result in several diseases including skeletal disorders. For instance, inactivating mutations of *LRP5* can cause osteoporosis-pseudoglioma syndrome (OPPG) [15,21]. In contrast, pathogenic loss-of-function mutations of *SOST* (encoding the WNT-inhibitor sclerostin), can lead to sclerosteosis or Van Buchem disease (VBD) that are characterized by pathologically high bone mass [15,22].

1.3 Identification of WNT1 as a potent osteoanabolic factor

WNT1, a member of the WNT ligand family, has been found to play important roles in regulating numerous biological activities including bone remodeling [12,13]. It has been demonstrated that WNT1 has a strong bone anabolic effect [23]. Inactivating mutations of WNT1 can result in early-onset osteoporosis (EOOP) or osteogenesis imperfecta (OI) type VX in humans, highlighting the clinical relevance of this ligand [24-27]. The respective phenotypes have additionally been recapitulated in corresponding mouse models. A previous study performed in our department revealed that a heterozygous R235W mutation of *Wnt1* in mice caused EOOP which mimics the EOOP phenotype in human patients carrying the same mutation, while the homozygous mutation in mice was able to significantly reduce the trabecular and cortical bone mass at a younger age [24]. Another study from our group reported that a homozygous G177C mutation of *Wnt1*, which leads to OI type VX in humans, was able to specifically cause an OI phenotype in mice [25]. Moreover, a previous study from our department revealed that osteoblast-specific induction of *Wnt1* increased bone mass significantly and rapidly, whereas the osteoblast-specific deletion of *Wnt1* led to severely reduced bone mass and spontaneous fractures [23]. Thus, it is apparent that WNT1 is essential for skeletal integrity.

However, the detailed mechanism of the osteoanabolic function of WNT1 is still unclear. The investigation of the mechanism is particularly valuable, since this can provide more insights into the WNT-signaling system, and potentially contribute to the development of novel treatments for skeletal disorders.

In previous experiments that were part of my medical doctoral thesis, I found that a recombinant WNT1/SFRP1 complex was able to significantly promote osteogenesis in ST2 cells, a mesenchymal stem cell line derived from mouse bone marrow [28]. Furthermore, *Omd* and *Postn* were among the highest induced genes upon short-term WNT1 stimulation. POSTN was previously reported to be important in maintaining cortical microstructure *in vivo* [29,30]. Interestingly, OMD was reported to be able to reduce the diameter and variability of collagen I fibrils during assembly *in vitro* [31], which indicates that OMD is possibly a regulator of collagen fibrils during bone formation. Therefore, I hypothesized that OMD and POSTN could potentially be relevant downstream targets of WNT1. Since the potential functions of OMD had not been analyzed *in vivo* at the beginning of the study, one major goal of the present thesis was to analyze the skeletal phenotype of *Omd*-deficient mice and their response to the osteoanabolic influence of WNT1.

Moreover, another important question regarding the molecular function of WNT1 is the identity of the relevant receptor. When comparing the gene expression of all frizzled receptors after the stimulation with reWNT1/SFRP1, *Fzd4* was the most suppressed one. Based on the negative feedback pattern, I speculated that FZD4 may be the receptor for WNT1. This notion is further supported by the observation that FZD4 can regulate bone mass in mice [32]. Therefore, the second aim of this thesis was to determine if FZD4 is the receptor for WNT1.

In addition, recombinant WNT1 only has a biological activity in complex with SFRP1. Although SFRP1 is generally considered as an antagonist of WNT-signaling, it was also reported to contribute to the solubility of WNT1 [33]. Therefore, another aim of this thesis is to investigate if SFRP1 is necessary for the bone-anabolic function of WNT1 *in vivo*.

1.4 Current knowledge about Osteomodulin (OMD)

1.4.1 Identification and distribution of OMD

Osteomodulin (OMD) belongs to the small leucine-rich repeat proteoglycan (SLRP) family [34] and was isolated and identified for the first time from bovine bone in 1998 [35]. It was named osteoadherin (OSAD) at that time since it was able to bind hydroxyapatite and promote osteoblast attachment *in vitro* [35].

Numerous subsequent studies have investigated the distribution and expression pattern of OMD. *In situ* hybridization detected OMD mRNA in osteoblasts on the trabecular bone surface when analyzing fetal calf growth plate from fetlock joints, with the strongest signal in mature osteoblasts on well-developed trabeculae [34]. Similarly, in femoral trabecular bone of fetal and postnatal young rat, OMD mRNA could be detected in osteoblasts on trabecular surfaces, with the strongest expression at the interface between cartilage and bone [36]. This finding was consistent with immunohistochemical analyses that detected OMD predominantly in trabecular bone, with the highest level at the bone-cartilage interface [36,37]. In addition, OMD was also detected in osteocytes in cortical bone of mouse tibia [38]. During endochondral ossification of embryonic mouse metatarsal, immunostaining revealed that OMD appeared first within the forming bone collar, especially at the endosteal osteoid surface. At the postnatal stage, OMD was mainly localized in primary spongiosa and osteoid surface in developing bone, while it could be observed throughout the mineralized bone matrix in adult mouse metatarsal [39]. Collectively, in bone tissue, OMD is primarily expressed by mature osteoblasts in trabecular bone and located in the mineralized bone matrix [34,36,37,39].

OMD was also detected in other skeletal sites in several species. In calf, OMD was observed in the mineralized dentin matrix, cementum and surrounding alveolar bone at the age of 1.5 years [40]. In developing mouse teeth, OMD was detected in the predentin layer at the mineralization front at protein level [41]. In rats, *Omd* gene expression was detected by *in situ* hybridization in alveolar bone in embryos and the teeth of new born ones. In the teeth it started in polarized odontoblasts and increased in secretory and mature odontoblasts [42]. In older rats, immunostaining indicated that OMD was distributed in extracellular matrix and odontoblasts of the incisor [40]. Likewise, in third molar germs of humans, OMD expression was detected in mature odontoblasts [42].

OMD is not solely localized in bone and dental tissues. On the one hand, OMD was detected in plasma and has been found in kidney, vessel and bladder [43-46]. On the other hand, during our own assessment of the *Omd* expression pattern, we have observed relatively high expression in tissues other than bone, including lung, thyroid gland and visceral fat (Fig.3 upper panel). The variable expression pattern is also reported in the NCBI database, with relatively high *Omd* expression in bladder and embryonic limb and central nervous system [47].

1.4.2 Function of OMD

An *in vitro* study demonstrated that OMD was capable to suppress the rate and extent of type I collagen fibril formation. Furthermore, OMD could suppress the formation of twisted collagen fibrils. As a consequence, OMD was able to reduce the diameter and variability of type I collagen fibrils [31]. The authors further investigated the molecular basis and found that the weak electrostatic forces between OMD and type I collagen were responsible for their interaction, which enables the assembly of collagen fibrils with an optimal diameter and shape [48]. The findings indicate that OMD might be a regulator of collagen I fibrillogenesis during bone formation, which was an important basis of my investigation.

Since OMD is characterized by its presence in mineralized tissues, it was speculated that OMD plays a role in bone and dentin formation. Accordingly, numerous studies were performed regarding this hypothesis in the past years.

The expression pattern of OMD during osteogenic differentiation has already been thoroughly explored to explore the function of OMD. In MC3T3-E1 cells, mouse calvarial osteoblasts, and human and rat dental pulp stem cells, *Omd* expression was upregulated during osteogenic differentiation [38,41,49,50].

Interestingly, OMD overexpression in MC3T3-E1 cells led to increased mineralization capacity after 2 or 3 weeks of osteogenic differentiation [51]. However, in another study, transient overexpression of *Omd* was not able to alter the expression of *Alpl* and *Bglap*. After 14 days of osteogenic differentiation following transient *Omd* overexpression, ALPL activity was not changed [49].

On the contrary, *in vitro* studies demonstrated that the knockdown or silencing of *Omd* by siRNA or shRNA resulted in significantly decreased expression of osteogenesis relevant genes (*Dmp1*, *Alpl* and *Dspp*) and transcription factors (*Sp7*, *Runx2* and *Dlx5*) during osteogenic differentiation in human dental pulp stem cells [50,52]. Furthermore, the mineralization capacity of *Omd*-knocked-down and -silenced cells was both significantly reduced [50,52].

These findings support that OMD promotes osteogenesis. However, all of them are *in vitro* investigations.

An *in vivo* study revealed that bone resorption regulated by osteoclasts may be able to induce OMD expression [38]. More specifically, in the *op*/*op* mouse line which displays osteopetrosis phenotype due to deficiency of osteoclasts caused by an M-CSF defect [53,54], Cathepsin K was significantly reduced. This phenotype could be rescued by MCS-F treatment, which led to increased osteoclast activity accompanied by OMD expression in the surroundings which was comparable to the physiological condition, indicating that the OMD induction is likely to occur during the coupled bone formation process [38].

Moreover, OMD might be involved with proliferation and apoptosis of MC3T3-E1 cells [49]. Administration of recombinant mouse OMD to MC3T3-E1 cells at 10nM was able to significantly suppress cell viability and proliferation as measured by an MTT assay [51].

A recent study explored the interaction of OMD with BMP2. Co-administration of OMD and BMP2 significantly promotes the expression induction of *Sp7* and *Alpl* compared to BMP2 alone in human dental pulp stem cells [50]. Since previous studies indicated that *Omd* might be a downstream target of BMP2 [38,55], the authors further investigated the interaction of OMD with BMP2 and proposed a potential mechanism that OMD is able to bind BMP2 and facilitate the anchoring of BMP2 to its receptors on cell surface, thus promoting BMP/SMAD signaling [50].

Of note, all these studies were not able to determine the *in vivo* function of OMD. Only recently, when most of the practical investigations of this thesis were already completed, a study was published where the *in vivo* function of OMD was explored for the first time in skeleton. The researchers observed that OMD deficiency moderately altered bone microstructure and had a potential protective effect against osteoarthritis (OA) in mice [56].

OMD is not only expressed in bone and dental matrix. OMD was found to induce osteogenic-like microenvironment of renal interstitium, subsequently contributing to the formation of Randall's plaques [43]. A recent study revealed that OMD is associated with cardiovascular calcification and widely upregulated in both plasma and local tissue. OMD is potentially an important early modulator of cardiovascular calcification processes, where OMD expression could be increased by inflammation of the vessel wall and osteogenic transition of smooth muscle cells and be able to attenuate calcification of extracellular matrix [44]. OMD protein and mRNA levels are associated with plaque calcification in atherosclerosis in humans. High *Omd* levels were associated with fewer cardiovascular events during follow-up for patients after carotid plaques removal by endarterectomy. Moreover, the OMD mRNA level was associated with plaque stability [45]. Besides, OMD is potentially an endogenous inhibitor of bladder cancer initiation and progression [46].

1.5 Aims of the thesis

Since the *in vivo* function of OMD as a potential WNT1 downstream target had not been previously analyzed, the major goal of the present thesis was to analyze the skeletal phenotype of *Omd*-deficient mice and their response to transgenic overexpression of WNT1 in osteoblasts. In accompanying studies, it was also addressed if SFRP1 is required for the osteoanabolic function of

WNT1 *in vivo*, and if FZD4 (or FZD2) are relevant WNT1 receptors in osteoblasts.

2. Materials and Methods

2.1 Materials

2.1.1 Equipment

Equipment	Model/Version	Manufacturer
Affymetrix GeneChip Fluidics Station	450	Affymetrix, Santa Clara, US
Affymetrix GeneChip Scanner	3000 7G	Affymetrix, Santa Clara, US
Agilent 2200 TapeStation System	2200	Agilent Technologies, Inc., Santa Clara, US
Analytical balance	CPA224S	Sartorius AG, Göttingen, DE
Analytical balance	TE2101	Sartorius AG, Göttingen, DE
Atomic force microscopy probe	HQ:NSC15/AlBS	MikroMasch, Sofia, BG
Backscattered electron detector	Type 202	K.E. Developments Ltd., Cambridge, UK
Camera	EOS 200D	Canon Inc., Tokyo, JP
Camera lens	50mm 1:2.8 Macro	Sigma Corp., Kawasaki, JP
Cell culture incubator	BBD 6220	Heraeus GmbH, Hanau, DE
Centrifuge	GS-6	Beckman Coulter Inc., Brea, US
Centrifuge	5415D	Eppendorf AG, Hamburg, DE
Centrifuge	5430R	Eppendorf AG, Hamburg, DE
Centrifuge	5425	Eppendorf AG, Hamburg, DE
Class II biological safety cabinet	MSC-Advantage™	Thermo Fisher Scientific Inc., Waltham, US
Cold light platform	LP5000K	Hama GmbH & Co. KG, Monheim, DE
Electrophoresis cell	Sub-Cell GT	Bio-Rad Laboratories, Inc., Hercules, US

Equipment	Model/Version	Manufacturer
Incubation bath	1012	GFL Gesellschaft für Labortechnik GmbH, Burgwedel, DE
Incubator shaker	Innova 4000	New Brunswick Scientific Co., Inc., Edison Township, US
Level atomic force microscopy system	/	Anfatec Instruments AG, Oelsnitz, DE
Magnetic Stirrer	RCT Basic	IKA GmbH & Co. KG, Staufen im Breisgau, DE
MicroCT scanner	µCT 40	Scanco Medical AG, Brüttisellen, CH
Microplate reader	VersaMax™	Molecular Devices, San Jose, US
Microprocessor controlled power supply	200/2.0	Bio-Rad Laboratories, Inc., Hercules, US
Microscope	Axioskop	Carl Zeiss AG, Oberkochen, DE
Microscope	IX50	Olympus Corp., Tokyo, JP
Microscope	BX53	Olympus Corp., Tokyo, JP
Microscope system	EVOS™ M5000	Invitrogen Corp., Waltham, US
Molecular Imager ChemiDoc™ XRS System	170-8070	Bio-Rad Laboratories, Inc., Hercules, US
Nanoindenter	iMicro	KLA Corporation, Milpitas, US
PCR cycler	Msastercycler® pro S	Eppendorf AG, Hamburg, DE
Precision balance	440-33	Kern & Sohn GmbH, Balingen, DE
Scanner	G4050	HP Inc., Palo Alto, US
Scanning electron microscope	LEO 435	LEO Microscopy Ltd., Cambridge, UK
Shaker	Duomax 1030	Heidolph Instruments GmbH & Co. KG, Schwabach, DE

Equipment	Model/Version	Manufacturer
Spectrophotometer	ND1000	PEQLAB Biotechnologie GmbH, Erlangen, DE
StepOnePlus Real-Time PCR System	StepOnePlus	Applied Biosystems Inc., Waltham, US
Thermomixer	Thermomixer comfort	Eppendorf AG, Hamburg, DE
Tube roller	RS-TR05	Phoenix Instrument GmbH, Garbsen, DE
Vilber E-box Imaging system	VX2	Vilber, Marne-la-Vallée, FR
Western-Blotting system	Mini Gel Tank system	Thermo Fisher Scientific Inc., Waltham, US
Western-Blotting system	Mini Bolt Module	Thermo Fisher Scientific Inc., Waltham, US
X-ray cabinet	621/96	Faxitron, Tucson, US
X-ray film processor	1170-1-0000	PROTEC GmbH & Co. KG, Oberstenfeld, DE

2.1.2 Consumables

Consumables	Manufacturer
100 Sterican® needles	B. Braun Melsungen AG, Melsungen, DE
1.5 ml SafeSeal micro tube	Sarstedt AG & Co. KG, Nürmbrecht, DE
2.0 ml SafeSeal micro tube	Sarstedt AG & Co. KG, Nürmbrecht, DE
Biosphere® Filter Tips 0.1-10µl	Sarstedt AG & Co. KG, Nürmbrecht, DE
Biosphere® Filter Tips 100-1000µl	Sarstedt AG & Co. KG, Nürmbrecht, DE
Biosphere® Filter Tips 2-100µl	Sarstedt AG & Co. KG, Nürmbrecht, DE
Biosphere® Filter Tips 2-20µl	Sarstedt AG & Co. KG, Nürmbrecht, DE
Bolt™ Bis-Tris Plus Mini Protein Gels, 4-12%, 1.0 mm	Invitrogen Corp., Waltham, US
Cell culture flask, 250 ml, 75cm^2	Greiner Bio-One GmbH, Kremsmünster, AT

Consumables	Manufacturer
Cell culture plate (12- and 24-well format)	Greiner Bio-One GmbH, Kremsmünster, AT
Clariom™ D Assay, mouse (REF: 902513)	Thermo Fisher Scientific Inc., Waltham, US
Screw cap Falcon tube, 50ml	Sarstedt AG & Co. KG, Nürmbrecht, DE
Screw cap Falcon tube, 25ml	Sarstedt AG & Co. KG, Nürmbrecht, DE
Filtration cup (PES membrane, 0.2 µm)	Th. Geyer GmbH & Co. KG, Renningen, DE
Injekt®-F	B. Braun Melsungen AG, Melsungen, DE
MicroAmp™ Fast Optical 96-Well Reaction Plate	Thermo Fisher Scientific Inc., Waltham, US
Microtiter plate	Sarstedt AG & Co. KG, Nürmbrecht, DE
Nitrocellulose transfer membrane 0.45µm pore size	Schleicher & Schuell Inc., Keene, US
PCR SingleCap 8-pack SoftStrips 0.2ml	Biozym Scientific GmbH, Hessisch Oldendorf, DE
PCR SoftStrips 12, 0.2 ml	Biozym Scientific GmbH, Hessisch Oldendorf, DE
Quality Pipette Tips 0.1-10 µl	Sarstedt AG & Co. KG, Nürmbrecht, DE
Quality Pipette Tips 100-1000µl	Sarstedt AG & Co. KG, Nürmbrecht, DE
Quality Pipette Tips 2-200µl	Sarstedt AG & Co. KG, Nürmbrecht, DE
Sarstedt® cells craper	Sarstedt AG & Co. KG, Nürmbrecht, DE
Serological pipette 5ml	Sarstedt AG & Co. KG, Nürmbrecht, DE
Serological pipette 10ml	Sarstedt AG & Co. KG, Nürmbrecht, DE
Serological pipette 25ml	Sarstedt AG & Co. KG, Nürmbrecht, DE
Slide-A-Lyzer™ G2 Dialysis Cassette	Thermo Fisher Scientific Inc., Waltham, US

2.1.3 Chemicals

Chemical name	Abbreviation	Molecular formula	Manufacturer
Acetic Acid		CH_3COOH	Carl Roth GmbH & Co. KG, Karlsruhe, DE
Alizarin Red S		$C_{14}H_7NaO_7S$	Sigma-Aldrich Corp., St. Louis, US
Ammonium hydroxide		NH_4OH	Sigma-Aldrich Corp., St. Louis, US
Diethyl pyrocarbonate	DEPC	$C_6H_{10}O_5$	Sigma-Aldrich Corp., St. Louis, US
Dimethyl sulfoxide	DMSO	$(CH_3)_2SO$	Carl Roth GmbH & Co. KG, Karlsruhe, DE
Ethylenediaminetetra acetic acid	EDTA	$C_{10}H_{16}N_2O_8$	Sigma-Aldrich Corp., St. Louis, US
Ethanol	EtOH	C_2H_6O	Merck KGaA, Darmstadt, DE
Ethidium bromide	EtBr	$C_{21}H_{20}BrN_3$	Sigma-Aldrich Corp., St. Louis, US
Guanidine·HCl		$CH_5N_3 \cdot HCl$	SERVA Electrophoresis GmbH, Heidelberg, DE
Isopropanol		C_3H_8O	Carl Roth GmbH & Co. KG, Karlsruhe, DE
L-Ascorbic acid	ASC	$C_6H_8O_6$	Sigma-Aldrich Corp., St. Louis, US
Methanol	MeOH	CH_3OH	Carl Roth GmbH & Co. KG, Karlsruhe, DE

Chemical name	**Abbreviation**	**Molecular formula**	**Manufacturer**
Phenol/Chloroform/Isoamyl alcohol			Carl Roth GmbH & Co. KG, Karlsruhe, DE
Tris(hydroxymethyl)aminomethane	Tris	$(HOCH_2)_3CNH_2$	Carl Roth GmbH & Co. KG, Karlsruhe, DE
Tween 20		$C_{58}H_{114}O_{26}$	Carl Roth GmbH & Co. KG, Karlsruhe, DE
β-glycerophosphate	β-Gly	$C_3H_9O_6P$	Sigma-Aldrich Corp., St. Louis, US
β-mercaptoethanol	βME	$HOCH_2CH_2SH$	Sigma-Aldrich Corp., St. Louis, US

2.1.4 Reagents

Reagents	Manufacturer
Bio-Rad Protein Assay Dye Reagent Concentrate (Bradford reagent, REF: 5000006)	Bio-Rad Laboratories, Inc., Hercules, US
Biozym LE Agarose (REF: 840004)	Biozym Scientific GmbH, Hessisch Oldendorf, DE
Bovine Serum Albumin lyophilized powder, REF: A9418-100G)	Sigma-Aldrich Corp., St. Louis, US
Collagenase (REF: C9891-1G)	Sigma-Aldrich Corp., St. Louis, US
cOmplete™ Protease Inhibitor Cocktail Tablets (REF: 04693124001)	Roche AG, Basel, CH
Dispase® II (neutral protease, grade II, REF: 04942078001)	Roche AG, Basel, CH
Fzd2 endoribonuclease-prepared siRNA (esiRNA, REF: EMU073051)	Sigma-Aldrich Corp., St. Louis, US
Gibco™ Fetal Bovine Serum (FBS, REF: A5670701)	Fisher Scientific International, Inc. Pittsburgh, US
Gibco™ Penicillin-Streptomycin (10,000 U/mL, REF: 15140122)	Fisher Scientific International, Inc. Pittsburgh, US
Minimum Essential Medium Eagle (powder, REF: M0643-1L)	Sigma-Aldrich Corp., St. Louis, US
PhosSTOP™ Phosphatase Inhibitor Cocktail Tablets (REF: 04906837001)	Roche AG, Basel, CH
Pierce™ Bovine Serum Albumin Standard (2mg/ml, REF: 23210)	Thermo Fisher Scientific Inc., Waltham, US
Pierce™ ECL Plus Western Blotting Substrate (REF: 32132)	Thermo Fisher Scientific Inc., Waltham, US
Pierce™ ECL Western Blotting Substrate (REF: 32109)	Thermo Fisher Scientific Inc., Waltham, US
Proteinase K (REF: P9290)	Sigma-Aldrich Corp., St. Louis, US
Recombinant Mouse WNT1/SFRP1 Complex Protein (reWNT1/SFRP1, REF: 9765-WN)	R&D Systems, Minneapolis, US
Recombinant Mouse SFRP1 Protein (reSFRP1, REF: 9019-SF)	R&D Systems, Minneapolis, US
Recombinant Murine WNT3a (reWNT3a, REF: 315-20)	PeproTech, Cranbury, US
Recombinant Mouse WNT5a Protein (reWNT5a, REF: 645-WN)	R&D Systems, Minneapolis, US

Reagents	Manufacturer
Silencer™ Select Negative Control No.1 siRNA (REF: 4390843)	Thermo Fisher Scientific Inc., Waltham, US
TaqMan™ Gene Expression Master Mix (REF: 4369014)	Applied Biosystems Inc., Waltham, US
Gibco™ Trypsin-EDTA (0.25%), phenol red (REF: 25200056)	Fisher Scientific International, Inc. Pittsburgh, US

2.1.5 Solutions and buffers

Name	Composition
Digestion buffer (for isolation of calvarial osteoblasts)	For each use: αMEM -/- medium 30ml (details indicated below) 1mg/ml collagenase (Sigma-Aldrich Corp., St. Louis, US) 2mg/ml dispase (Dispase® II, Roche AG, Basel, CH)
TAE buffer (50×)	2M Tris-Base 1M acetic acid 100mM EDTA Ad dH_2O pH=8.5 (adjust with HCl if necessary)
Alizarin red staining solution	40mM Alizarin red S in H_2O, pH=4.1~4.2
Bolt™ MES SDS Running Buffer (20×, REF: B0002)	Obtained from Life Technologies, Carlsbad, US
Bolt™ Transfer Buffer (20×, REF: BT00061)	Obtained from Life Technologies, Carlsbad, US
Calcein solution	0.25% (w/v) calcein
NuPAGE™ LDS Sample Buffer (4×, REF: NP0007)	Obtained from Life Technologies, Carlsbad, US
Ponceau S solution	0.1% (w/v) Ponceau S 5% (v/v) acetic acid, ad H_2O
Re-Blot Plus Strong Antibody Stripping Solution (REF: 2504)	Obtained from Merck Millipore, Burlington, US
RIPA buffer	10mM Tris-HCl (pH=8.0) 1mM EDTA 0.1% Sodium Deoxycholate 0.1% SDS 150mM NaCl, ad dH_2O

Name	Composition
Tail Lysis Buffer	50mM Tris-HCl (pH=8.5) 100mM NaCl 2.5mM EDTA 0.1% SDS Ad dH_2O
αMEM -/- medium	Minimum Essential Medium Eagle (powder fits for 1L medium, Sigma-Aldrich Corp., St. Louis, US) $NaHCO_3$ 2.2g/L medium Ad dH_2O to 1L Filtered in clean bench with Filtration cup, PES membrane, 0.2 µm (Th. Geyer GmbH & Co. KG, Renningen, DE)
αMEM +/+ medium	α MEM -/- medium described above Supplemented with: 10% v/v Gibco™ Fetal Bovine Serum (FBS, Fisher Scientific International, Inc. Pittsburgh, US) 1% v/v antibiotics (Gibco™ Penicillin-Streptomycin (10,000 U/mL, Fisher Scientific International, Inc. Pittsburgh, US)

2.1.6 Commercial Kits

Kit name	Manufacturer
Phire Animal Tissue Direct PCR Kit (REF: F140WH)	Thermo Fisher Scientific Inc., Waltham
Lipofectamine™ 2000 Kit (REF: L3000001)	Invitrogen Corp., Waltham, US
Lipofectamine™ RNAiMAX Transfection Reagent (REF: 13778075)	Thermo Fisher Scientific Inc., Waltham, US
Macherey-Nagel NucleoSpin RNA/Protein Kit (REF: 740933)	Macherey-Nagel, GmbH & Co. KG, Düren, DE
peqGOLD TriFast Kit (REF: 30-2010)	PEQLAB Biotechnologies GmbH, Erlangen, DE
Verso cDNA Synthesis Kit (REF: AB1453A)	Thermo Fisher Scientific Inc., Waltham, US

Kit name	Manufacturer
GeneChip™ WT PLUS Reagent Kit (REF: 902280)	Thermo Fisher Scientific Inc., Waltham, US

2.1.7 Genotyping primers

Primer	Sequence
Omd WT and KO	WT For (5’ GAT GCC CTG GAA CTT ACT ATG C 3’) WT Rev (5’ GTA CTC CCT CGG CCA CTA TCT GC 3’) KO For (5’ TCC CCC ATT GTC TCA TGT CC 3’) KO Rev (5’ GCA GCG CAT CGC CTT CTA TC 3’)
Wnt1Tg	For (5’ CGC CAA AAA CAT AAA GAA AGG C 3’) Rev (5’ TGT CCC TAT CGA AGG ACT CTG G 3’)
ColtTA	For (5’ CTC TGC ACC TTG GTG ATC 3’) Rev (5’ GCT GCT TAA TGA GGT CGG 3’)
Sfrp1 WT and KO	WT For (5’ TCC GTT CCT CGT CTA TCC TG 3’) WT Rev (5’ GAT TGA TTT TCC CTG GCT CA 3’) KO For (5’ CTT GGG TGG AGA GGC TAT TC 3’) KO Rev (5’ AGG TGA GAT GAC AGG AGA TC 3’)
Fzd4 floxed	Fzd4-fl For v3 (5’ GCA CGT CTC ACC TGA AAG AGA 3’) Fzd4-fl Rev v2 (5’ TCT TGG TCA CGT TGT AGC CG 3’)
CMV-Cre	Cre-F (5’ ACT GGG ATC TTC GAA CTC TTT GGA C 3’) Cre-R (5’ GAT GTT GGG GCA CTG CTC ATT CAC C 3’) Cre-CreF (5’ CCA TCT GCC ACC AGC CAG 3’) Cre-CreR (5’ TCG CCA TCT TCC AGC AGG 3’)
Fzd4 WT and KO	WT For (5’ CAG CTG ACA ACT TTC ACG CC 3’) WT Rev (5’ CTG GAA GGG CGA AGT TCT GT 3’) Fzd4 loxP For v2 (5’ TGT AAA CCC CAA ATA CCG TG 3’) Fzd4 loxP Rev v2 (5’ CGT ATA ATG TAT GCT ATA CGA AG 3’)

2.1.8 TaqMan probes

Gene	Catalog number
Gapdh	4352661
Alpl	Mm00475834_m1
Apcdd1	Mm01257559_m1
Aspn	Mm00445945_m1
Bglap	Mm03413826_mH
Col1a1	Mm00801666_g1

Gene	Catalog number
Fzd2	Mm02524776_s1
Omd	Mm00449589_m1
Postn	Mm00450111_m1
Runx2	Mm00501580_m1
Sp7	Mm00504574_m1
Tnfsf11	Mm00441908_m1
Tnfrsf11b	Mm00435454_m1
Wnt16	Mm00446420_m1

2.1.9 Primary and secondary antibodies for Western-Blotting

Antibody	Source	Dilution	Manufacturer	Product number
OMD (Mouse Osteoadherin/OSAD Antibody)	Goat	1:1666 in 5% BSA in TBST	R&D Systems, Minneapolis, US	AF3308
β-actin Antibody	Rabbit	1:1000 in 5% w/v nonfat dry milk	Cell Signaling Technology, Danvers, US	#4967
Polyclonal Rabbit Anti-Goat Immunoglobulins/HRP	Rabbit	1:1000 in 5% BSA in TBST	Dako GmbH, Hovedstaden, DK	P0449
Polyclonal Goat Anti-Rabbit Immunoglobulins/HRP	Goat	1:2000 in 5% BSA in TBST	Dako GmbH, Hovedstaden, DK	P0448

2.1.10 Software

Software	Version	Manufacturer
Microsoft Office 2010	16.0	Microsoft Corp., Redmond, US
EndNote	X7	Thomson ResearchSoft, Stanford, US
GraphPad Prism	9.2.0	GraphPad Software Inc. San Diego, US
StepOne™ Software	2.3	Applied Biosystems Inc., Waltham, US
Bioquant Osteo	23.5.6	BIOQUANT Image Analysis Corp., Nashville, US
ImageJ	1.54f (OrientationJ Plugin v2.0.5)	National Institutes of Health, Bethesda, US

Software	Version	Manufacturer
MATLAB	R2022a	The MathWorks, Inc., Natick, US
MicroCT Analysis Software	4.05	Scanco Medical AG, Brüttisellen, CH
Olympus cellSens Dimension software	V4.1	Olympus Corp., Tokyo, JP
Osteomeasure Software	4.3.0	OsteoMetrics, Inc., Decatur, US
Quantity One Software	4.6.9	Bio-Rad Laboratories, Inc., Hercules, US
TestXpert III software	V1.5	ZwickRoell GmbH & Co. KG, Ulm, DE
Transcriptome Analysis Console (TAC) Software	4.0	Thermo Fisher Scientific Inc., Waltham, US

2.2 Methods

2.2.1 Animals and animal husbandry

The *Omd*-deficient mice (B6;129S5-*Omd*^{tm1Lex}/Uke) were obtained as frozen sperm from the MMRRC repository (Stock Number: 011749-UCD) and revitalized in the animal facility at University Medical Center Hamburg-Eppendorf according to standard protocols. The mice were bred on a C57Bl6/J background. *Omd* coding exons 1 and 2 were targeted by homologous recombination in the mouse line with gene trap technique in embryonic stem cells by the MMRRC-contributor Lexicon Pharmaceuticals, Inc. (The Woodlands, US).

Calcein injection was utilized to measure the bone formation rate for 6-week-old female *Omd*-deficient mice and the littermate controls. Calcein solution was injected intraperitoneally with the dose of 10mg/kg whole body mass (i.e. 0.1ml solution/25g body mass). Afterwards the animal welfare was assessed and scored by daily investigation of overall appearance and body mass until sacrifice. Calcein labelling was performed 9 and 2 days prior to sacrifice respectively.

The previously established mouse line carrying osteoblast-specific inducible *Wnt1* transgene (*Wnt1*Tg mouse line [23]) was utilized to investigate the effect of OMD on the osteoanabolic function of WNT1. This mouse line was crossed with the *Omd*-deficient mice to generate the *Wnt1*Tg/*Omd*-deficient mouse line (STOCK-Tg(tetO-*Wnt1*,-luc)TWNTLach-Tg(Col1a1-tTa)139Niss-*Omd*^{tm1Lex}/Uke).

Sfrp1-deficient mouse line was obtained from the Jackson Laboratory (line number: 023209) as living mice. The *Sfrp1*-deficient mouse line was then crossed with the *Wnt1*Tg mouse line to generate *Wnt1*Tg/*Sfrp1*-deficient mouse line (B6-Tg(tetO-Wnt1,-luc)TWNTLach-Tg(Col1a1-tTa)139Niss-*Sfrp1*$^{\mathrm{tm1Jrbn}}$/Uke).

To generate *Fzd4*-deficient mice, first, the *Fzd4*-floxed mouse line was obtained from the Jackson Laboratory (line number: 011078) as living mice. Then the mice which were homozygous for *Fzd4* loxP site were crossed with the mouse line obtained from our animal stock carrying a CMV-Cre recombinase, thus generating the heterozygous *Fzd4*-deficient mice. The heterozygous *Fzd4*-deficient mice were crossed with *Wnt1*Tg mice to get *Wnt1*Tg/*Fzd4*-deficient mouse line (B6;129-Tg(tetO-Wnt1,-luc)TWNTLach-Tg(Col1a1-tTa)139Niss-*Fzd4*$^{\mathrm{tm2.1dNat}}$/UKE).

All mice were housed in a specific pathogen-free environment with a 12-hour light/dark cycle, 45% to 65% relative humidity and temperature in the range of 20 °C to 24 °C in open or individually ventilated cages with proper nesting materials and at maximum 6 mice per cage. The mice had *ad libitum* access to tap water and standard rodent chow (1328P, Altromin Spezialfutter GmbH & Co. KG, Lage, DE). For the mice which carried the osteoblast-specific inducible *Wnt1* transgene, the diet always contained doxycycline (ssniff-Spezialdiäten GmbH, Soest, DE) to suppress the transgene expression. Their diet was switched from doxycycline-containing food to standard chow for 1 week or 3 weeks to induce the transgenic *Wnt1* gene.

Genotyping was performed for all new-born mice to verify the genotypes as described below in the section Genotyping with the primers indicated above in the section Genotyping primers. The number of animals per group was 1 to 7, with the exact number presented by the individual data points in corresponding figures.

All animal experiments were approved by the animal facility of the University Medical Center Hamburg-Eppendorf and by the “Behörde für Soziales, Familie, Gesundheit und Verbraucherschutz” (Org869, Org1091, N022/2022, N003/2021) in accordance with the local implementation of EU Directive 2010/63/EU for animal experiments. No unexpected adverse events were observed during the research.

2.2.2 Genotyping

The genotypes of mice were verified by polymerase chain reaction (PCR) and agarose gel electrophoresis. DNA was extracted from tail biopsies from newborn mice using Phire Animal Tissue Direct PCR Kit (Thermo Fisher Scientific Inc., Waltham, US; for each sample, 20µl Dilution Buffer and 0.5µl DNA Release Additive were added) at room temperature for 5min followed by an incubation of 2 min at 98°C. For Fzd4 WT and KO genotyping PCR, the tail biopsies were fully lysed with Tail Lysis Buffer and proteinase K at 55°C for at least 6 hours, followed by DNA extraction with phenol/chloroform and isopropanol. Afterwards, the purified DNA was dissolved in water and used for genotyping PCR.

The sequences of the PCR primers are listed in the section “Genotyping primers” above. The detailed PCR protocols and thermocycler settings are listed in Table 1 to Table 8.

Table 1. Omd genotyping PCR protocol

Omd WT and KO					
Component	Volume (μl)	PCR Program			
H_2O	6.2	Initialization	94°C	4 min	
10× Dream Taq Green Buffer	2	Denaturation	94°C	40 sec	40 cycles
DMSO	1.5	Annealing	55°C	40 sec	
dNTPs (10mM)	1	Elongation	72°C	1 min	
Primer 1 (WT For or KO For, 2μM)	4	Last Elongation	72°C	10 min	
Primer 2 (WT Rev or KO Rev, 2μM)	4	Store	4°C		
Dream Taq DNA Polymerase	0.3	Target bands: WT=218bp, KO=286bp			
DNA	1 (≈50ng)				
Total	20				

Table 2. Wnt1Tg genotyping PCR protocol

Wnt1Tg					
Component	Volume (μl)	PCR Program			
H_2O	12.5	Initialization	94°C	4 min	
10× Dream Taq Green Buffer	2.5	Denaturation	94°C	30 sec	40 cycles
DMSO	0.25	Annealing	52°C	40 sec	
dNTPs (10mM)	0.5	Elongation	72°C	1 min	
Primer 1 (Wnt1-Luc For, 2μM)	4	Last Elongation	72°C	10 min	
Primer 2 (Wnt1-Luc Rev, 2μM)	4	Store	4°C		
Dream Taq DNA Polymerase	0.25	Target band: 500bp			
DNA	1 (≈50ng)				
Total	25				

Table 3. ColtTA genotyping PCR protocol

ColtTA

Component	Volume (µl)
H_2O	12.5
10× Dream Taq Green Buffer	2.5
DMSO	0.25
dNTPs (10mM)	0.5
Primer 1 (Col-tTA For, 2µM)	4
Primer 2 (Col-tTA Rev, 2µM)	4
Dream Taq DNA Polymerase	0.25
DNA	1 (≈50ng)
Total	25

PCR Program			
Initialization	94°C	5 min	
Denaturation	94°C	30 sec	35 cycles
Annealing	60°C	30 sec	
Elongation	72°C	30 sec	
Last Elongation	72°C	7 min	
Store	4°C		
Target band: 550bp			

Table 4. Sfrp1 genotyping PCR protocol

Sfrp1 WT and KO

Component	Volume (µl)
H_2O	2.2
10× Dream Taq Green Buffer	2
DMSO	1.5
dNTPs (10mM)	1
Primer 1 (WT For, 2µM)	3
Primer 2 (KO For, 2µM)	3
Primer 3 (WT Rev, 2µM)	3
Primer 4 (KO Rev, 2µM)	3
Dream Taq DNA Polymerase	0.3
DNA	1 (≈50ng)
Total	20

PCR Program			
Initialization	94°C	4 min	
Denaturation	94°C	40 sec	40 cycles
Annealing	58°C	40 sec	
Elongation	72°C	1 min	
Last Elongation	72°C	10 min	
Store	4°C		
Target bands: WT=486bp, KO=280bp			

Table 5. Fzd4 floxed genotyping PCR protocol

Fzd4 floxed

Component	Volume (µl)
H_2O	12.8
10× Dream Taq Green Buffer	2
DMSO	0.5
dNTPs (10mM)	1
Primer 1 (Fzd4-fl For v3, 2µM)	1.2
Primer 2 (Fzd4-fl Rev v2, 2µM)	1.2
Dream Taq DNA Polymerase	0.3
DNA	1 (≈50ng)
Total	20

PCR Program			
Initialization	94°C	4 min	
Denaturation	94°C	30 sec	40 cycles
Annealing	56°C	30 sec	
Elongation	72°C	1 min	
Last Elongation	72°C	10 min	
Store	4°C		
Target bands: WT=812bp, Floxed=862bp Final results were confirmed by Sanger Sequencing.			

Table 6. CMV-Cre genotyping PCR protocol

CMV-Cre

Component	Volume (µl)
H_2O	15.7
10× Dream Taq Green Buffer	2.5
DMSO	0
dNTPs (10mM)	0.5
Primer 1 (Cre-F, 2µM)	1.25
Primer 2 (Cre-R, 2µM)	1.25
Primer 3 (Cre-CreF, 2µM)	1.25
Primer 4 (Cre-CreR, 2µM)	1.25
Dream Taq DNA Polymerase	0.3
DNA	1 (≈50ng)
Total	25

PCR Program			
Initialization	95°C	3 min	
Denaturation	95°C	30 sec	35 cycles
Annealing	62°C	30 sec	
Elongation	72°C	1 min	
Last Elongation	72°C	10 min	
Store	4°C		
Target bands: WT=420bp, Mutant=281bp			

Table 7. Fzd4 WT genotyping PCR protocol

Fzd4 WT

Component	Volume (μl)
H_2O	8.5
10× Dream Taq Green Buffer	2
DMSO	1
dNTPs (10mM)	1
Primer 1 (Fzd4 WT For, 2μM)	3
Primer 2 (Fzd4 WT Rev, 2μM)	3
Dream Taq DNA Polymerase	0.5
DNA	1 (≈50ng)
Total	20

PCR Program			
Initialization	94°C	4 min	
Denaturation	94°C	30 sec	40 cycles
Annealing	57°C	40 sec	
Elongation	72°C	1 min	
Last Elongation	72°C	10 min	
Store	4°C		
Target band: 468bp			

Table 8. Fzd4 KO genotyping PCR protocol

Fzd4 KO

Component	Volume (μl)
H_2O	8.5
10× Dream Taq Green Buffer	2
DMSO	1
dNTPs (10mM)	1
Primer 1 (Fzd4 loxP For v2, 2μM)	3
Primer 2 (Fzd4 loxP Rev v2, 2μM)	3
Dream Taq DNA Polymerase	0.5
DNA	1 (≈50ng)
Total	20

PCR Program			
Initialization	94°C	4 min	
Denaturation	94°C	30 sec	45 cycles
Annealing	50°C	40 sec	
Elongation	72°C	1 min	
Last Elongation	72°C	10 min	
Store	4°C		
Target band: 587bp			

Electrophoresis was done on a 1% agarose gel in TAE buffer with EtBr (10mg/ml stock, final concentration:0.5mg/L), at the voltage of 120V for 25 minutes. A DNA ladder (GeneRuler 1kb Plus DNA Ladder, Thermo Fisher Scientific Inc., Waltham, US) was used for identifying the size of PCR products and the gels were visualized with ultraviolet light by using the Vilber E-box Imaging system (Vilber, Marne-la-Vallée, FR).

Given that PCR products of *Fzd4* floxed genotyping protocol have very similar sizes, the genotype was determined by Sanger sequencing. The PCR products were purified using NucleoSpin™ Gel and PCR Clean-up Kit (Macherey-Nagel, GmbH & Co. KG, Düren, DE) according to the manufacturer’s guidelines followed by concentration measurement with spectrophotometer (ND-1000, PEQLAB Biotechnologie GmbH, Erlangen, DE). Then the samples were sent to Microsynth AG (Balgach, CH) for Sanger Sequencing.

2.2.3 Preparation of mouse organ and skeleton

Mice were anesthetized with a mixture of 20% O_2 and 80% CO_2 and subsequently euthanized with 100% CO_2.

For gene expression analysis in different tissues, 8-week-old female C57Bl6/J wildtype mice were sacrificed and multiple tissues were obtained, including skin, muscle, lung, kidney, heart, aorta, liver, brain, spinal cord, thyroid gland, spleen, thymus, stomach, duodenum, colon, visceral fat, subcutaneous fat, brown fat, bone marrow, vertebral body and femur.

For skeletal analysis, female *Omd*-deficient mice and wildtype littermate controls were sacrificed at the age of 6 or 12 or 24 weeks, while male mice were analyzed at the age of 12 weeks. When investigating the influence of Omd deficiency on the bone anabolic function of WNT1, female *Wnt1*Tg*/Omd*-deficient mouse were sacrificed at 12 weeks old, before which they had been switched to doxycycline-free diet for 1 or 3 weeks or maintained on the doxycycline-containing diet.

To investigate the influence of SFRP1 and FZD4 on the bone anabolic function of WNT1, *Wnt1*Tg/*Sfrp1*-deficient mice were sacrificed at the age of 12 weeks, before which the diet had been switched to doxycycline-free type for 1 week or maintained as doxycycline-containing type, while the *Wnt1*Tg/*Fzd4*-deficient mice were sacrificed at 5 weeks old, with or without the switch of diet for 1 week.

After the mice were euthanized as described above, body mass was measured with an electronic balance (440-33, Kern & Sohn GmbH, Balingen, DE). Then blood samples were obtained via heart-puncture with a syringe. Afterwards, serum was collected after 8min of centrifugation at 6,000rcf. The skin and organs in thoracic and abdominal cavities were removed with the skeleton undamaged. Mice were fully stretched and fixed on cork-boards, followed by fixation in 3.7% PBS-buffered formaldehyde for 48h, after which the skeletons were transferred into 80% ethanol for temporary storage. Contact radiographs were performed using an X-ray cabinet (35kV, 2s, Faxitron, Tucson, US). X-ray films (AGFA Corp., Mortsel, NL) were developed with an automated X-ray processor (PROTEC GmbH & Co. KG, Oberstenfeld, DE). X-rays were scanned using a scanner (V850 pro, Epson, Nagano, JP), on which the body length was measured, counting from the bottom of the skull to the beginning site of tail. Tibiae and femora and the lumbar spines (L1 to L4) were isolated without damaging the structure. For 12-week-old female *Omd*-deficient mice and wildtype controls, humeri and the whole skulls were removed from the skeleton. All bone samples were stored in 80% ethanol until further analysis.

2.2.4 Micro-computed tomography (micro-CT/µCT)

µCT scanning and analysis were performed on a µCT 40 desktop cone-beam microCT system (Scanco Medical AG, Brüttisellen, CH) at 55kVp, 145µA based on the established protocol [24]. The voxel resolution was 10µm. Femora, tibiae, humeri, skulls and subsequently calvariae were scanned separately. The Scanco MicroCT software suite (v6.5-2, Scanco Medical AG, Brüttisellen, CH) was used for evaluation. The trabecular bone of femora was analyzed in the distal metaphysis in a volume situated 2500µm to 500µm proximal of the distal growth plate. The cortical bone of femora was analyzed in a volume with a length of 1000µm situated in the middle of the femoral diaphysis. Tibial cortical bone was measured in a 1000µm long section located centrally between the distal end of proximal growth plate and the proximal start of distal tibiofibular connection. For humeri, cortical parameters were determined in a 1000µm long section beginning 500µm distal of the diaphyseal midpoint, which avoids the most irregular cortex. Inner and outer diameters of cortical bone were calculated from total tissue area and cortical thickness based on a circular shape as the modeling basis for all bone types. The skulls were scanned in full with an FOV value of 30mm and analyzed first for calvarial thickness, which was measured by ImageJ on segmented 3D reconstruction models of the skulls on the coronal plane at the second turn of the cochleae. To enable more accurate and efficient analysis of calvarial porosity, the complete calvariae were isolated from the skulls and then scanned along the axis of sagittal suture. Calvarial porosity was subsequently determined in a volume with a length of 3000µm on the right parietal bone, excluding any sutures at the medial and lateral edges. All 3D visualizations were generated by Scanco MicroCT software suite.

2.2.5 Histology and histologic staining

The formalin-fixed right tibiae and lumbar spines (L1 to L4) of mice were dehydrated by ascending ethanol concentrations. Then the bones were embedded in methyl methacrylate. Sectioning and staining were performed as routine by the histology technicians of the Department of Osteology and Biomechanics. Sections of 4μm thickness were cut in the sagittal (tibia) or coronal (spine) plane and stained by von Kossa/van Gieson or Toluidine blue staining. The right femora from 6-week-old female *Omd*-deficient mice and wildtype controls were treated in the same way and sections of 12μm thickness were cut in the transversal plane at mid-shaft without any staining, which was used for the dynamic histomorphometry to measure cortical bone formation rate as described below.

2.2.6 Histomorphometric analysis

Structural histomorphometry was performed using sections of tibiae and lumbar spines after von Kossa/van Gieson staining with Bioquant Osteo software (BIOQUANT Image Analysis Corp., Nashville, US). Semi-automated quantifications with standard settings of the trabecular bone compartment were performed on images of sections taken at 1.25× magnification. For the lumbar spine, the mean values for parameters obtained in the trabecular compartments of vertebral body L3 and L4 were used for further analysis. For tibiae, the trabecular bone region distal of the proximal growth plate was quantified, of which the length along the tibial axis was approximately equal to the length of the proximal growth plate. These parameters were obtained: trabecular bone volume (BV/TV, bone volume/tissue volume), trabecular number (Tb.N), trabecular thickness (Tb.Th) and trabecular separation (Tb.Sp).

For the measurement of growth plate thickness, tibia sections with Toluidine blue staining from 12-week-old female *Omd*-deficient mice and littermate controls were analyzed with Osteomeasure software (OsteoMetrics, Inc., Decatur, US) in a blinded fashion according to the guidelines of ASBMR [57].

Omd-deficient mice and wildtype controls of 6-week-old were injected with calcein 9 and 2 days before sacrifice. The transversal sections of femora were analyzed for dynamic histomorphometry with Osteomeasure software in a blinded fashion as well according to the ASBMR guidelines [57].

2.2.7 Cell culture

ST2 cells (obtained from Leibniz Institute DSMZ, Braunschweig, DE), calvarial osteoblasts and bone marrow-derived osteoblasts were utilized for *in vitro* analysis. All cells were cultured at 37°C in an atmosphere with 5% CO2 and a relative humidity of 95%. Osteogenic differentiation was started and maintained by supplementing 50µg/ml ascorbic acid and 10mM β-glycerophosphate (both from Sigma-Aldrich Corp., St. Louis, US) to the medium.

The details of isolation and culture of calvarial and bone marrow-derived osteoblasts are described in the individual sections below.

ST2 is a mesenchymal stem cell line derived from mouse bone marrow and can be induced to differentiate into osteoblasts. In this thesis, ST2 cells were used for transfection, stimulation of different reagents and gene knockdown by siRNA. ST2 cells were cultured in αMEM +/+ medium in cell culture flask and fresh medium was routinely changed on every Monday, Wednesday and Friday. The cells were passaged when they reached about 90% confluence by detaching with Trypsin/EDTA (0.25%, Fisher Scientific International, Inc. Pittsburgh, US). The details of culture and methods of the experiments are described in the individual sections below.

2.2.8 Isolation and culture of bone marrow-derived osteoblasts

Bone marrow-derived osteoblasts were isolated from *Omd*-deficient mice of both genders and wildtype male mice at the age of 7 weeks. After sacrifice, femora, tibiae and whole coxae were isolated and temporarily stored on ice. Afterwards, all the bone samples were transferred into the clean bench. A PCR tube with a small hole in the bottom was fixed into an Eppendorf tube to spin down the bone marrow. The femora were cut proximal to the distal growth plate while the tibiae were cut through the distal tibiofibular connection. The coxae were cut proximal to the acetabulum. All the bones were placed into the PCR tubes with the open side downwards. Bone marrow was collected into the Eppendorf tube by a transient centrifugation at 6,000rcf for 12s and then resuspended with 500µl prewarmed αMEM +/+ medium per tube. The mixture was filtered through a cell strainer (70µm, Greiner Bio-One GmbH, Kremsmünster, AT) and the strainer was flushed using additional 2ml of αMEM +/+ medium. A cell counting chamber (Thoma, LO - Laboroptik Ltd., Lancing, GB) was utilized for counting the cells according to the manufacturer’s guidelines. Then cells were seeded into 12-well cell culture plates (Greiner Bio-One GmbH, Kremsmünster, AT) at a concentration of 5 million cells/ml (1ml/well). The medium was changed for the first time 2 days after seeding the cells. When the cells reached 80~90% confluence, osteogenic differentiation was started. Medium change was done every two days during osteogenic differentiation until day 11 and 15 respectively. RNA isolation, subsequent qRT-PCR, alizarin red staining and corresponding quantification were performed afterwards to measure gene expression and mineralization capacity of the cells.

Femora that were left from the experiment were stored in liquid nitrogen immediately after removing soft tissues as much as possible and were used for further RNA isolation as indicated below.

2.2.9 Isolation and culture of calvarial osteoblasts

Calvarial osteoblasts were isolated from newborn mice at the age of 3 to 5 days. Following sacrifice by decapitation, the soft tissues were carefully removed from the calvaria in the clean bench. Then then calvariae were temporarily stored in sterile PBS. Digestion buffer was prepared and prewarmed to 37°C and then filtered through a filtration cup (0.22µm pore size) in the clean bench before use. The calvaria underwent initial incubation in 10 to 12ml digestion buffer (enough for 5 mice) at 37°C for 12 min with simultaneous shaking at 200rpm. Afterwards, the digestion buffer was discarded and replaced by fresh buffer, followed by a further digestion for 50min at 37°C with simultaneous shaking at 200rpm. After the digestion completed, the solution was filtered in the bench through a filter (70µm, Greiner Bio-One GmbH, Kremsmünster, AT) and the filter was flushed with extra 2ml of αMEM +/+ medium. After the filtered solution was centrifuged at 400rcf for 6 min, all the liquid was removed without disturbing the cell layer. The cells were resuspended with fresh and warm αMEM +/+ medium and cell counting was performed as demonstrated above. Cells were plated in 12-well cell culture plates (Greiner Bio-One GmbH, Kremsmünster, AT) with a concentration of 50,000 cells/ml (1ml/well) in αMEM +/+ medium.

Osteogenic differentiation was initiated when the cells reached 80~90% confluence. Calvarial osteoblasts underwent no osteogenic differentiation or differentiation for 4, 7,10 and 20 days respectively, during which the medium was changed every two days, followed by RNA isolation from each time point and subsequent qRT-PCR to measure gene expression.

2.2.10 Stimulation of ST2 cells

ST2 cells were utilized for the stimulation with the reagents listed below:

1. reWNT1/SFRP1 complex (recombinant mouse WNT1/SFRP1 complex, 9765-WN, R&D Systems, Minneapolis, US. Final concentration: 100ng/ml)
2. reSFRP1 (recombinant mouse SFRP1, 9019-SF, R&D Systems, Minneapolis, US. Final concentration: 50ng/ml, as equimolar control for reWNT1/SFRP1)
3. reWNT3a (recombinant murine WNT3a, 315-20, PeproTech, Cranbury, US. Final concentration: 100ng/ml)
4. reWNT5a (recombinant mouse WNT5a, 645-WN, R&D Systems, Minneapolis, US. Final concentration: 100ng/ml)

All the reagents were reconstituted as the manufacturer’s guideline instructed while PBS was used as control. ST2 cells were seeded into 24-well cell culture plate with the concentration of 100,000 cells/ml (0.5ml/well) in αMEM +/+

medium. After 2 days, when the cells proliferated to 80~90% confluence, cells were washed with PBS to remove the serum completely. Afterwards, the reagents were administrated to the cells in αMEM -/- medium with the concentrations indicated above. reWNT1/SFRP1 and reSFRP1 were administrated for the stimulation of 0.5, 2 or 6 hours while reWNT3a and reWNT5a were used only for 6 hours. RNA isolation was performed after the stimulation.

reWNT1/SFRP1 and reSFRP1 were also administrated to ST2 cells with PBS as control for 6 hours after *Fzd2* gene knock down as demonstrated below with the same final reagent concentrations. RNA was isolated subsequently.

2.2.11 Transfection

ST2 cells were transfected with the previously described pLNCX-based expression plasmids containing either the wildtype *Wnt1* open reading frame or an osteogenesis imperfecta-causing variant encoding the G177C mutation [25]. Lipofectamine™ 2000 Transfection Reagent (Thermo Fisher Scientific Inc., Waltham, US) was utilized to perform the transfection according to the manufacturer's instruction with further optimizations as described below in Table 9.

ST2 cells were seeded into 12-well plate in αMEM +/+ medium with the concentration of 100,000 cells/well (1ml/well). After 2 days, when the cell reached 80~90% confluence, the transfection was performed. The plasmid amount for each well was 1μg. The transfection lasted for 5 days in total, while the medium was changed once 2 days after transfection. RNA isolation and expression analysis were performed afterwards as indicated in the section below.

Table 9. Protocol for transfection

Steps	**Component**	**Volume per well (μl)**
Dilute Lipofectamine™ 2000 Reagent	Opti-MEM™ medium	50
	Lipofectamine™ 2000 Reagent	2μl
Dilute plasmid DNA	Opti-MEM™ medium	50
	Plasmid DNA	1μg
Prepare DNA-lipid complex	Add diluted DNA to diluted Lipofectamine™ 2000 Reagent: Transfer 50μl of diluted DNA to diluted Lipofectamine™ Reagent, then mix gently	
Incubation	Incubate for 5min at room temperature	
Add DNA-lipid complex to cells	Add 100μl of DNA-lipid complex directly to cells	

2.2.12 Gene knockdown by siRNA

A Fzd2 endoribonuclease-prepared siRNA (esiRNA, EMU073051, Sigma-Aldrich Corp., St. Louis, US) was utilized to perform gene knock down in ST2 cells. Specifically, Fzd2 esiRNA was reconstituted in TE buffer and aliquoted according to the manufacturer’s guidelines. Actual concentration of Fzd2 esiRNA stock was 12.25μM as measured by spectrophotometer. Silencer™ Select Negative Control No.1 siRNA (Stock=10μM, 4390843, Thermo Fisher Scientific Inc., Waltham, US) was used as negative control.

Lipofectamine™ RNAiMAX Transfection Reagent (13778075, Thermo Fisher Scientific Inc., Waltham, US) was used for the transfection based on the manufacturer’s instructions with my optimizations. To be specific, Opti-MEM™ medium (31985062, Thermo Fisher Scientific Inc., Waltham, US) was used for dilution of RNAiMAX Reagent and siRNA as indicated below in Table 10. The siRNA-lipid complex was prepared by adding diluted siRNA into diluted RNAiMAX Reagent. The complex solution was incubated at room temperature and then loaded into 24-well plates (50μl/well).

Reverse transfection was performed in 24-well plates by seeding the resuspended cells into the plate with siRNA-lipid complex already inside with a cell density of 30,000/ml in αMEM +/+ medium (0.5ml/well). The final concentration of both Fzd2 esiRNA and control siRNA was 10nM. After 3 days, when the cells reached 80~90% confluence, PBS or reWNT1/SFRP1 or reSFRP1 was administrated for 6h to stimulate the cells as demonstrated above. Afterwards RNA isolation and qRT-PCR were performed to measure gene expression.

Table 10. Protocol for *Fzd2* gene knockdown

Steps	Component	Volume (µl)	
1. Dilute RNAiMAX Reagent for Ctrl siRNA	Opti-MEM™ medium	25	× number of wells for corresponding group (Ctrl / Fzd2)
	RNAiMAX Reagent	1.5	
2. Dilute RNAiMAX Reagent for Fzd2 esiRNA	Opti-MEM™ medium	25	
	RNAiMAX Reagent	1.5	
3. Dilute Ctrl siRNA	Opti-MEM™ medium	25	
	Ctrl siRNA (Stock=10µM)	0.5	
4. Dilute Fzd2 esiRNA	Opti-MEM™ medium	25	
	Fzd2 esiRNA (Stock=12.25µM)	0.41	
5. Prepare siRNA-lipid complex	Add diluted siRNA into corresponding diluted RNAiMAX Reagent: Transfer 400µl mixture from Step 3 (or 4) to the mixture from Step 1 (or 2), then mix gently		
6. Incubation	Incubate for 5min at room temperature		
7. Load siRNA-lipid complex into plate	Load 50µl siRNA-lipid complex per well (24-well plate) for corresponding group (Ctrl / Fzd2)		
8. Seed the cells to perform reverse transfection	Seed ST2 cells into the 24-well plate (30,000 cells/ml, 0.5ml/well) in αMEM +/+ medium		
Final volume or amount per well	siRNA-lipid complex	50µl	
	siRNA	5pmol	
	RNAiMAX Reagent	1.5µl	

2.2.13 RNA isolation and cDNA synthesis

RNA of cultured cells and multiple mouse tissues was isolated by using the Macherey-Nagel NucleoSpin RNA/Protein Kit (Macherey-Nagel, GmbH & Co. KG, Düren, DE) according to the manufacturer's guidelines.

RNA from the femoral cortex of 7-week-old *Omd*-deficient mice and wildtype controls was isolated by using peqGOLD TriFast Kit (PEQLAB Biotechnologies GmbH, Erlangen, DE) according to the manufacturer's guidelines. More specifically, femoral cortexes were obtained from the femora which were used for isolation of bone marrow-derived osteoblasts mentioned above. Samples were ground into a fine powder in liquid nitrogen, then transferred into 1ml TriFast reagent and vortexed for 15s. After incubation at room temperature for 5min, 200µl of phenol/chloroform was added into the solution. Following another incubation at room temperature for 10min, the samples were centrifuged at 12,000rcf for 15min at 4°C. The aqueous phase (about 450µl) was collected without disturbing other phases. Then 450µl isopropanol was added to the aqueous phase and vortexed for 15s, followed by a centrifugation at 12,000rcf for 10min at 4°C to precipitate RNA. The liquid was removed by pipetting as much as possible without disturbing the RNA pellet. Then 500µl 70% ethanol in DEPC-H_2O was added to wash the RNA pellet, followed by a centrifugation at 12,000rcf for 7min at 4°C. The liquid was removed by pipetting as much as possible without touching the RNA pellet. The RNA pallet was air-dried for 5min, then 20µl of RNAse-free H_2O was added directly to dissolve RNA. The concentration and purity of RNA were measured by a spectrophotometer.

The Verso cDNA Synthesis Kit (Thermo Fisher Scientific Inc., Waltham, US) was utilized to synthesize cDNA according to manufacturer's instructions. The reaction protocol is listed in Table 11**.**

Table 11. Protocol for cDNA synthesis

Components	Volume (µl) 1×
5× cDNA Synthesis Buffer	2
dNTP Mix (5 mM)	1
Anchored Oligo dT (500 ng/µL)	0.5
Verso Enzyme Mix	0.5
RT Enhancer	0.5
H_2O	1.5*
RNA	4*
Total	10
42°C 30min → 95°C 2min → Dilute with H_2O according to cDNA concentration (3 to 4 times)	
* Can be adjusted according to RNA concentration. Maximum RNA amount is 500ng.	

2.2.14 Expression analysis

qRT-PCR was utilized to measure the expression analysis in numerous experiments using the StepOnePlus Real-Time PCR System (Applied Biosystems Inc., Waltham, US) with predesigned TaqMan gene expression assays as listed above in the section TaqMan probes. Gene expression was presented relative to *Gapdh* or as fold change values compared to corresponding control group based on the $\Delta\Delta C_T$ method as indicated in the figures. The reaction protocol for qRT-PCR is demonstrated in Table 12 below.

Table 12. Reaction components for qRT-PCR

Components	Volume (µl) per well
TaqMan™ Gene Expression Master Mix	10
TaqMan™ Primer	1
cDNA	2*
H_2O	7*
Total	20
* Can be adjusted according to RNA and cDNA concentration. Routine amount of cDNA is 200ng.	

Microarray-based whole transcriptome analysis was performed utilizing Clariom™ D Assay (mouse, Thermo Fisher Scientific Inc., Waltham, US) according to the manufacturer's GeneChip™ WT PLUS Reagent Kit user guide (Document 703174, revision A.0) after the measurement of RNA concentration and quality using the Agilent 2200 TapeStation System (Agilent Technologies, Inc., Santa Clara, US). In brief, 100ng of total RNA per sample pooled from three independent experiments per condition was used for the synthesis of 2nd-cycle ss-cDNA. Gene chip hybridization was performed with 5µg per sample of fragmented and labeled cDNA. After washing and staining with Affymetrix GeneChip Fluidics Station 450 (Affymetrix, Santa Clara, US), microarrays were scanned with the Affymetrix GeneChip Scanner 3000 7G (Affymetrix, Santa Clara, US). Data were analyzed with Transcriptome Analysis Console software (TAC 4.0, Thermo Fisher Scientific Inc., Waltham, US) using the default analyzing settings (v2) and Gene + Exon - SST-RMA as summarization. Full datasets have been uploaded to the GEO repository (GSE249300) [58].

2.2.15 Mineralization analysis

Alizarin red staining and corresponding quantification were performed to assess the mineralization of bone marrow-derived osteoblasts from 7-week-old *Omd*-deficient and wildtype mice after osteogenic differentiation for 11 or 15 days. First, the cells were washed with 1ml/well PBS. Then they were fixed with 1ml/well of 90% cold ethanol for 15min. After fixation, ethanol was removed and all the wells were washed twice with 1ml/well of water. Then cells were stained with 1ml/well of the staining solution (40mM Alizarin red S in H_2O, pH=4.1~4.2) for 10min. Afterwards, the staining solution was removed and all the wells were washed with 1ml/well of water for 3 to 5 times depending on the staining intensity. Pictures of all wells were taken after removing the liquid.

For quantification, 800µl/well of 10% acetic acid in H_2O was added and incubated for 30min at room temperature. Cell layers were completely lifted using cell scrapers and then transferred into new microreaction tubes together with the liquid. Then the samples were incubated at 85°C for 10min, followed by centrifugation for 10min at 21,000rcf. Then 400µl of supernatant was transferred into new microreaction tubes with 150µl of 10% ammonium hydroxide inside. After mixing, if the solution was deep red with flaky color particles inside, more acetic acid would be added until the solution turned yellow. The same amount of acetic acid should be added into all the samples which would be compared with. At last, 150µl liquid was transferred into a microtiter plate (Sarstedt AG & Co. KG, Nürmbrecht, DE) and the absorption was measured at 405nm with a Microtiter plate reader (Molecular Devices, San Jose, US). Equivalent volumes of 10% acetic acid in H_2O and 10% ammonium hydroxide were used as blank control.

2.2.16 Protein isolation

Proteins were isolated from bone marrow-derived osteoblasts from *Omd*-deficient and wildtype mice after osteogenic differentiation for 15 days. First, the medium was removed and the wells were washed with PBS once. After removing PBS, 150µl of RIPA buffer (supplemented with 1× protease inhibitor cocktail and phosphatase Inhibitor cocktail, both from Roche AG, Basel, CH) was added into each well. The cell layers were completely lifted with cell scrapers, then the mixture was transferred into new microreactoion tubes. The samples were mixed by vortex for 15s, followed by an incubation at 4°C for 15min. Afterwards, the samples were centrifuged at 21,000rcf for 10min at 4°C. The supernatant was collected without disturbing the residues.

Bradford assay was utilized to measure the concentration of the protein samples with Bradford reagent (Bio-Rad Protein Assay Dye Reagent Concentrate). Pierce™ Bovine Serum Albumin Standard (2mg/ml) was diluted with H_2O to a concentration of 0.2mg/ml to make standard reference as demonstrated below in Table 13.

Table 13. Components for Bradford assay standard reference

Contains BSA (µg)	Diluted BSA solution (µl, 0.2mg/ml)	H_2O (µl)	Bradford reagent (µl)
0	0	800	200
5	25	775	200
10	50	750	200
15	75	725	200
20	100	700	200

After adding 200µl of Bradford reagent, the solution was thoroughly mixed by vortex for 10s. For sample measurement, 10µl of the protein sample was mixed with 790µl of H_2O and 200µl of Bradford reagent, followed by vortex for 10s. Then 100µl of the mixed solution was transferred into a 96-well microtiter plate

(Sarstedt AG & Co. KG, Nürmbrecht, DE) and the absorption was measured at 595nm with a Microtiter plate reader. The actual concentration of protein samples was calculated based on the standard reference.

2.2.17 Western Blotting

NuPAGE™ LDS Sample Buffer (4×, Life Technologies, Carlsbad, US) was used for sample preparation prior to Western Blotting as indicates below in Table 14.

Table 14. Sample preparation for Western Blotting

Components	Volume (µl) per well
Protein sample	x (contains 20µg protein)
NuPAGE™ LDS Sample Buffer (4×)	7.5
Reducing agent	3
H_2O	$19.5 - x$
Total volume	30

Bolt™ 4~12% Bis-Tris, 1.0 mm×10 well pre-made gels (Invitrogen Corp., Waltham, US) were used with 20µg protein sample for each well. Bolt™ MES SDS Running Buffer (Life Technologies, Carlsbad, US) and Mini Gel Tank system (Thermo Fisher Scientific Inc., Waltham, US) were used for electrophoresis according to the manufacturer's guidelines. Specifically, the electrophoresis was performed at 90V for 75min. Then the Mini Gel Tank system was utilized with Mini Blot Module (Thermo Fisher Scientific Inc., Waltham, US) and Nitrocellulose membrane (0.45µm pore size, Schleicher & Schuell Inc., Keene, US) for protein transfer according to the manufacturer's guidelines. The diluted Bolt™ Transfer Buffer (Life Technologies, Carlsbad, US) was always supplemented with 10% methanol. The membrane was immersed into transfer buffer for at least 10min before use. The transfer was performed at a constant voltage of 10V for 60min.

After protein transfer, the membrane was washed 3 times with TBST for 5min. Then Ponceau S staining was performed on the membrane by incubating in Ponceau S solution for 1min with gentle shaking to verify transfer efficiency, followed by washing with H_2O for 5min for 1 to 3 times until the bands became separate and clear. After taking pictures, the membrane was washed with H_2O for 5min for 6 to 8 times until the red staining was completely removed.

Blocking was performed with 5% BSA (Sigma-Aldrich Corp., St. Louis, US) in TBST for 1h at room temperature. Then the membrane was incubated overnight with gentle shaking at 4°C in OMD primary antibody. On the second day, the membrane was washed 3 times with TBST for 5min, and the incubation of secondary antibody (Polyclonal Rabbit Anti-Goat Immunoglobulins/HRP) was performed for 1h at room temperature with gentle shaking. The details of the antibodies and the dilution ratios are listed in the Table “Primary and secondary antibodies for Western Blotting” in Materials section.

After incubation, the membrane was washed 3 times with TBST for 5min. Subsequently detection was performed with Pierce™ ECL Plus Western Blotting Substrate (40:1 ratio, Thermo Fisher Scientific Inc., Waltham, US) according to the manufacturer’s instruction. The Molecular Imager ChemiDoc™ XRS System (Bio-Rad Laboratories, Inc., Hercules, US) and the Quantity One program (Bio-Rad Laboratories, Inc., Hercules, US) were used to record images of the Western Blotting with an exposure time of 30min.

After the detection for OMD, the membrane was washed twice with TBST for 5min, and then stripped by Re-Blot Plus Strong Antibody Stripping Solution (Merck Millipore, Burlington, US) for 15min at room temperature and used for detecting β-actin. The membrane was washed 3 times with TBST for 5min, followed by re-blocking in 5% BSA in TBST for 45min at room temperature. The incubation with β-actin primary antibody and secondary antibody (Goat Anti-Rabbit Immunoglobulins/HRP) and the washing steps were performed in the same way as OMD detection. Imaging was performed as described above with 40 min exposure time Pierce™ ECL Western Blotting Substrate (1:1 ratio, Thermo Fisher Scientific Inc., Waltham, US).

2.2.18 Three-point-bending test

Three-point-bending test was performed to measure the biomechanical property of femora after µCT analysis. Before testing, any soft tissues on the femoral diaphysis were removed. The test was performed with a universal testing machine (Z2.5/TN1S, ZwickRoell GmbH & Co. KG, Ulm, DE). The femora were horizontally placed with the posterior surface facing downward at a support distance of 7mm. The femoral midshaft was positioned at the mid-point of the support distance, while the femoral axis located centrally in the support area. A constant displacement rate of 0.05mm/s was applied. Load-displacement data were recorded until failure. The results such as elastic modulus, maximum load and load until fracture were determined by the testXpert III software (ZwickRoell GmbH & Co. KG, Ulm, DE). The structural data of cortical compartment derived from µCT analysis, including inner and outer diameter, were used to calculate the mechanical parameters such as second moment of area, section modulus, and subsequent flexural strength. All the calculations were performed on the assumption that the femur shaft can be approximated as a hollow cylinder. The detailed calculation and equations are listed as below.

Elastic modulus, which represents the material stiffness, was defined as the ratio of the stress applied to the bone and the resulting strain within the linear elastic region, which was automatically determined by the software.

The calculation is: $E = Stress/Strain$

Second moment of area (I) was calculated as: $I = \frac{\pi\left(D^4 - d^4\right)}{64}$

Section modulus (W) was calculated as: $W = \frac{\pi\left(D^4 - d^4\right)}{32D}$

D is the outer diameter of cortical ring while d is the inner diameter in both equations.

Flexural stiffness $= EI$

i.e. the product of elastic modulus and second moment of inertia.

Flexural strength (σ) was calculated for the point when the maximum load was applied. $\sigma = \frac{My}{I}$

M is the bending moment. y is the maximum distance from the neutral axis to the outermost surface on the bending plane, i.e. $D/2$ here. I is the second moment of area.

Then the equation is equal to: $\sigma = \frac{\left(\frac{F}{2}\right)\left(\frac{L}{2}\right)\left(\frac{D}{2}\right)}{\frac{\pi\left(D^4 - d^4\right)}{64}}$

F is the maximum load. L is the support distance, i.e. 7mm here.

2.2.19 Nanoindentation

My colleagues Prof. Dr. Björn Busse and Dr. Praveer Sihota kindly performed the nanoindentations using the tibiae of 12 weeks old female *Omd*-deficient mice and wildtype littermate controls. Before testing, all embedded samples were ground to a co-planar finish and surface-polished. The measurement was performed utilizing the iMicro Nanoindenter (KLA Corporation, Milpitas, US) equipped with a Berkovich diamond tip. The cortical bone of each sample was tested with 10~20 indentations at a distance of at least 20μm between each indent. The integrated microscope was used to validate the indents regarding correct position and appearance. Indentations were performed in depth-sensing continuous stiffness mode with a target depth of 3000nm and a target indentation strain rate of 0.05/s. Calibration was done on fused silica before and after each measurement. The hardness and elastic modulus were evaluated applying a Poisson's ratio of 0.3 based on a previously described method using the software provided by the manufacturer [59].

2.2.20 Circular polarized light microscopy

Circular polarized light imaging was performed on 4µm undecalcified tibia sections with Toluidine blue staining by utilizing an Olympus BX53 microscope with polarization filters (Olympus Corp., Tokyo, JP). Controlled by Olympus cellSense Dimension software (v4.1, Olympus Corp., Tokyo, JP), two adjacent regions of interest for each medial and lateral cortical bone were imaged beginning 0.7 mm distal of the proximal growth plate (Fig. 14A). Images were analyzed by ImageJ (v1.54f, National Institutes of Health, Bethesda, US) by first converting the images into grey scale and then using the plugin "OrientationJ" (v2.0.5) to measure the coherency of collagen fibers [60,61]. While selecting the region of cortex for analysis, any bone marrow region was excluded.

2.2.21 Quantitative backscattered electron imaging (qBEI)

My colleague Dr. Simon von Kroge kindly carried out the qBEI measurements utilizing the tibiae from 12-week-old female *Omd*-deficient and wildtype control mice. The bone mineral density distribution of cortical bone was determined as described previously [62]. Methylmetacrylate-embedded tibiae were imaged using a backscattered electron detector (Type 202, K.E. Developments Ltd., Cambridge, UK) attached to a scanning electron microscope (LEO 435, LEO Microscopy Ltd., Cambridge, UK). Analysis was performed for the regions of interest located 1~2mm distal of proximal growth plate on both medial and lateral side. Gray-value based mages were acquired to evaluate the local calcium content by a custom-made MATLAB script (The MathWorks, Inc., Natick, US) to derive characteristic determinants of the bone mineral density distribution and osteocyte lacunae.

2.2.22 Atomic force microscopy (AFM)

Prof. Dr. Dr. Petar Milovanovic and Dr. Dr. Jelena Jadzic from the Center of Bone Biology at the University of Belgrade kindly performed the atomic force microscopy and evaluation by using the femora from 12-week-old female *Omd*-deficient mice and the wildtype controls. The mice were sacrificed and the femora were isolated and stored as described above in the section Mouse organs and skeleton preparation in Materials and Methods part.

The cortex from mid-diaphysis of undecalcified femora was fixed onto a sample disk and imaged by a Level atomic force microscopy system (Anfatec Instruments AG, Oelsnitz, DE) under ambient conditions. The images were obtained in high-resolution dynamic (non-contact) scanning mode using an atomic force microscopy probe (MikroMasch, Sofia, BG) with the following circumstances: AFM cantilever length was 125μm; force constant was 40N/m; resonant frequency was around 275kHz; AFM tip radius less than 10nm. The samples were scanned with the field of view of 2μm×2μm, image resolution of 256×256 pixels and scanning speed of 2 lines per second. For each bone sample, at least 10 different sites of images were evaluated to measure the heterogeneity of bone nanostructure. Topography, amplitude, and phase images were obtained simultaneously, enabling more comprehensive evaluation of the observed nanostructural features.

Semiquantitative analysis of observed nanostructural features or patterns was performed in a blinded procedure by two investigators to determine the relative frequency of images containing a particular feature or pattern per mouse. Each image was classified into one of the available categories regarding one parameter (i.e. surface homogeneity, density of packing and parallelism). More specifically, the categories including heterogenous, intermediate and homogenous were determined for the parameter surface homogeneity. Loose, intermediate and dense were determined for the parameter density of packing (of collagen fibrils). Disorganized, intermediate and unidirectional were determined for the parameter parallelism (of collagen fibrils). The percentage of images assigned to each category for the respective parameter was calculated per animal.

2.2.23 Statistical analysis

All data in the manuscript are presented as individual values as well as means ± standard deviations. Statistical analysis for the comparison of two groups was performed by initial testing for equal variance by F-test and subsequent unpaired two-tailed Student's t-test if there was no difference in variance or Welch's t-test if the variance was significantly different. For the comparison of multiple groups, one-way or two-way ANOVA with Tukey's multiple comparison test was used. Chi-squared test was utilized to compare observed vs. expected results. All statistical analyses were performed using GraphPad Prism (GraphPad Software Inc. San Diego, US). P-values below 0.05 were considered statistically significant. Sample size and power of analysis for animal experiments were determined by apriori t-test with G*Power for a significance level α of 0.05 and power of 0.8 based on an estimated effect size [63].

3. Results

3.1 *Omd* is a WNT1-induced gene

Based on previous studies of our group and other researchers, the function of WNT1 in skeletal integrity and bone anabolism has been extensively verified [23-25]. However, the detailed mechanism of WNT1 in these processes is still unclear. As a continuation of my medical doctorate dissertation, the first aim of my study was to explore the potential downstream targets of WNT1 during bone formation.

To achieve this goal, ST2 cells were transfected with either a *Wnt1* expression plasmid or an empty pLNCX vector. Whole transcriptome expression analysis was performed by microarray 5 days after transfection to compare the gene expression after transfection of *Wnt1* expression plasmid or the empty pLNCX vector. *Postn*, *Aspn* and *Omd* were the three most strongly induced genes when *Wnt1* was overexpressed (Fig.1A). Subsequently, qRT-PCR was performed to confirm the expression of these genes. In contrast, transfection with the plasmid carrying the *Wnt1-G177C* variant which causes osteogenesis imperfecta could not induce any of these genes (Fig.1B).

I previously found that *Omd* and *Postn* were significantly induced by a recombinant WNT1/SFRP1 complex in ST2 cells [25]. Therefore, I performed more extensive experiments to investigate if these genes are direct downstream targets of WNT1. ST2 cells were stimulated with recombinant WNT1/SFRP1 or SFRP1 for 0.5, 2 or 6 hours with PBS-treatment as negative control. Subsequent qRT-PCR indicated a significant induction of *Omd* in response to stimulation with reWNT1/SFRP1 after 2h and even more strongly after 6h similar to a canonical WNT-signaling target gene *Apcdd1* [64,65]. *Postn* was only significantly induced after 6h (Fig.1C). In contrast, *Aspn* was not induced. In order to verify if the induction is caused by the activation of canonical WNT-signaling, the established canonical WNT ligand reWNT3a [12,66] and the non-canonical WNT ligand reWNT5a [67] were administered to ST2 cells for 6h. qRT-PCR showed significant induction of *Apcdd1*, *Omd* and *Postn* by reWNT3a compared to PBS, which is similar to reWNT1/SFRP1, while reWNT5a only significantly induced *Aspn* (Fig.1C). Collectively, these data indicate that *Omd* and *Postn* are induced upon canonical WNT-signaling activation.

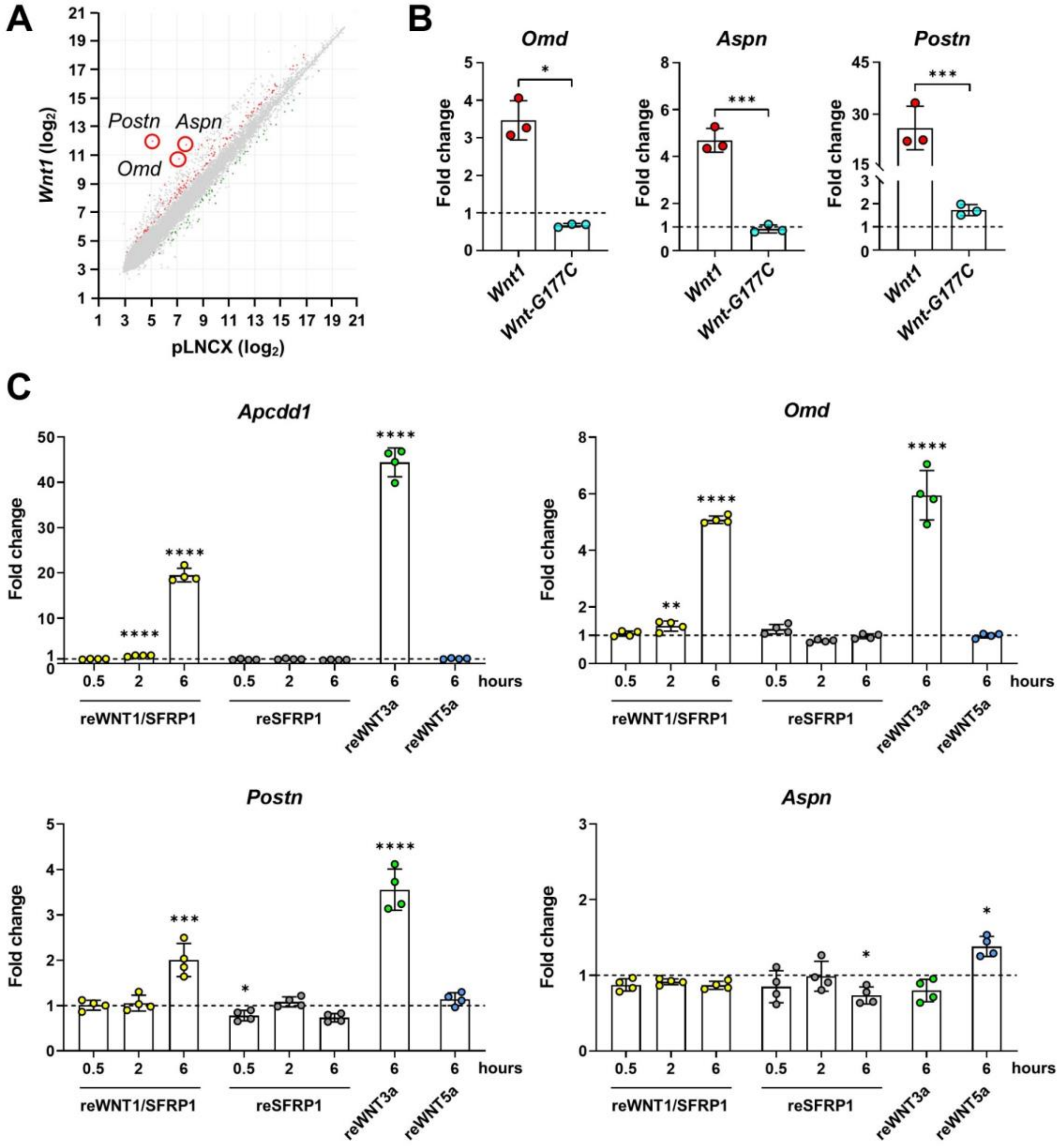

Figure 1. *Omd* is a WNT1-induced gene. (A) Scatter plot of microarray expression analysis, which shows average signal intensities of transcripts in ST2 cells five days after transfection with a wildtype *Wnt1* expression plasmid or an empty pLNCX vector. The three most induced genes (i.e. *Omd*, *Aspn*, *Postn*) are marked by red circles. (B) Confirmation of microarray results by qRT-PCR. Expression of *Omd*, *Aspn* and *Postn* in ST2 cells five days after transfection with a *Wnt1* expression plasmid or a plasmid encoding the osteogenesis imperfecta-causing G177C variant of *Wnt1*. Data show expression relative to ST2 cells transfected with the empty pLNCX vector (dashed line). (C) Expression of *Apcdd1, Omd*, *Aspn* and *Postn* in ST2 cells stimulated for the indicated duration with either recombinant WNT1/SFRP1, SFRP1, WNT3a or WNT5a compared to corresponding controls treated with PBS (dashed line). Data were analyzed by Student's t-test (B, n=3) or one-way ANOVA with Tukey's multiple comparison test (C, n=4). * $p < 0.05$, ** $p < 0.01$, *** $p < 0.001$, **** $p < 0.0001$.

3.2 *In silico* analysis of *Omd* promoter sequence for the potential binding sites of the transcription factors TCF/LEF

An *in silico* analysis using ConTra v3 system [68] was performed for 1kb region upstream of the *Omd* transcription start site (TSS). There were five potential binding sites of the transcription factors TCF/LEF of canonical WNT-signaling (Fig.2), which further supports that *Omd* is a direct downstrem target of WNT1.

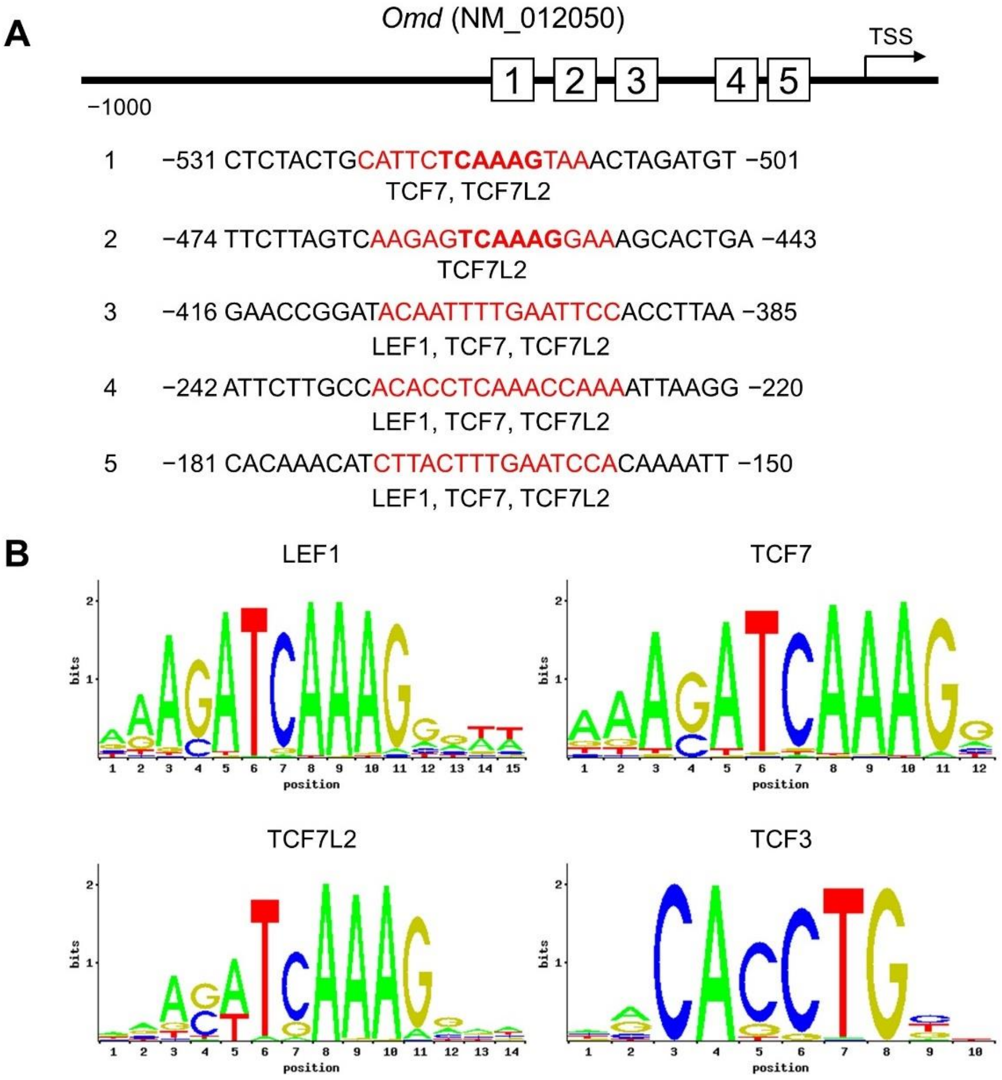

Figure 2. Potential TCF/LEF binding sites in the promoter region of the murine *Omd* gene. (A) Schematic presentation of the 1kb region upstream of *Omd* transcriptional start site (TSS) that was analyzed using ConTra v3 system. Identified TCF/LEF binding sites are indicated in the 5 sequence blocks shown below by red letters. Bold letters indicate the consensus binding motif. (B) Sequence logos representing the position weight matrices used for the identification of binding sites of indicated TCF/LEF family members.

3.3 *Omd* expression has a high tissue specificity

Given that gene expression levels and tissue specificity can provide information about the potential relevance of a given gene in specific organs, multiple tissues were obtained from C57Bl/6J wildtype female mice and qRT-PCR was performed to measure the expression of *Omd*, *Aspn* and *Postn* in these tissues. Compared to *Aspn* and *Postn*, *Omd* had a high and more specific expression in bone tissues (i.e. verterbral body and femur), which further indicates a potential role of OMD in the skeleton on the basis of the previous investigation on ST2 cells. Therefore, I selected OMD as the main research target of my study.

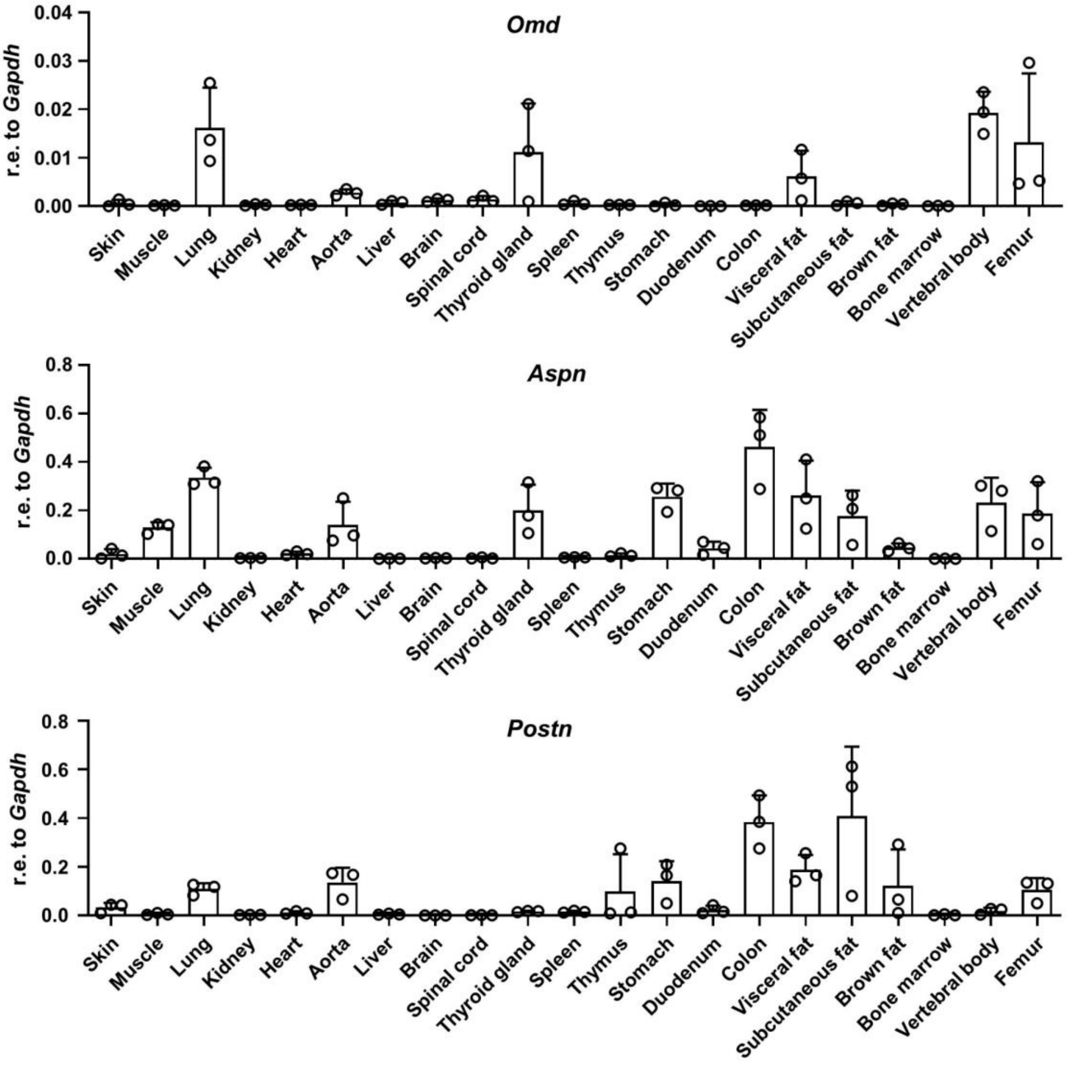

Figure 3. *Omd* expression has a high tissue specificity. Expression of *Omd*, *Aspn* and *Postn* in the indicated tissues as measured by qRT-PCR. Multiple tissues from 8-week-old female C57Bl/6J wildtype mice were obtained and subsequent qRT-PCR was performed to measure gene expression relative to *Gapdh*. n=3 for each tissue.

3.4 Generation of an *Omd*-deficient mouse line

Expression of *Omd* was determined by qRT-PCR in calvarial osteoblasts isolated from wildtype new born mice at different time points during the osteogenic differentiation process (Fig.4A). The expression of *Omd* increased along with progressing osteogenic differentiation, which indicates that OMD might play an important role for osteoblastic differentiation. Moreover, since the *in vivo* function of OMD was still not completely elucidated, I took advantage of *Omd*-deficient mice for this study. Thus, the *Omd*-deficient (*Omd* $^{-/-}$) mouse line was established at the animal facility after obtaining frozen sperms from the MMRRC repository. Genotypes of the newborn mice were determined by PCR amplifying the wildtype or mutant allele (Fig.4B). qRT-PCR confirmed the absence of *Omd* expression in *Omd*-deficient mice by measuring the gene expression in the femoral cortex at 7 weeks of age (Fig.4C). Allele frequency was calculated using all the offsprings from the heterozygous matings. Although there were less *Omd*-deficient mice, there was no significant difference regarding frequency when compared with the expected Mendelian ratio (Fig.4D). Moreover, no significant differences were observed regarding body mass and body length in 12- and 24-week-old female and 12-week-old male *Omd*-deficient mice compared with the corresponding wildtype controls (*Omd* $^{+/+}$) (Fig.4E).

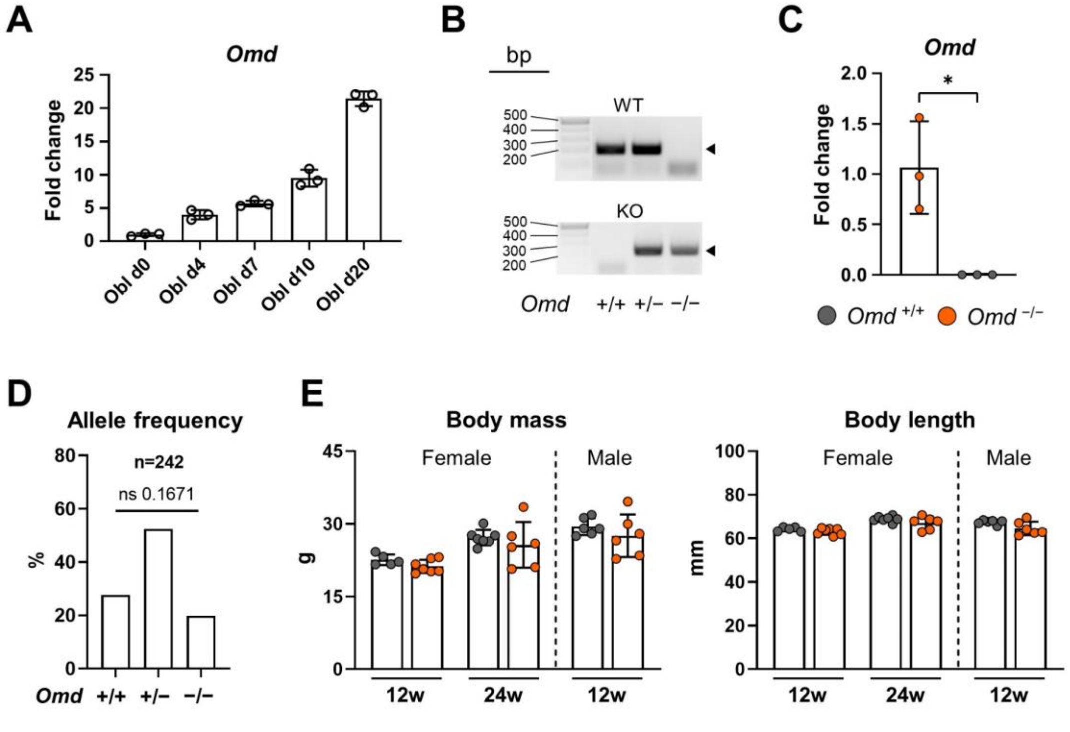

Figure 4. Generation of the *Omd*-deficient mouse line. (A) Expression of *Omd* as measured by qRT-PCR in calvarial osteoblasts at the indicated time points during osteogenic differentiation. Expression level is normalized to Obl d0. n=3 for each group. (B) Representative images of the genotyping PCR products (agarose gel

electrophoresis, EtBr stain) to determine the genotypes of newborn mice. The black triangles indicate the expected bands of wildtype and *Omd*-deficiency PCR products. (C) *Omd* expression in the femoral cortex of 7-week-old *Omd*-deficient mice and wildtype littermates as measured by qRT-PCR. Data were analyzed by Student's t-test (n=3). * $p < 0.05$. (D) Allele frequency calculated with all the offsprings (n=242) from matings of heterozygous mice. The observed frequency was compared with the expected Mendelian ratio by Chi-squared test. ns $p > 0.05$. (E) Body mass and body length were measured for female *Omd*-deficient and wildtype mice at the age of 12 and 24 weeks, and male mice at the age of 12 weeks. Data were analyzed by Student's t-test. n=5~7 as represented by individual data points.

3.5 Histomorphometric phenotyping of *Omd*-deficient mice in the trabecular bone of vertebral bodies

Structural histomorphometric analysis was performed on undecalcified spine sections with von Kossa/van Gieson staining from 12- and 24-week-old female and 12-week-old male *Omd* $^{-/-}$ mice compared to their respective wildtype controls. The trabecular compartment of vertebral bodies L3 and L4 was analyzed and the following parameters were determined: Bone volume per tissue volume (BV/TV), trabecular number (Tb.N) and trabecular thickness (Tb.Th). *Omd* deficiency did not change any of these parameters significantly in any analyzed group (Fig.5A, B).

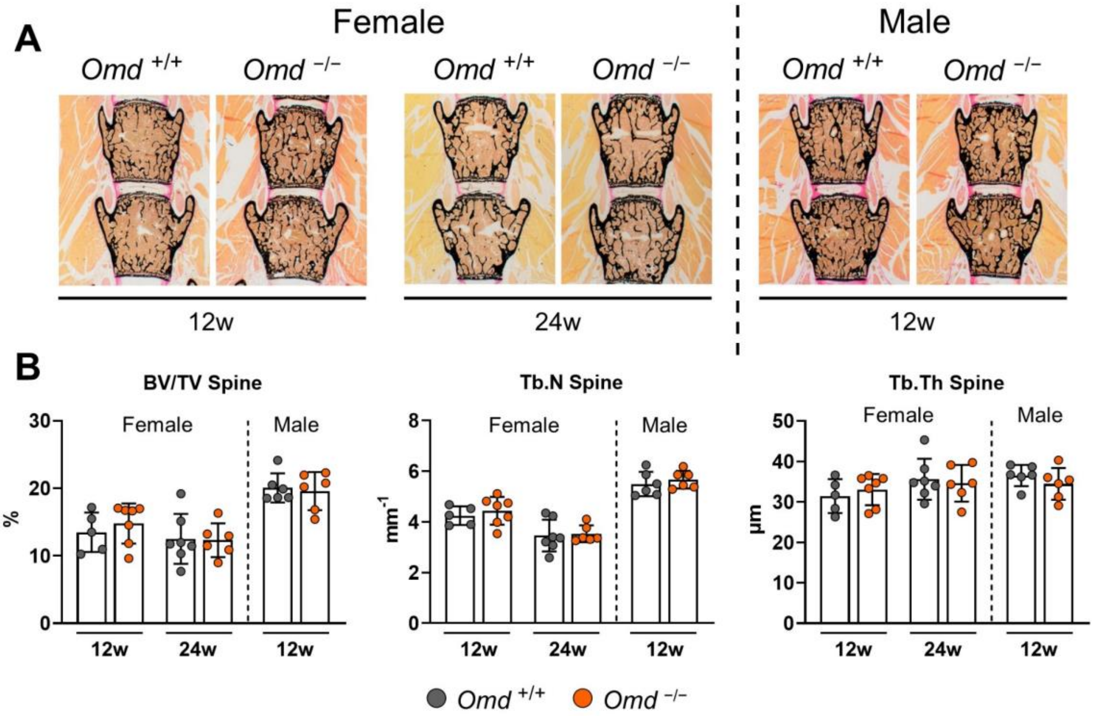

Figure 5. Histomorphometric phenotyping of *Omd*-deficient mice in the trabecular bone of vertebral bodies. (A) Representative images of undecalcified sections of vertebral bodies L3 and L4 with von Kossa/van Gieson staining from mice with the indicated gender, age and phenotype. (B) Results of histomorphometric analysis performed for the trabecular compartment of L3 and L4, including bone volume per tissue volume (BV/TV), trabecular number (Tb.N) and trabecular thickness (Tb.Th). Data were analyzed by Student's t-test. n=5~7 as represented by individual data points.

3.6 Histomorphometric phenotyping of *Omd*-deficient mice in the trabecular compartment of tibiae

As part of the appendicular skeleton, regulation of bone turnover in the tibia may differ from the spine. Therefore, histomorphometric analysis was also performed on undecalcified section of right tibiae with von Kossa/van Gieson staining for the same groups as described above. The trabecular compartment in the proximal metaphysis was analyzed. As observed in the spine, *Omd* deficiency did not cause any significant change in the structural parameters of the tibiae (Fig.6A, B).

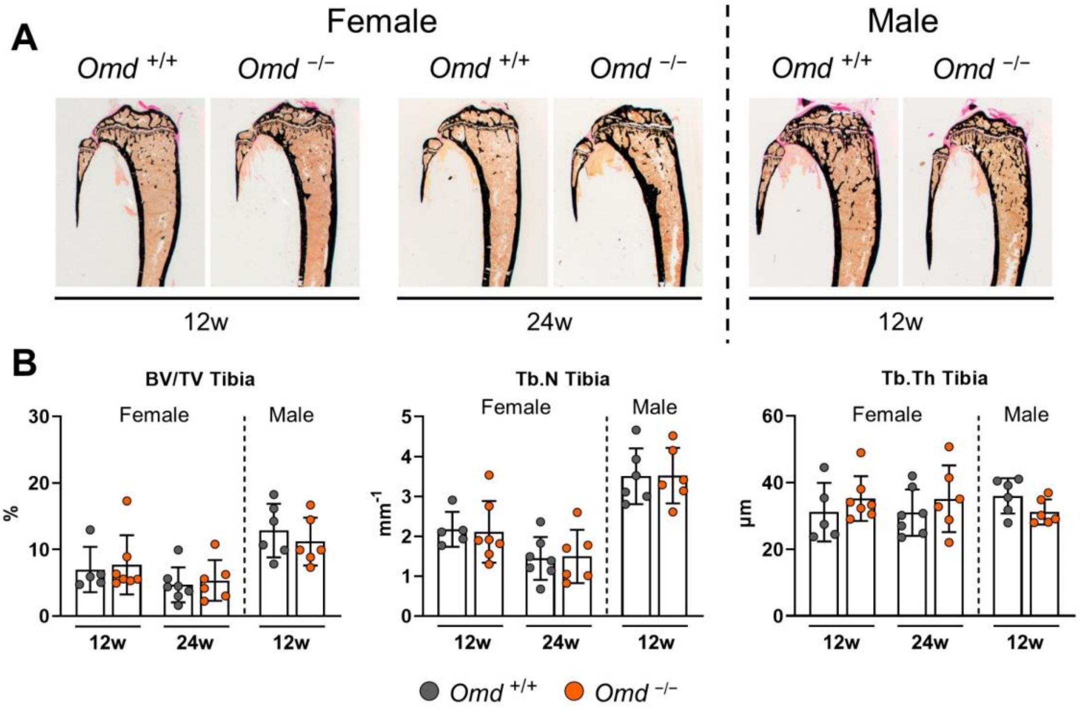

Figure 6. Histomorphometric phenotyping of *Omd*-deficient mice in the trabecular compartment of tibiae. (A) Representative images of undecalcified sections of right tibiae with von Kossa/van Gieson staining from mice with the indicated gender, age and phenotype. (B) Results of the structural histomorphometric analysis performed in the proximal metaphysis, including bone volume per tissue volume (BV/TV), trabecular number (Tb.N) and trabecular thickness (Tb.Th). Data were analyzed by Student's t-test. n=5~7 as represented by individual data points.

3.7 Influence of *Omd* deficiency on growth plate morphology

Meanwhile, the morphology of tibial growth plate was analyzed. In line with the lack of influence of *Omd* deficiency on longitudinal bone growth, the total thickness of the proximal tibial growth plate was not significantly different between female *Omd*-deficient and wildtype mice at the age of 12 weeks (Fig.7A, B).

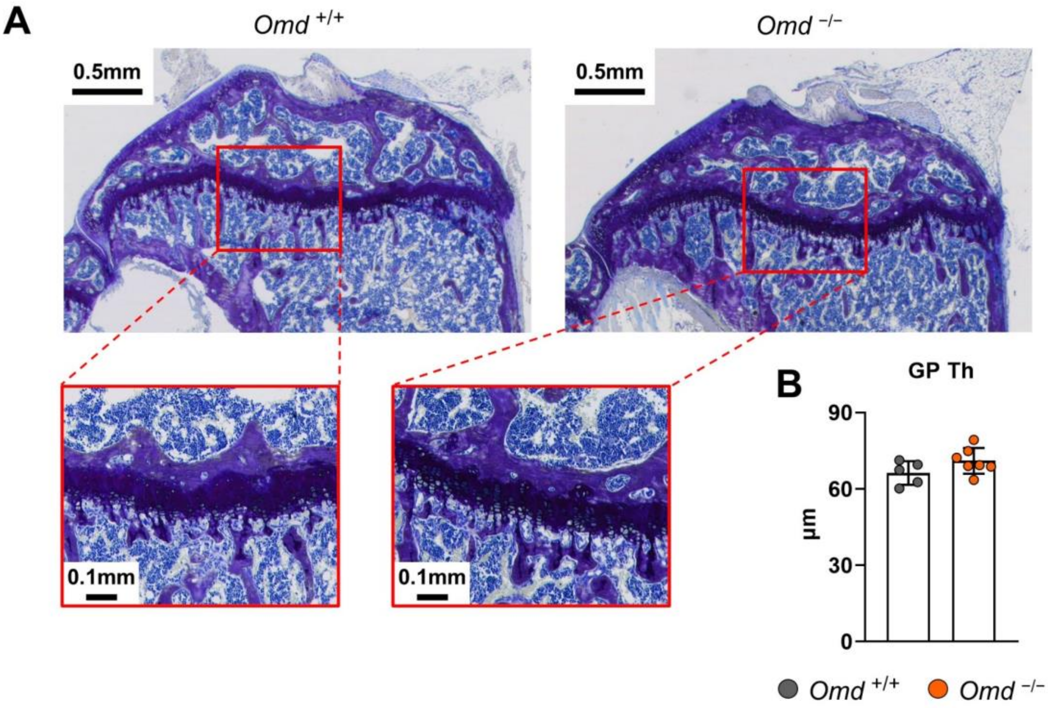

Figure 7. Influence of *Omd* deficiency on growth plate morphology. (A) Representative images and magnified details of the proximal tibial growth plate from 12-week-old female *Omd* $^{+/+}$ and *Omd* $^{-/-}$ mice. (B) Histomorphometric quantification of total growth plate thickness in tibiae of 12-week-old female *Omd* $^{+/+}$ and *Omd* $^{-/-}$ mice. Data were analyzed by Student's t-test. n=5 or 7 as represented by individual data points.

3.8 Cell-autonomous phenotype of *Omd*-deficient osteoblasts

In vitro experiments were performed to investigate if *Omd* deficiency causes any cell autonomous phenotype. Bone marrow-derived osteoblasts were isolated from 7-week-old *Omd* $^{-/-}$ mice and wildtype controls followed by osteogenic differentiation for 11 or 15 days. The mineralization capacity of osteoblasts was measured by alizarin red staining and subsequent quantification, which showed no significant difference at both time points (Fig.8A, B). Expression of *Omd* was measured by qRT-PCR, which confirmed the deficiency of the *Omd* gene in *Omd* $^{-/-}$ osteoblasts (Fig.8D). Moreover, Western Blotting for OMD confirmed the absence of the OMD protein in *Omd*-deficient primary osteoblasts which underwent 15 days of osteogenic differentiation (Fig.8C). Expression of indicated osteoblast marker genes was measured by qRT-PCR for the bone marrow-derived osteoblasts after 11 and 15 days of osteogenic differentiation. Interestingly, despite the unaffected mineralization capacity, the expression of *Runx2* and *Wnt16* was significantly decreased in *Omd* $^{-/-}$ osteoblasts at day 15 of osteogenic differentiation (Fig.8D). Since WNT16 is an essential regulator for cortical bone structures in terms of thickness and porosity [69], the cortical structure was assessed in addition to the trabecular bone in the next step.

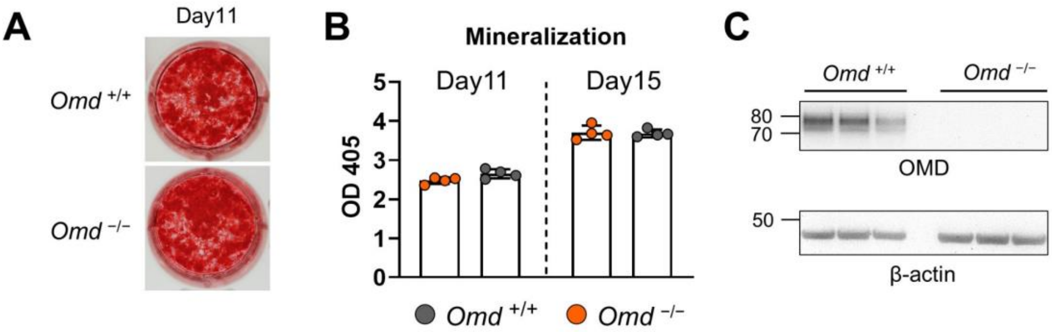

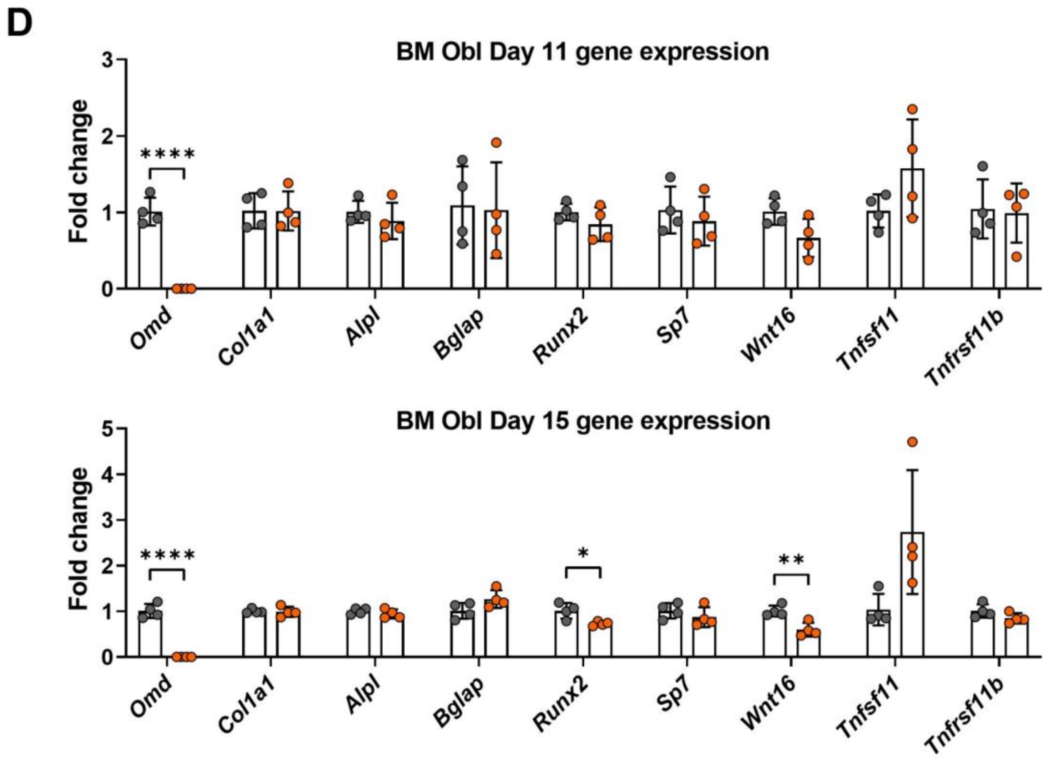

Figure 8. Cell-autonomous phenotype of *Omd*-deficient osteoblasts. (A) Representative images of alizarin red staining of bone marrow-derived osteoblasts from 7-week-old *Omd* $^{-/-}$ mice and wildtype controls after osteogenic differentiation for 11 or 15 days. (B) Quantification of mineralization after alizarin red staining. Data were analyzed by Student's t-test. n=4 for each group. (C) Images of Western Blotting for OMD with β-actin as internal control in cell lysate of bone marrow-derived osteoblasts from *Omd* $^{+/+}$ and *Omd* $^{-/-}$ mice after 15 days of osteogenic differentiation. n=3 for each group. (D) Expression analysis of bone marrow-derived osteoblasts from 7-week-old *Omd* $^{+/+}$ and *Omd* $^{-/-}$ mice for the indicated osteoblast markers after osteogenic differentiation of 11 days (upper) or 15 days (lower) as measured by qRT-PCR. Data were analyzed by Student's t-test. n=4 for each group. * $p < 0.05$, ** $p < 0.01$, **** $p < 0.0001$.

3.9 Structural phenotype of femoral trabecular bone

µCT analysis was performed to evaluate the long bone phenotype of 6-, 12- and 24-week-old female and of 12-week-old male *Omd*-deficient mice. First, the trabecular compartment was analyzed in the distal metaphysis of the right femora (Fig.9A). The trabecular parameters were obtained and analyzed including bone volume per tissue volume (BV/TV), trabecular number (Tb.N), trabecular thickness (Tb.Th), trabecular separation (Tb.Sp) and trabecular bone mineral density (Tb.TMD). Except for significantly but slightly increased Tb.Th in 12-week-old female *Omd* $^{-/-}$ mice and significantly decreased Tb.TMD in 12-week-old male *Omd* $^{-/-}$ mice, *Omd* deficiency did not cause any significant changes of parameters in all other analyzed groups (Fig.9B to D). Overall, there is no obvious trabecular bone phenotype detectable in femora of *Omd*-deficient mice.

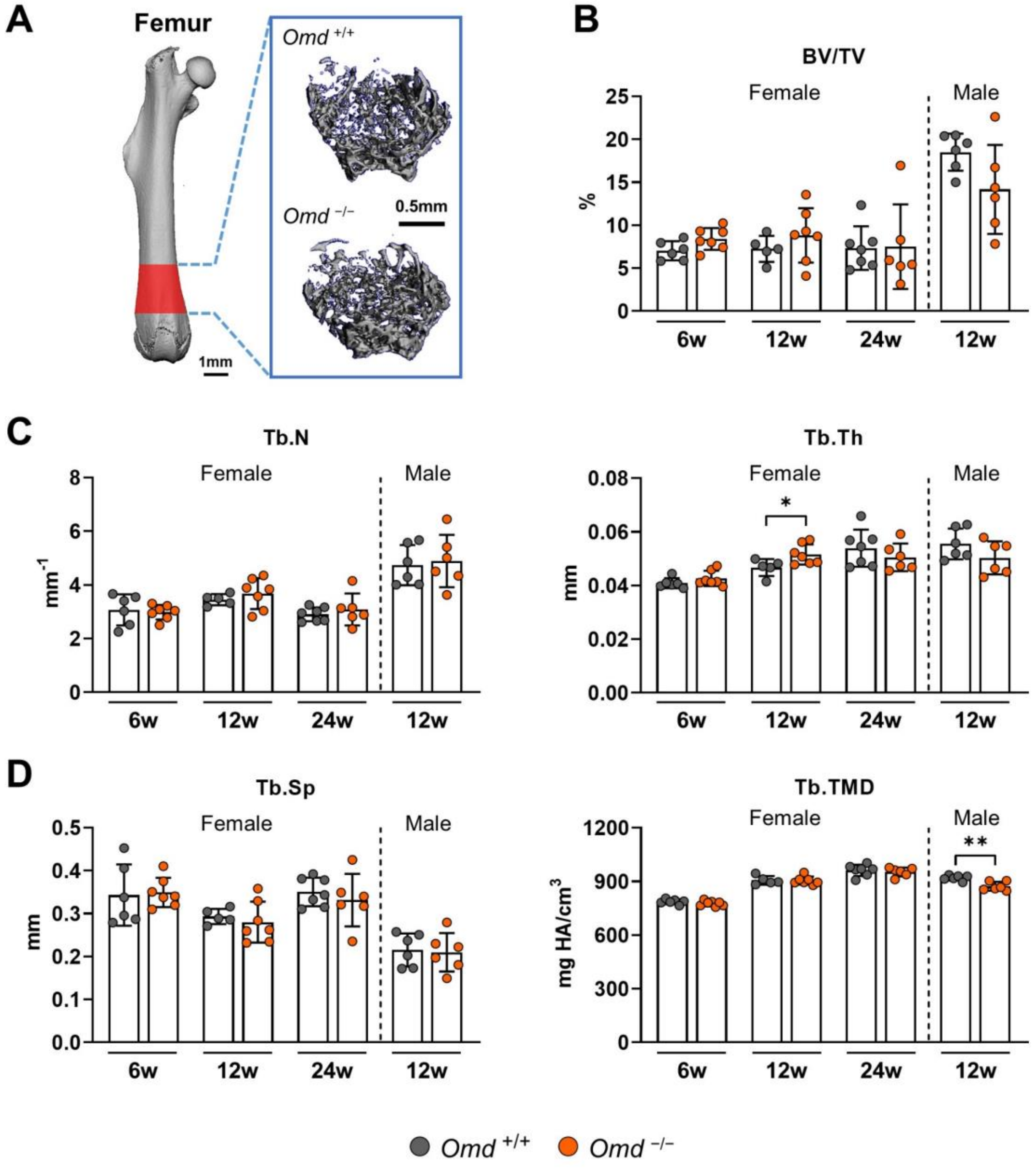

Figure 9. Structural phenotype of femoral trabecular bone. (A) Representative images of 3D reconstructions of the analyzed trabecular compartment in the distal metaphysis of the right femora of 12-week-old female *Omd* $^{+/+}$ and *Omd* $^{-/-}$ mice. The 3D reconstruction image of a complete femur is shown on the left with the red region representing the region of interest analyzed for trabecular parameters. (B to D) Parameters of the trabecular compartment of mice with the indicated gender, age and phenotype as evaluated by μCT, including bone volume per tissue volume (BV/TV), trabecular number (Tb.N), trabecular thickness (Tb.Th), trabecular seperation (Tb.Sp) and trabecular bone mineral density (Tb.TMD). Data were analyzed by Student's t-test. n=5~7 as represented by individual data points. * $p < 0.05$, ** $p < 0.01$.

3.10 Structural phenotype of femoral cortical bone

The cortical compartment of the femoral mid-diaphysis was analyzed by µCT in 6-, 12- and 24-week-old female and 12-week-old male *Omd*-deficient mice (Fig.10A). The following parameters were measured: Cortical thickness (Ct.Th), inner diameter, outer diameter and cortical porosity (Ct.Por). The length of the whole femur was determined as well. (Fig.10B to D) Interestingly, both inner and outer diameters were significantly decreased in *Omd*-deficient mice, which can also be observed on the reconstructed 3D images (Fig.10A), except for outer diameter of 6-week-old female mice. Moreover, the only significant difference among other parameters is that 12-week-old female *Omd* $^{-/-}$ mice have slightly higher Ct.Th. Therefore, *Omd* deficiency leads to a consistent slender bone phenotype in femora without obviously altering cortical thickness, porosity and femur length.

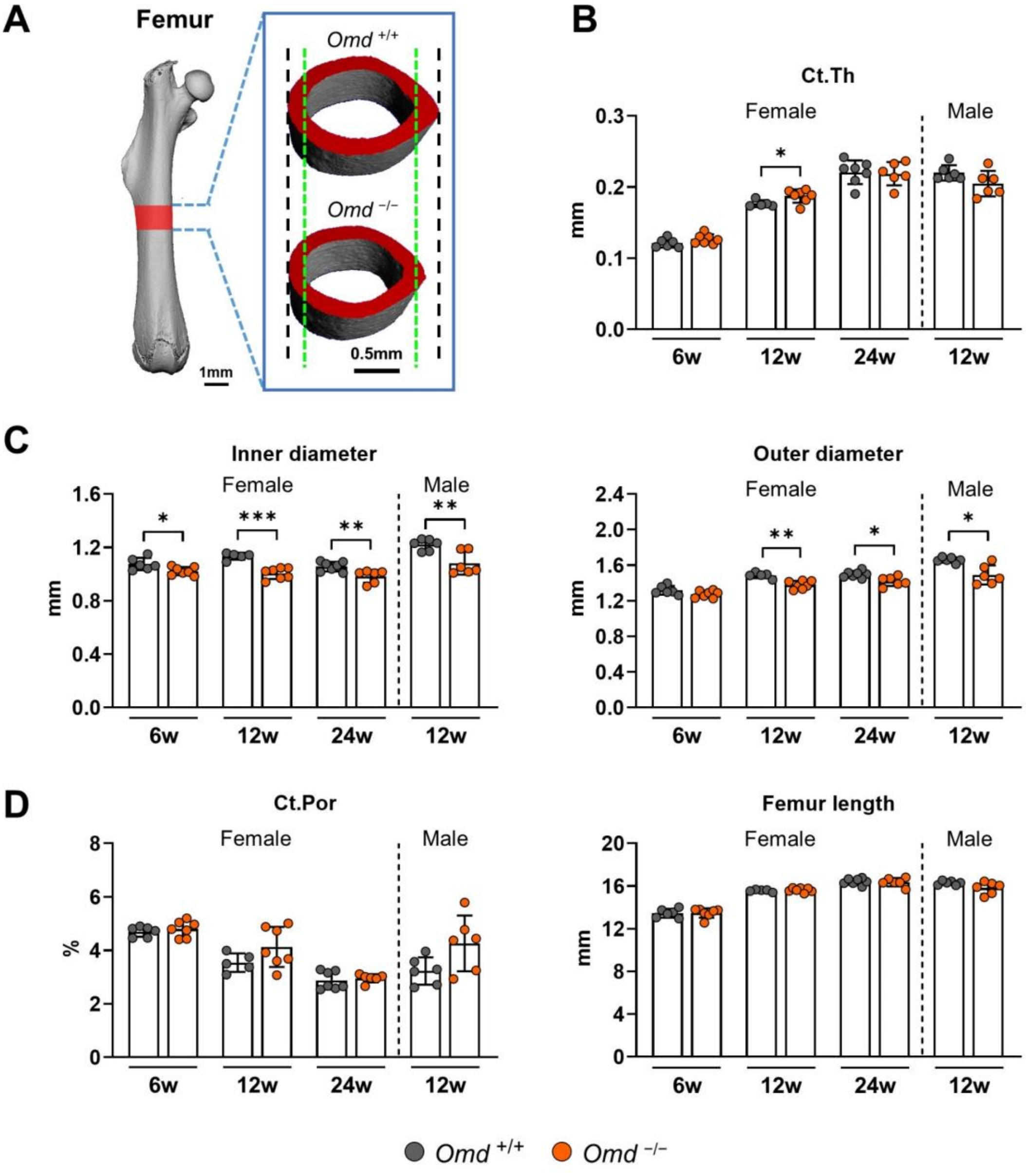

Figure 10. Structural phenotype of femoral cortical bone. (A) Representative images of 3D reconstructions of the analyzed cortical compartment from the mid-diaphysis of the right femora of 12-week-old female *Omd* $^{+/+}$ and *Omd* $^{-/-}$ mice. The green and black dashed lines show the ranges of inner and outer diameters of *Omd* $^{+/+}$ femur respectively. The 3D reconstruction image of complete femur is shown on the left with the red region representing the analyzed cortical bone. (B to D) Parameters of the cortical compartment of mice with the indicated gender, age and phenotype as measured by μCT evaluation, including cortical thickness (Ct.Th), inner diameter, outer diameter, cortical porosity (Ct.Por) and whole femur length. Data were analyzed by Student's t-test. n=5~7 as represented by individual data points. * $p < 0.05$, ** $p < 0.01$, *** $p < 0.001$.

3.11 Structural phenotype of tibial and humeral cortical bone

Since the slender bone phenotype was observed in femora of *Omd*-deficient mice, the mid-diaphyseal cortical compartment of other representative long bones (i.e. tibiae and humeri) from 12-week-old female *Omd* $^{+/+}$ and *Omd* $^{-/-}$ mice were further analyzed by µCT (Fig.11A). Cortical thickness (Ct.Th), inner diameter, outer diameter and cortical porosity (Ct.Por) were analyzed as well as length of the whole tibia and humerus (Fig.11B to D). For tibiae, similar to femora, Ct.Th is significantly but slightly increased in *Omd* $^{-/-}$ mice. Most importantly, both inner and outer diameters were consistently and significantly decreased in tibiae and humeri of *Omd*-deficient mice, without influencing cortical porosity and bone length. Therefore, the slender bone phenotype is stable and consistent in different long bones.

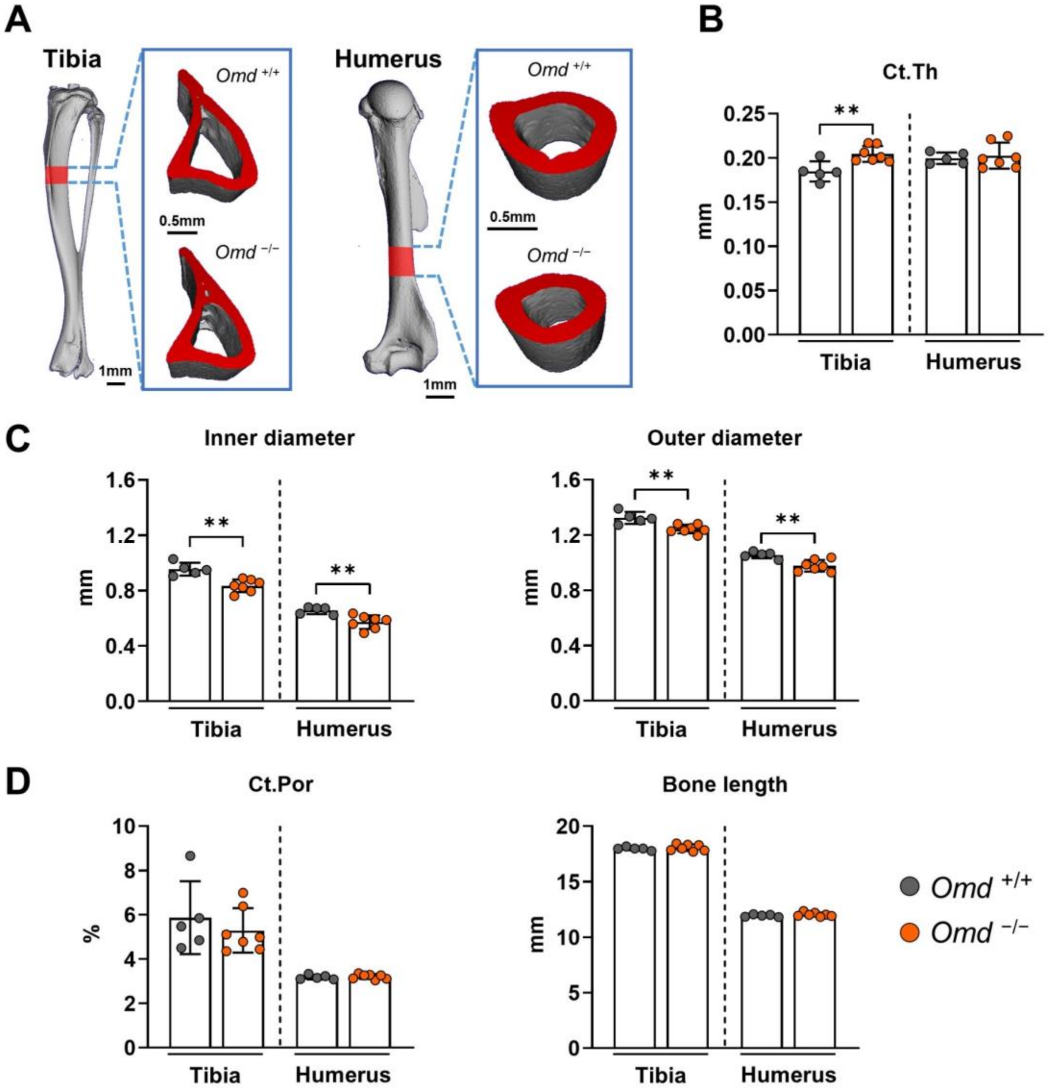

Figure 11. Structural phenotype of tibial and humeral cortical bone. (A) Representative 3D reconstruction images of the analyzed cortical compartment from mid-diaphysis of the left tibiae (left part) and humeri (right part) of 12-week-old female *Omd* $^{+/+}$ and *Omd*

$^{-/-}$ mice. The 3D reconstruction images of full tibia and humerus are shown adjacently with the red highlights representing the analyzed cortical region. (B to D) Cortical parameters measured by μCT, including cortical thickness (Ct.Th), inner diameter, outer diameter and cortical porosity (Ct.Por) as well as the length of the whole tibia and humerus. Data were analyzed by Student’s t-test. n=5 or 7 as represented by individual data points. ** $p < 0.01$.

3.12 Dynamic histomorphometric analysis of femoral cortical bone of *Omd*-deficient mice

Cortical bone formation rate is a critical factor that influences the cortical diameters. Since 12- and 24-week-old female *Omd*-deficient mice displayed a consistent slender bone phenotype in their femora, I focused on femoral cortical bone formation rate for the next step. However, when taking a closer look at the diameters, in either female *Omd* $^{+/+}$ or *Omd* $^{-/-}$ mice, 24-week-old mice have larger outer diameter but smaller inner diameter than 12-week-old ones. When comparing the age-dependent difference in diameters, it was similar for both genotypes, indicating that the cortical bone formation rate of *Omd* $^{+/+}$ and *Omd* $^{-/-}$ mice from 12 weeks until 24 weeks of age is possibly similar. However, at the age of 6 weeks, female *Omd*-deficient mice display only significantly decreased inner diameter, which let us deduce that the phenotype regarding cortical bone formation rate occurs at a younger age. Thus, the dynamic histomorphometry analysis of femoral cortical bone was performed for 6-week-old female mice in the transversal plane of the mid-diaphysis for both endocortical and periosteal surfaces. While the parameters including mineralizing surface per bone surface (MS/BS), mineral apposition rate (MAR) and bone formation rate (BFR/BS) are homogenous on endocortical surface without significant difference between *Omd* $^{+/+}$ and *Omd* $^{-/-}$ mice (Fig.12A), the parameters on periosteal surface were unfortunately highly variable (Fig.12B). The main cause is that there are more damaged regions at the periosteal surface, leading to unreliable measurements. Overall, no influence of *Omd* deficiency on femoral cortical bone formation rate was observed in 6-week-old female mice.

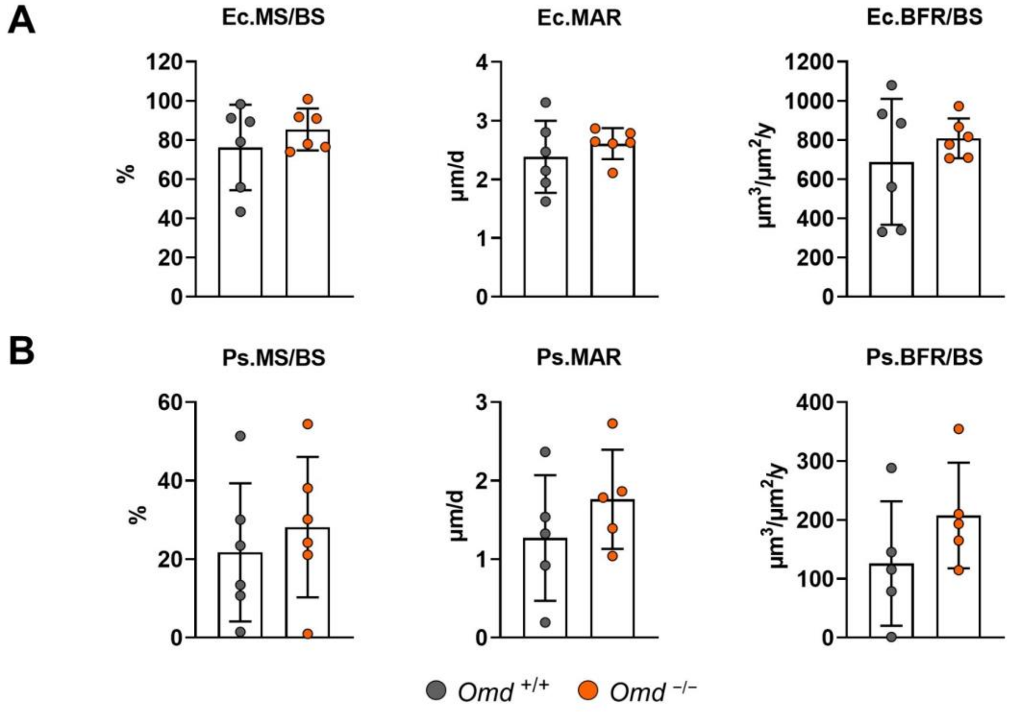

Figure 12. Dynamic histomorphometric analysis of femoral cortical bone of *Omd*-deficient mice. (A) Parameters of the endocortical surface as determined in the transversal plane of the mid-diaphysis of 6-week-old female *Omd* $^{+/+}$ and *Omd* $^{-/-}$ mice, including mineralizing surface per bone surface (MS/BS), mineral apposition rate (MAR) and bone formation rate (BFR/BS). (B) The same histomorphometric parameters determined at the periosteal surface. Data were analyzed by Student's t-test. n=5 or 6 as represented by individual data points. One sample in each group were removed when calculating Ps.MAR and Ps.BFR/BS due to insufficient double labels.

3.13 Calvarial phenotype of *Omd*-deficient mice

The calvarial phenotype was also evaluated as part of the thorough skeletal phenotyping of 12-week-old female *Omd*-deficient mice. There was no significant difference between *Omd* $^{+/+}$ and *Omd* $^{-/-}$ mice regarding calvarial thickness (Fig.13A) and porosity (Fig.13B) as measured by µCT analysis.

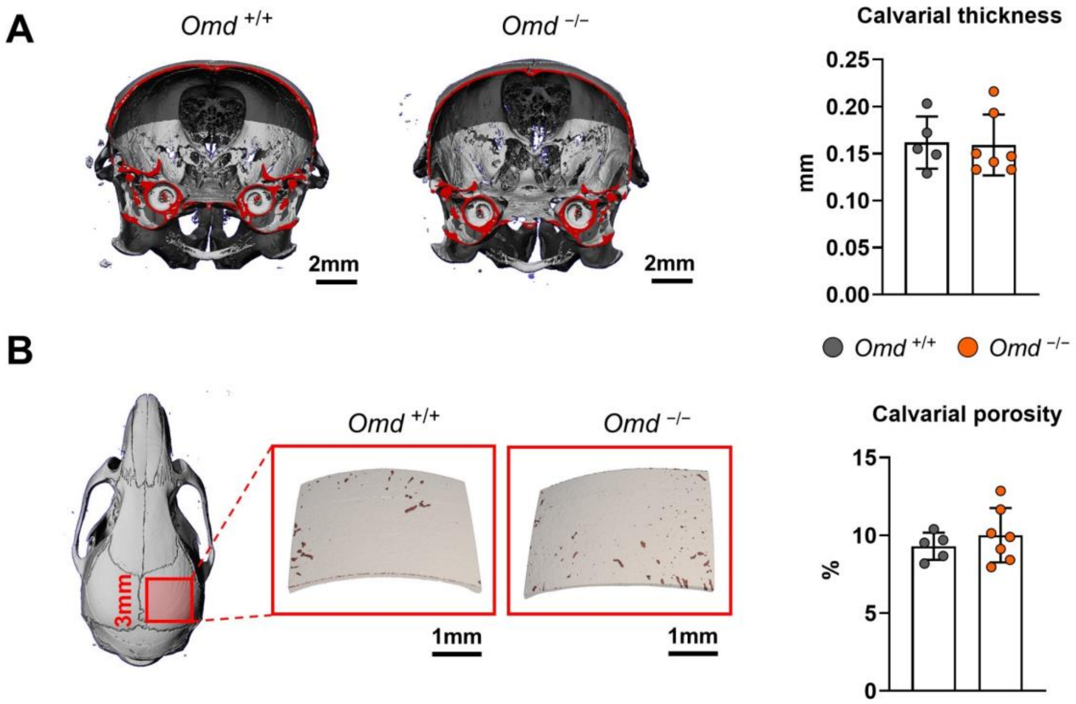

Figure 13. Calvarial phenotype of *Omd*-deficient mice. (A) Representative reconstructed µCT 3D images of of skulls from 12-week-old female *Omd* $^{+/+}$ and *Omd* $^{-/-}$ mice in the posterior rostral visual axis with a virtual coronal cut plane indicated in red (left part). Quantification of calvarial thickness in the anatomical plane indicated by the representative images (right part). (B) Representative images of calvaria from 12-week-old female *Omd* $^{+/+}$ and *Omd* $^{-/-}$ mice with pores highlighted in red (in large red box). The analyzed region of interest is indicated on the skull on the left. Quantification of the calvarial porosity in the analyzed region (right part). Data were analyzed by Student’s t-test. n=5 or 7 as represented by individual data points.

3.14 Mechanical properties of *Omd*-deficient bones

Based on the proposed function of OMD as well as the finding that *Omd* deficiency altered the long bone structure, the next aim of my study was investigating the mechanical properties of the bones from *Omd*-deficient mice. Three-point-bending test was performed on the femora of 12-week-old female *Omd*-deficient and wildtype mice. Material stiffness (represented by elastic modulus), the maximum load applied and the flexural strength were measured, among which only flexural strength was significantly increased by *Omd* deficiency (Fig.14A). Due to the difference of geometry between *Omd* $^{+/+}$ and *Omd* $^{-/-}$ mice, the section modulus and flexural stiffness were calculated to reflect the details of mechanical properties more accurately. In line with the difference of transversal dimension, section modulus and flexural stiffness were significantly decreased in *Omd* $^{-/-}$ mice (Fig.14B). Furthermore, nanoindentation was performed on the tibial cortical bone to measure the material properties of compression. Here, the hardness and modulus were unaffected by *Omd* deficiency (Fig.14C). Taken together, the significant differences of the measured parameters are rather the consequence of geometric difference between *Omd* $^{+/+}$ and *Omd* $^{-/-}$ mice instead of changed material mechanical properties.

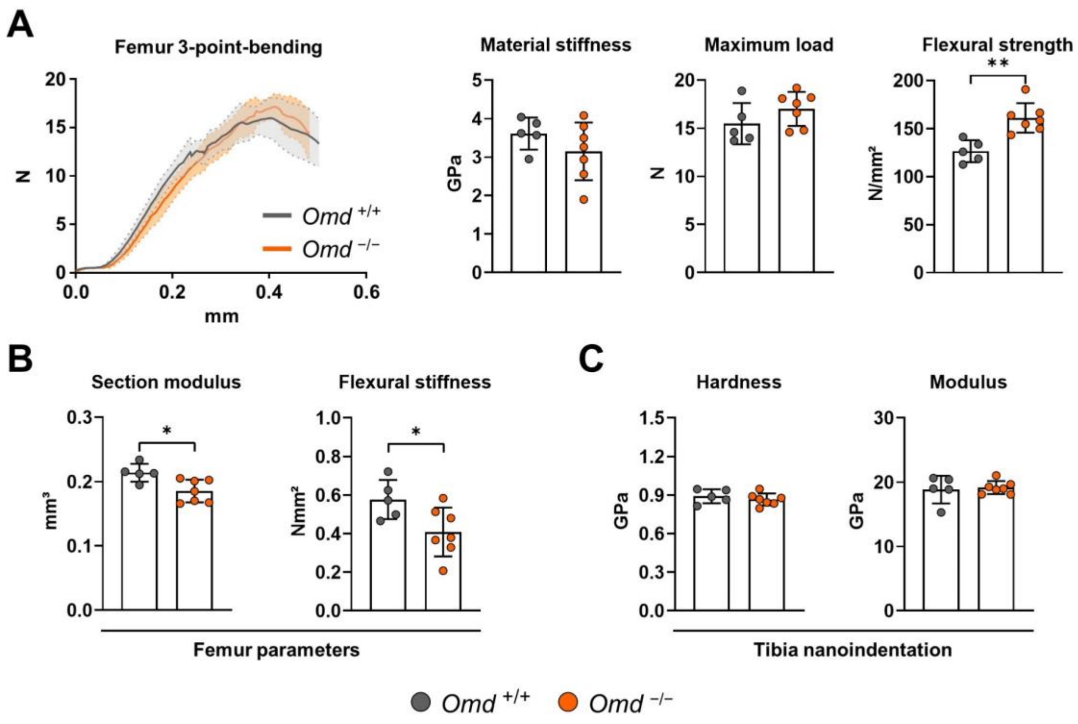

Figure 14. Mechanical properties of *Omd*-deficient bones. (A) Load-displacement curves of the three-point-bending test performed on the explanted femora of 12-week-old female *Omd* $^{+/+}$ and *Omd* $^{-/-}$ mice. Solid lines represent the mean value while the shaded areas denote the standard deviation (left part). Material stiffness, maximum load applied, flexural strength as determined by three-point-bending test (right part).

(B) Section modulus and flexural stiffness of femora measured by three-point-bending test in combination with geometric parameters of µCT evaluation. (C) Evaluation of bone matrix material hardness and modulus by nanoindentation for cortical compartment of tibiae from 12-week-old female *Omd* $^{+/+}$ and *Omd* $^{-/-}$ mice. Data were analyzed by Student's t-test. n=5 or 7 as represented by individual data points. * $p < 0.05$, ** $p < 0.01$.

3.15 Microstructural analysis of bone matrix

Based on previous studies demonstrating the ability of OMD to regulate type I collagen assembly *in vitro* [31], circular polarized light imaging was performed to assess if the order of collagen fibers is influenced by *Omd* deficiency. Images from undecalcified tibiae with Toluidine blue staining were obtained from 12-week-old female *Omd* $^{+/+}$ and *Omd* $^{-/-}$ mice (Fig.15A). Quantification of fiber coherency on both medial and lateral sides of tibial cortex revealed no significant differences between *Omd*-deficient and wildtype bones (Fig.15B).

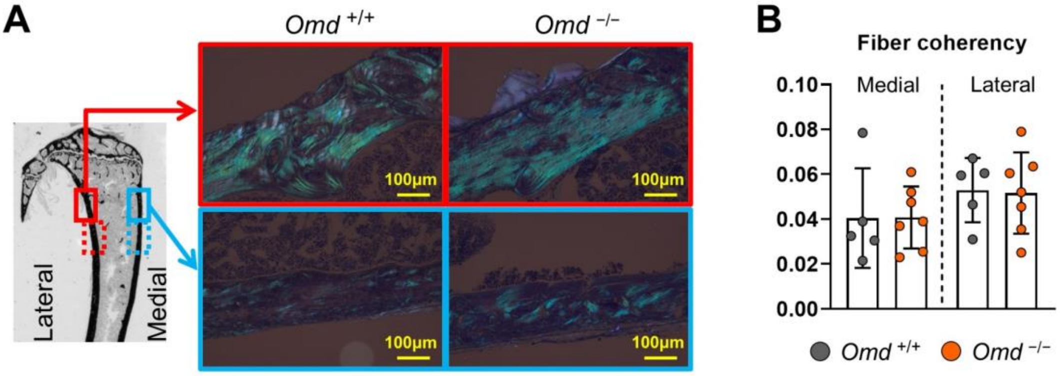

Figure 15. Microstructural analysis of bone matrix. (A) Representative images of circular polarized light imaging of right tibia on undecalcified section of tibiae with Toluidine blue staining from 12-week-old female *Omd* $^{+/+}$ and *Omd* $^{-/-}$ mice. The analyzed cortical regions of interest (4 regions per mouse) are marked in small boxes on the overview section of tibia (left part) with the magnified details on the right. (B) Quantification of fiber coherency. Data were analyzed by Student's t-test. n=5 or 7 as represented by individual data points. * $p < 0.05$, ** $p < 0.01$.

3.16 Calcium content analysis of bone matrix

Next, quantitative backscattered electron imaging (qBEI) was performed to evaluate the influence of *Omd* deficiency on the calcium content of the tibial cortical bone matrix in 12-week-old female *Omd* $^{+/+}$ and *Omd* $^{-/-}$ mice (Fig.16A, B). No significant differences were observed regarding the mean calcium content (Ca Mean), the most frequently occurring calcium concentration (Ca Peak), as well as the calcium content variance (Ca.Width). Additionally, this method allowed for a precise determination of the number of osteocyte lacunae (N.Ot.Lc/B.Ar) with no difference being observed between *Omd* $^{+/+}$ and *Omd* $^{-/-}$ mice (Fig.16C).

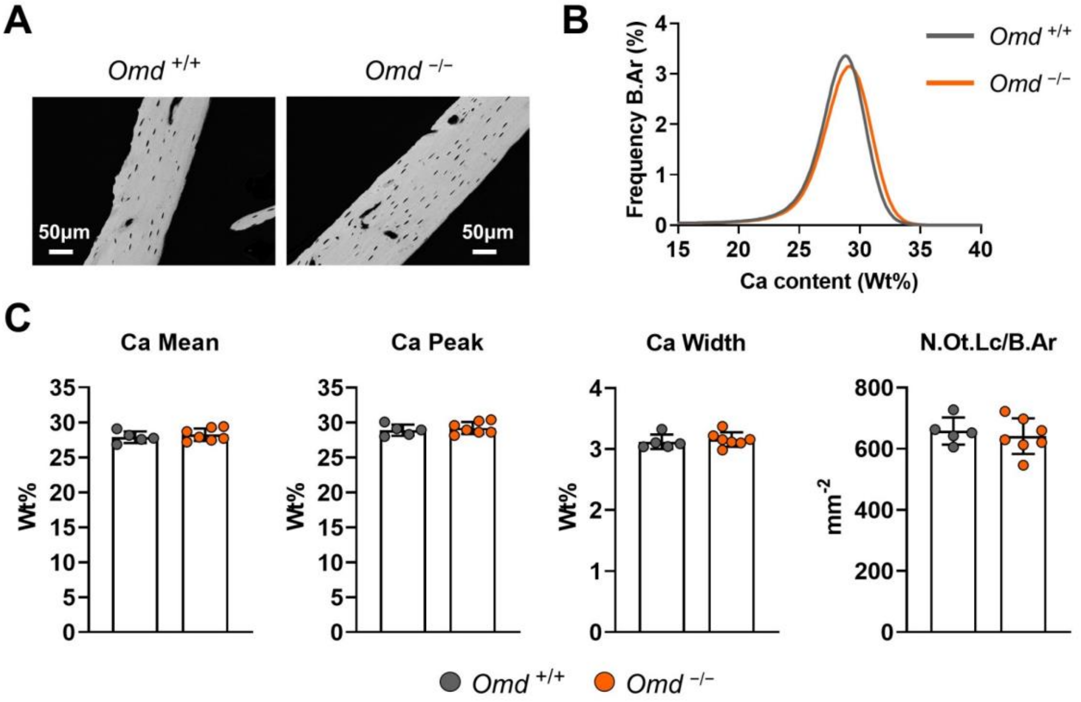

Figure 16. Calcium content analysis of bone matrix. (A) Representative backscattered electron images of the proximal metaphyseal cortical region of tibiae from 12-week-old female *Omd* $^{+/+}$ and *Omd* $^{-/-}$ mice. (B) Quantitative backscattered electron imaging analysis of the bone matrix calcium content presented as histograms of the calcium density distribution. (C) Quantification of relevant calcium content parameters including the weighted mean calcium content (Ca Mean), the most frequently observed calcium concentration (Ca Peak) and the variance of the calcium content (Ca.Width), as well as the relative number of osteocyte lacunae (N.Ot.Lc/B.Ar) in the analyzed cortical region. Data were analyzed by Student's t-test. n=5 or 7 as represented by individual data points.

3.17 Nanostructural analysis of bone matrix

To assess the nanostructure of femoral cortical surface, atomic force microscopy analysis was performed on 12-week-old female *Omd* $^{+/+}$ and *Omd* $^{-/-}$ mice. Semi-quantitative evaluation was performed to determine the percentage of specific nanostructural features with corresponding classifications. No heterogenous surface was observed in *Omd* $^{+/+}$ femora, whereas on average more than 15% of the analyzed surfaces appeared heterogenous in *Omd*-deficient mice, which translated into a significantly less homogenous cortical surface in *Omd* $^{-/-}$ femora (Fig.17 left panel). While more loosely packed fibrils were observed in *Omd* $^{-/-}$ femora compared to *Omd* $^{+/+}$ femora (approx. 10% vs 0%), the mean value did not reach a statistical significance (Fig.17 middle panel). Parallelism of fibril was not affected by *Omd* deficiency (Fig.17 right panel). Overall, despite the unchanged collagen fiber microstructure as determined by polarized light microscopy, collagen fibrils at the nanostructural level were altered by *Omd* deficiency.

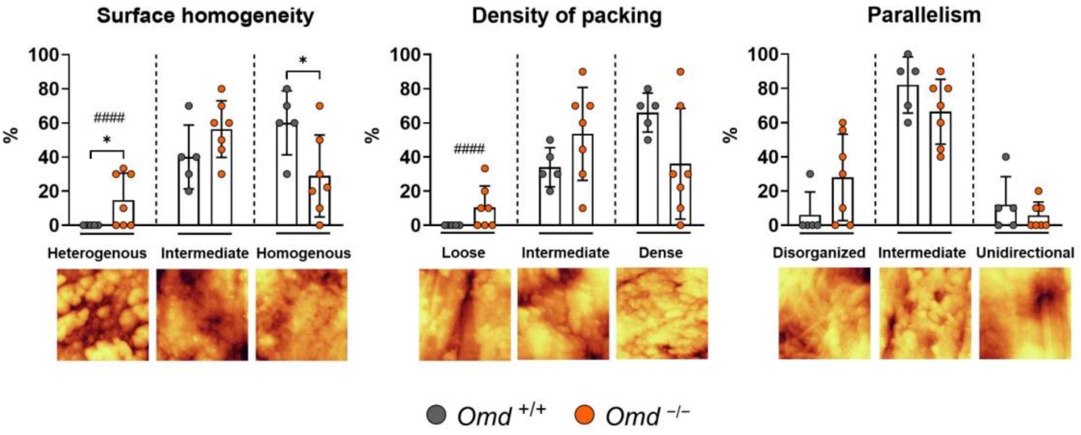

Figure 17. Nanostructural analysis of bone matrix. Nano-structural analysis of femoral surface by atomic force microscopy of 12-week-old female *Omd* $^{+/+}$ and *Omd* $^{-/-}$ mice. Semi-quantitative evaluation was performed to assess nano-structural features (i.e. surface homogeneity, fibril packing density and parallelism). Data are presented as percentage of images per animal (at least 10 images per mouse) with the indicated feature classifications (such as heterogenous, intermediate and homogenous). Representative images (2×2µm) for nano-structural features of different classifications are shown underneath the graphs. Data were analyzed by Student's t-test or Welch's t-test if there was a significant difference in variance (determined by F-test, #### $p < 0.0001$). n=5 or 7 as represented by individual data points. * $p < 0.05$.

3.18 Effect of *Omd* deficiency on WNT1-induced trabecular bone formation in vertebral bodies

Based on the previous findings, one major aim of my thesis was to investigate if OMD influences the bone anabolic function of WNT1. Thus, *Omd*-deficient mice were crossed with a previously reported mouse line carrying the osteoblastic inducible *Wnt1* transgene [23]. Structural histomorphometry was performed in the trabecular compartment of the lumbar vertebral bodies L3 and L4 after no, 1 week or 3 weeks of *Wnt1* gene induction (by doxycycline removal from the diet) until sacrifice at the age of 12 weeks (Fig.18A). Since the analyzed mice were obtained from different colonies, comparisons were made only within the same *Omd*-genotype. The bone formation caused by *Wnt1* transgene induction displayed a time-dependent pattern, as expected from previously published data [23]. Moreover, it is obvious that *Omd* deficiency did not impair the effect of WNT1 during bone formation as the change in key structural parameters was highly similar independent of the *Omd*-genotype (Fig.18B).

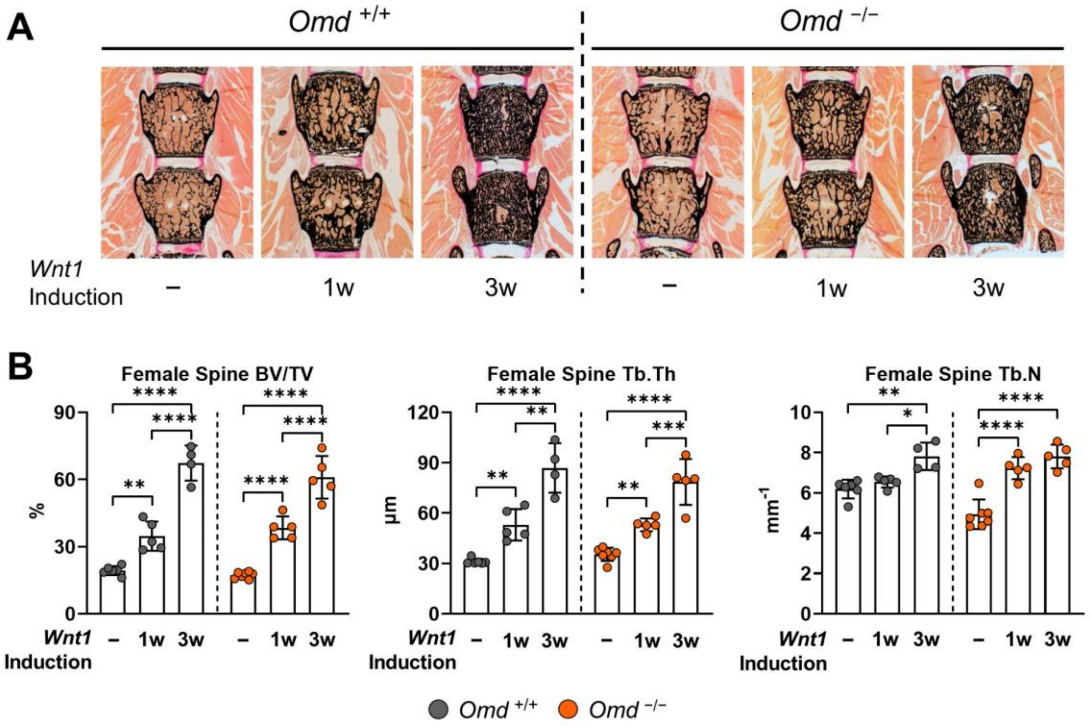

Figure 18. Effect of *Omd* deficiency on WNT1-induced trabecular bone formation in vertebral bodies (A) Representative images of undecalcified sections of vertebral bodies L3 and L4 with von Kossa/van Gieson staining from female *Omd* $^{+/+}$ and *Omd* $^{-/-}$ mice carrying the osteoblast-specific inducible *Wnt1* transgene with no, 1 or 3 weeks of the *Wnt1* gene induction until sacrifice at the age of 12 weeks. (B) Parameters of histomorphometric analysis performed on the trabecular compartment of L3 and L4, including bone volume per tissue volume (BV/TV), trabecular thickness (Tb.Th) and trabecular number (Tb.N). Data were analyzed by one-way ANOVA with Tukey's

multiple comparison test under either *Omd* $^{+/+}$ or *Omd* $^{-/-}$ condition. n=4~7 as represented by individual data points. * $p < 0.05$, ** $p < 0.01$, *** $p < 0.001$, **** $p < 0.0001$.

3.19 Effect of *Omd* deficiency on WNT1-induced trabecular bone formation in tibiae

Structural histomorphometric analysis was performed on undecalcified tibia sections as well to evaluate the trabecular compartment of proximal diaphysis for the mice described above (Fig.19A). Similar to vertebral bodies, the bone anabolic effect of WNT1 was not influenced by *Omd* deficiency in tibiae (Fig.19B).

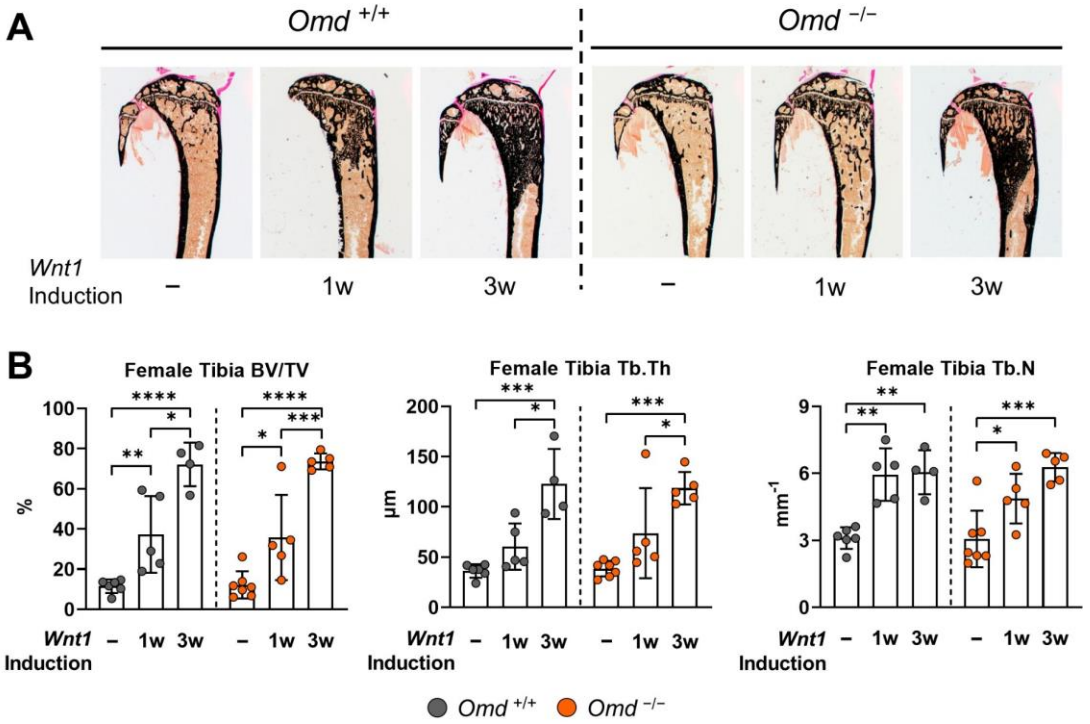

Figure 19. Effect of *Omd* deficiency on WNT1-induced trabecular bone formation in tibiae. (A) Representative images of undecalcified sections of tibiae with von Kossa/van Gieson staining from female *Omd* $^{+/+}$ and *Omd* $^{-/-}$ mice carrying the osteoblast-specific inducible *Wnt1* transgene with no, 1 or 3 weeks of the *Wnt1* gene induction until sacrifice at the age of 12 weeks. (B) Parameters of histomorphometric analysis performed on the trabecular compartment of proximal diaphysis, including bone volume per tissue volume (BV/TV), trabecular thickness (Tb.Th) and trabecular number (Tb.N). Data were analyzed by one-way ANOVA with Tukey's multiple comparison test under either *Omd* $^{+/+}$ or *Omd* $^{-/-}$ condition. n=4~7 as represented by individual data points. * $p < 0.05$, ** $p < 0.01$, *** $p < 0.001$, **** $p < 0.0001$.

3.20 Effect of *Omd* deficiency on WNT1-induced cortical bone formation and mechanical properties of femora

Since WNT1 also induces bone formation of cortical bone, the influence of *Omd* deficiency on WNT1-induced cortical bone formation was measured in femora by µCT analysis for female *Omd* $^{+/+}$ and *Omd* $^{-/-}$ mice carrying the osteoblast-specific inducible *Wnt1* transgene with no or 3 weeks of *Wnt1* gene induction until sacrifice at the age of 12 weeks (Fig.20A). The overexpression of *Wnt1* increased cortical thickness of femoral mid-diaphysis significantly to a similar extent in *Omd* $^{+/+}$ and *Omd* $^{-/-}$ mice (Fig.20B). The inner diameter of the analyzed cortical compartment remained unchanged, while the outer diameter was significantly increased by the induction of WNT1 (Fig.20C).

Three-point-bending test was performed to assess the mechanical properties of the explanted femora after µCT analysis. As expected, maximum load applied increased significantly after WNT1 induction for 3 weeks (Fig.20D left panel). Interestingly, despite a marked change of bone matrix after WNT1 induction, the flexural strength was unchanged in *Omd* $^{+/+}$ mice, whereas it was significantly increased in *Omd* $^{-/-}$ mice, suggesting that OMD may have a moderate influence on inherent bone matrix mechanical properties (Fig.20D right panel), such as the regulation of heterogeneity of collagen fibrils as measured by atomic force microscopy before (Fig.17).

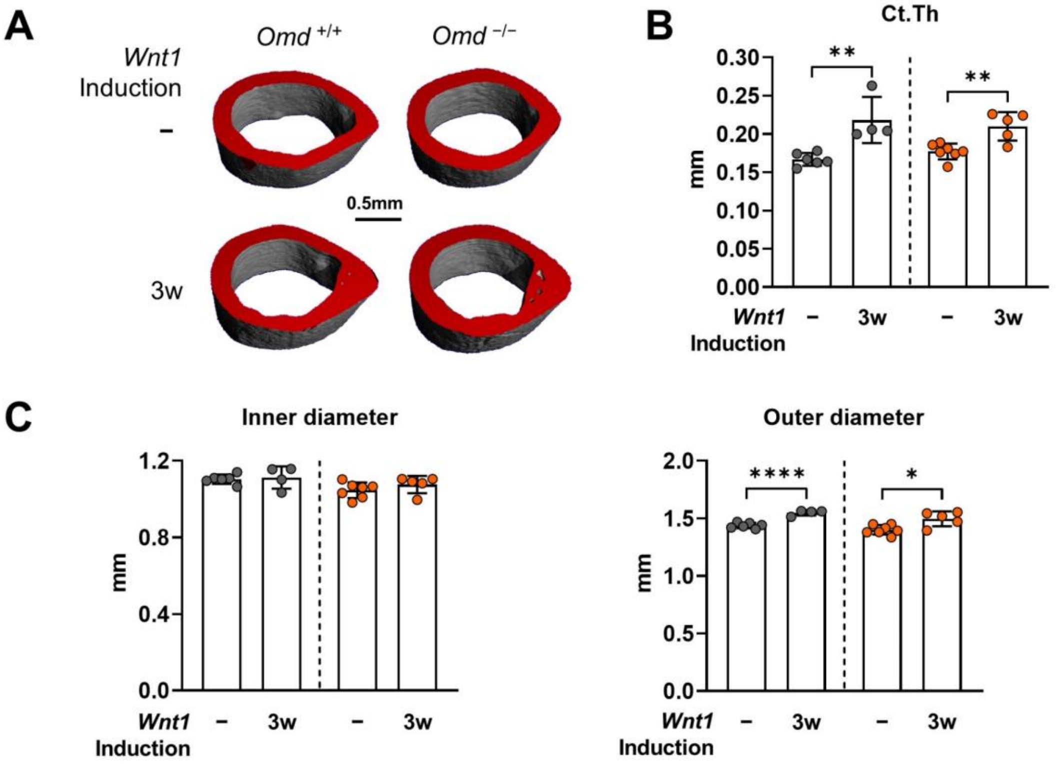

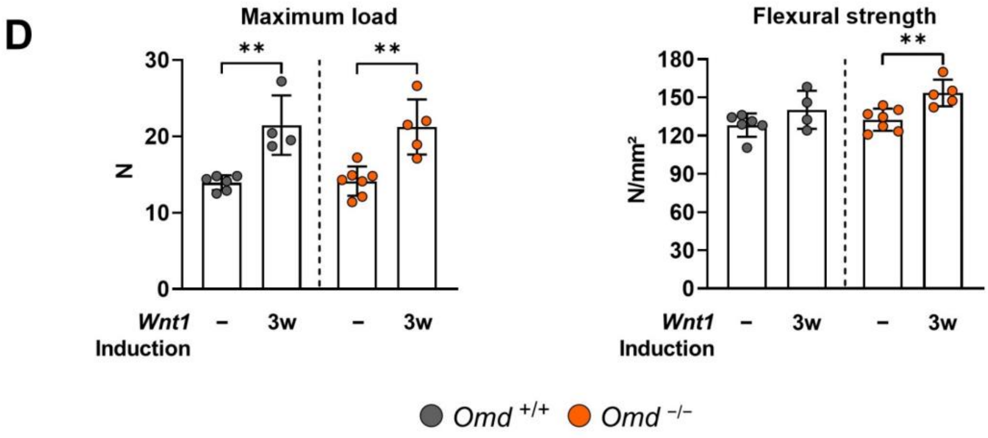

Figure 20. Effect of *Omd* deficiency on WNT1-induced cortical bone formation and mechanical properties of femora. (A) Representative μCT 3D reconstruction images of mid-diaphyseal cortical compartment of right femora from female *Omd* $^{+/+}$ and *Omd* $^{-/-}$ mice carrying the osteoblast-specific inducible *Wnt1* transgene with no or 3 weeks of *Wnt1* gene induction until sacrifice at the age of 12 weeks. (B) Cortical thickness (Ct.Th) and (C) inner and outer diameter of the cortical compartment measured by μCT for the 12-week-old female mice with indicated genotypes and *Wnt1* induction status. (D) Mechanical parameters including maximum load applied and flexural strength as determined by three-point-bending test on the femora after μCT analysis. Data were analyzed by Student's t-test under either *Omd* $^{+/+}$ or *Omd* $^{-/-}$ circumstance. n=4~7 as represented by individual data points. * $p < 0.05$, ** $p < 0.01$, **** $p < 0.0001$.

3.21 Effect of *Sfrp1* deficiency on WNT1-induced trabecular bone formation in vertebral bodies

In previous experiments, ST2 cells were responsive to the stimulation with the recombinant WNT1/SFRP1 complex. It was indicated previously that SFRP1 improves the solubility and stability of WNT1 [33]. Therefore, to investigate, if SFRP1 is necessary for the bone anabolic function of WNT1 *in vivo*, we crossed the *Sfrp1*-deficient (*Sfrp1* $^{-/-}$) mice with mice carrying the osteoblast-specific inducible *Wnt1* transgene [23]. A preliminary histomorphometric analysis of the trabecular compartment was performed on undecalcified sections of vertebral bodies L3 and L4 from female *Sfrp1* $^{+/+}$ and *Sfrp1* $^{-/-}$ mice carrying the osteoblast-specific inducible *Wnt1* transgene with no or 1 week of the *Wnt1* gene induction until sacrifice at the age of 12 weeks (Fig.21A). The induction of *Wnt1* significantly induced trabecular bone mass to a comparable level in the presence or absence of SFRP1 (Fig.21B). Although after WNT1 induction, trabecular thickness (Tb.Th) of *Sfrp1* $^{-/-}$ mice did not reach a statistical difference, the overall increase of bone volume per tissue volume (BV/TV) was not altered compared to WNT1-induced *Sfrp1* $^{+/+}$ mice. Hence, an influence of *Sfrp1* deficiency on the osteoanabolic effect of WNT1 was not observed.

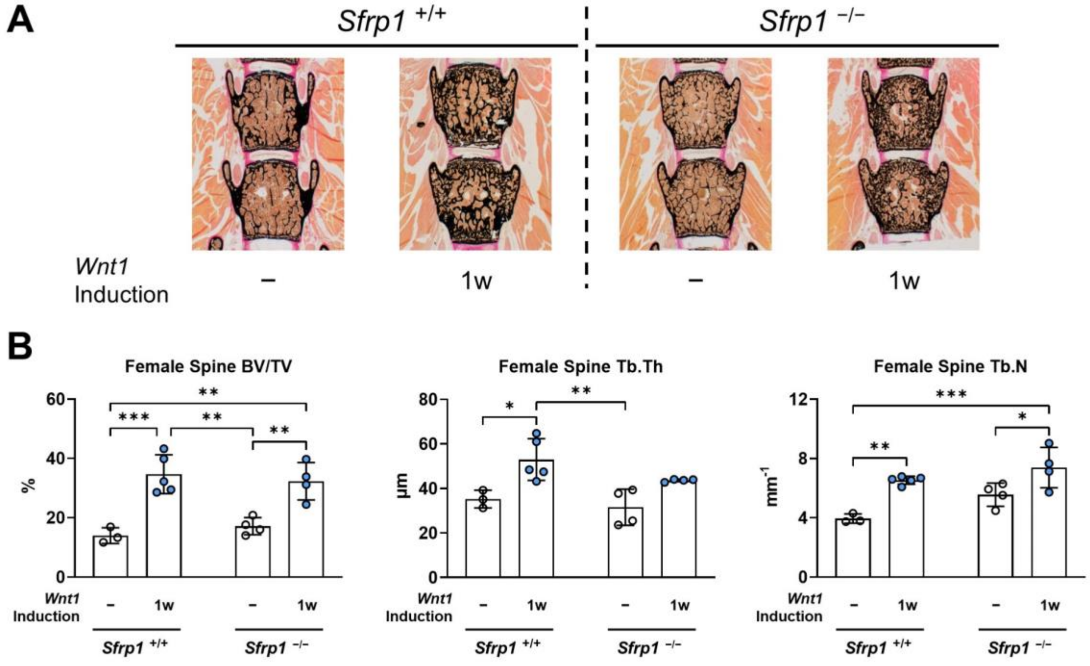

Figure 21. Effect of *Sfrp1* deficiency on WNT1-induced trabecular bone formation in vertebral bodies. (A) Representative images of undecalcified sections of vertebral bodies L3 and L4 with von Kossa/van Gieson staining from female *Sfrp1* $^{+/+}$ and *Sfrp1* $^{-/-}$ mice carrying the osteoblastic inducible *Wnt1* transgene with no or 1 week of the *Wnt1* gene induction until sacrifice at the age of 12 weeks. (B) Results of histomorphometric analysis performed on the trabecular compartment of vertebral bodies L3 and L4, including bone volume per tissue volume (BV/TV), trabecular

thickness (Tb.Th) and trabecular number (Tb.N). Data were analyzed by two-way ANOVA with Tukey's multiple comparison test. n=3~5 as represented by individual data points. * $p < 0.05$, ** $p < 0.01$, *** $p < 0.001$.

3.22 Preliminary investigation of the influence of *Fzd4* deficiency on WNT1-induced trabecular bone formation in vertebral bodies

In my medical doctor dissertation, based on gene expression studies, I hypothesized that FZD4 is a potential receptor of WNT1. Therefore, we introduced a *Fzd4*-deficiency allele into the mouse line carrying the osteoblast-specific inducible *Wnt1* transgene [23] by crossbreeding to test this hypothesis. Unfortunately, homozygous *Fzd4* deficiency caused high postnatal lethality that was in line with previously reported studies [70]. Therefore, only a small number of animals could be analyzed in the context of this dissertation. Preliminary histomorphometric analysis of the trabecular compartment was performed on undecalcified sections of vertebral bodies (L3 and L4) of 5-week-old *Fzd4* $^{+/+}$, *Fzd4* $^{+/-}$ and *Fzd4* $^{-/-}$ mice as well as *Fzd4* $^{-/-}$ mice carrying the osteoblast-specific inducible *Wnt1* transgene with 7 days of the *Wnt1* gene induction until sacrifice at the age of 5 weeks (Fig.22A). Although statistical analysis was not feasible yet, we could observe that the trabecular bone mass (i.e. BV/TV) was clearly increased after *Wnt1* induction (approx. doubled) also in the absence of *Fzd4* (Fig.22B). Hence, *Fzd4* deficiency most likely did not attenuate the effect of WNT1-dependent bone formation.

A

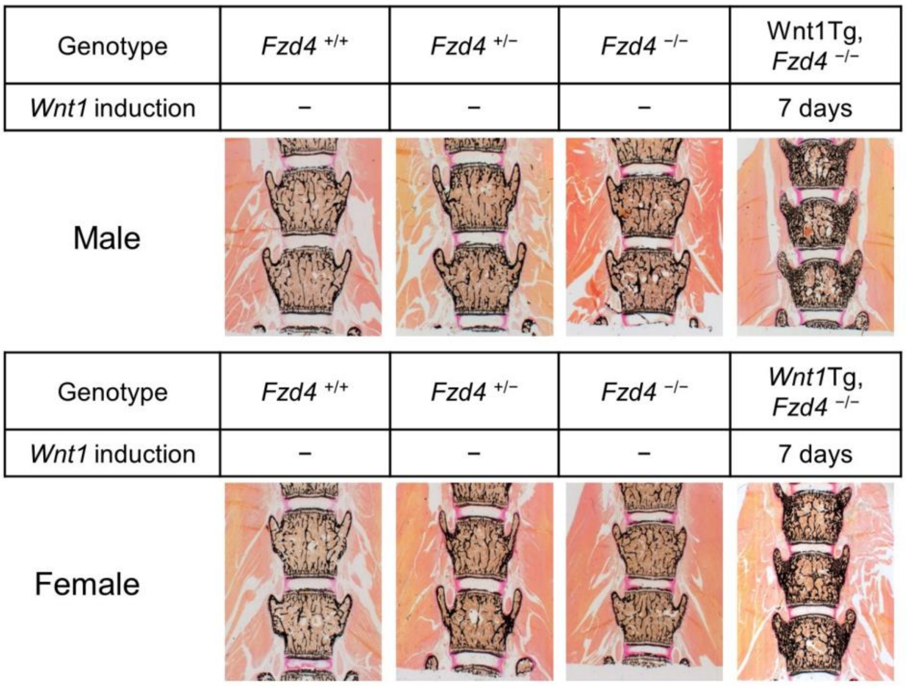

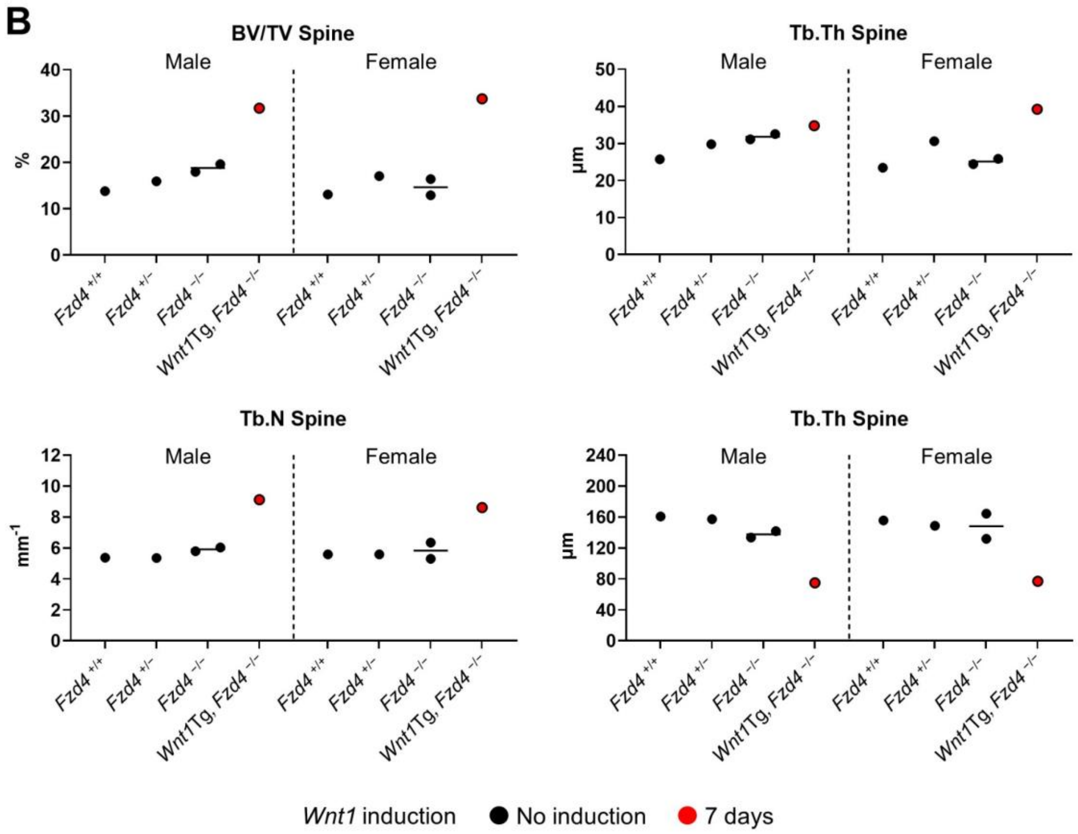

Figure 22. Preliminary investigation of the influence of *Fzd4* deficiency on WNT1-induced trabecular bone formation in vertebral bodies. (A) Representative images of undecalcified sections of vertebral bodies L3 and L4 with von Kossa/van Gieson staining from male and female *Fzd4* $^{+/+}$, *Fzd4* $^{+/-}$, *Fzd4* $^{-/-}$ and *Fzd4* $^{-/-}$ mice carrying the osteoblast-specific inducible *Wnt1* transgene with no or 7 days of the *Wnt1* gene induction until sacrifice at the age of 5 weeks. (B) Results of structural histomorphometry performed on the trabecular compartment of vertebral bodies L3 and L4, including bone volume per tissue volume (BV/TV), trabecular thickness (Tb.Th), trabecular number (Tb.N) and trabecular separation (Tb.Sp). Data were not analyzed statistically due to the low number of samples. n=1 or 2 as represented by individual data points.

3.23 Influence of *Fzd2* knockdown on the responsiveness of ST2 cells to reWNT1/SFRP1

To search for alternative WNT1 receptors, firstly I considered FZD2 as a candidate. In fact, pathogenic variants of FZD2 cause dysfunction of WNT-signaling and subsequently result in autosomal-dominant omodysplasia type 2, which is a rare skeletal dysplasia characterized by shortened humeri, short first metacarpals, craniofacial dysmorphism, radial head dislocation as well as genitourinary anomalies [71,72]. Since FZD2 is essential for the development of proper skeletal morphology, preliminarily cell culture experiements were performed to investigate if FZD2 is also involved with the effect of WNT1 on bone formation. Therefore, the *Fzd2* gene was knocked down in ST2 cells utilizing esiRNA. Reverse transfection was performed and maintained for 3 days, followed by the stimulation of reWNT1/SFRP1 or reSFRP1 with PBS as negative control for 6h. Gene expression of *Fzd2*, *Apcdd1* and *Omd* was measured by subsequent qRT-PCR. *Fzd2* expression was significantly reduced to a large extent (approx. 75%), indicating a successful gene knockdown (Fig.23 left panel). After reWNT1/SFRP1 administration, the expression of *Fzd2* in control group significantly increased compared to the PBS treated control cells (Fig.22 left panel). *Apcdd1* and *Omd* were significantly induced by reWNT1/SFRP1 in the control group, which is in line with the previous cell culture results (Fig.1C). Most importantly, when *Fzd2* was knocked down, *Apcdd1* and *Omd* induction was even higher in response to reWNT1/SFRP1 stimulation (Fig.23 middle and right panels). In addition, *Omd* expression could be significantly induced by the knockdown of *Fzd2* alone (Fig.23 right panel). Taken together, FZD2 could be preliminarily excluded as the receptor for WNT1 in ST2 cells. On the contrary, FZD2 might even be a negative regulator of WNT1-signaling.

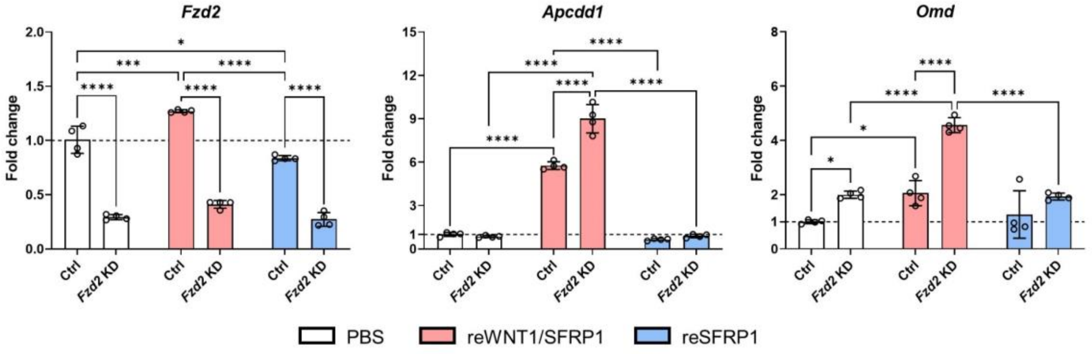

Figure 23. Influence of *Fzd2* knockdown on the responsiveness to reWNT1/SFRP1 of ST2 cells. Expression analysis of *Fzd2*, *Apcdd1* and *Omd* after stimulation with either PBS, reWNT1/Sfrp1 or reSFRP1 for 6h on ST2 cells transfected with Fzd2 esiRNA or a negative control siRNA as measured by qRT-PCR. Expression levels are normalized

to the PBS treated control group. Data were analyzed by one-way ANOVA with Tukey's multiple comparison test. $n=4$ for each group. * $p < 0.05$, *** $p < 0.001$, **** $p < 0.0001$.

4. Discussion

Numerous studies have demonstrated that WNT1 is essential for skeletal integrity. Pathogenic variants of WNT1 result in either early-onset osteoporosis (EOOP) or osteogenesis imperfecta (OI) in patients. These phenotypes could also be recapitulated in the corresponding mouse models [24,25]. In contrast, the activation of transgenic *Wnt1* in osteoblasts leads to a rapid and significant increase of bone mass in mice [23,25]. However, the underlying mechanism of the bone-anabolic effect of WNT1 is still not fully elucidated. Moreover, current treatments to EOOP, OI and osteoporosis are not always effective enough and have their individual limitations or side effects [15,73,74]. Therefore, the investigation of the detailed cellular and molecular mechanism is extremely valuable, since this can potentially provide new insights into the WNT-signaling system, and may enable the development of novel therapeutic approaches for skeletal diseases.

Based on the findings of my medical doctorate dissertation, I hypothesized OMD and POSTN as potential downstream targets of WNT1 in bone formation [14]. Therefore, in the present thesis, my first aim was to test this theory with a focus on OMD. Since the receptors on the membrane are indispensable for the functioning of WNT-signaling, I already performed investigations in my medical doctorate dissertation to screen for the receptor for WNT1 in bone formation and have hypothesized that FZD4 could be a potential receptor for WNT1 [14]. Thus, my second aim was to continue testing this hypothesis and/or to screen for othe responsible receptors. In addition to the WNT ligands and their receptors, there are other important factors involved into the regulation of WNT-signaling, such as secreted frizzled-related proteins (SFRPs) and WNT inhibitory factor 1 (WIF1) [13,15]. Based on the previous findings as introduced before, the third aim of this thesis is to investigate if SFRP1 is necessary for the osteoanabolic effect of WNT1.

4.1 WNT1-regulated response in ST2 cells

My previous experiments demonstrated that *Omd* and *Postn* are among the most highly induced genes (fold change > 5 times) in ST2 cells after 6h of stimulation by reWNT1/SFRP1 as measured by microarray-based whole transcriptome analysis [14]. Furthermore, another microarray expression analysis revealed that *Omd*, *Postn* as well as *Aspn* are the most highly induced genes in ST2 cells five days after transfection with a wildtype *Wnt1* expression plasmid (Fig.1A). Therefore, these three genes were selected as potential downstream targets of WNT1 for further consideration. Importantly, *Omd* was already significantly induced by reWNT1/SFRP1 stimulation after only 2h along with *Apcdd1*, a well-established downstream target gene of canonical WNT-signaling [64,65]. Moreover, *Omd*, *Postn* and *Apcdd1* could also be significantly induced after 6h of stimulation in ST2 cells by reWNT3a, which is an established canonical WNT ligand [12,66]. In contrast, *Aspn* was not induced by reWNT1/SFRP1 or reWNT3a, but by reWNT5a, an established non-canonical WNT ligand [67]. These findings indicate that *Omd* and *Postn* were directly induced through canonical WNT-signaling, while *Aspn* is presumably not a direct downstream target of WNT1. Instead, the induction of *Aspn* 5 days after transfection was rather a secondary response during the longer induction of WNT1. In addition, an *in silico* analysis using ConTra v3 system [68] for 1kb region upstream of the *Omd* transcription start site (TSS) indicated five potential binding sites of the transcription factors TCF/LEF of canonical WNT-signaling (Fig. 2).

4.2 Investigation of OMD as a potential downstream target of WNT1

When comparing multiple tissues, the expression of *Omd* displayed relatively higher skeletal specificity compared to *Postn* and *Aspn* (Fig.3), and the expression progressively increased during osteogenic differentiation in calvarial osteoblasts (Fig.4A), which is consistent with previous studies [38,41,49,50]. Additionally, the function of POSTN in regulating cortical bone architecture has already been investigated thoroughly [30]. In contrast, so far there is limited knowledge of the *in vivo* function of OMD. Importantly, previous studies indicated that OMD is able to reduce the diameter and heterogeneity of collagen I fibrils *in vitro* [31,48]. Based on these findings, OMD is potentially a downstream effector of WNT1 regulating the assembly of type I collagen fibrils during bone formation. Since the defect of normal type I collagen results in bone fragility in classical OI such as type I and II [75-77], the ability of OMD to regulate assembly of collagen I fibrils might help to explain the bone fragility in the mouse model carrying a G177C variation of *Wnt1* that results in osteogenesis imperfacta type XV [25]. Therefore, I selected OMD as the main target of investigation for this thesis.

4.2.1 Extensive evaluation of the skeletal phenotype of *Omd*-deficient mice

Before investigating the effect of OMD on the osteoanabolic function of WNT1, it was essential to elucidate the function of OMD in skeleton. At the time when the investigations presented in this thesis were conducted, the *in vivo* function of OMD had not been reported. Only recently, one study was published where the researchers mainly focused on the function of OMD in the context of osteoarthritis (OA) utilizing *Omd*-deficient and *Omd*-overexpressing mouse models [56]. In order to obtain more insights into the *in vivo* function of OMD, a thorough investigation of the skeletal phenotype of *Omd*-deficient mice was therefore performed in this thesis.

Of note, µCT analysis of the long bones demonstrated a highly unusual slender bone phenotype in *Omd*-deficient mice that display significantly reduced diaphyseal inner and outer diameter of femora, tibiae and humeri, resulting in decreased transversal size, without influencing cortical porosity or overall bone length. Cortical thickness was only slightly but significantly increased in femora and tibiae in 12-week-old female *Omd*-deficient mice. Since the increase was not observed in other analyzed ages, this difference might be caused by random variation or a transient effect of *Omd* deficiency on cortical bone. This phenotype is reminiscent of skeletal disorders such as osteogenesis imperfecta, osteocraniostenosis and 3-M syndrome that can manifest with slender long bones. However, these diseases are often accompanied by more severe skeletal symptoms such as bone deformity, spontaneous fractures, altered bone mass, etc. [77-79]. Therefore, the slender bone phenotype of long bones caused by OMD deficiency can be considered rather unique.

Evaluation of the general morphological parameters revealed that body length was not influenced by *Omd* deficiency, which is in line with the unchanged long bone length and growth plate thickness of tibiae. In the other study on *Omd*-deficient mice, Zappia *et al.* observed moderately higher thickness of tibial growth plate in 16-month-old male *Omd*-deficient mice compared to wildtype controls, but not in younger ones [56], which is consistent with my findings. However, they did not observe any significant difference regarding body and long bone length [56].

Structural histomorphometry of vertebral bodies and tibiae as well as µCT analysis of the trabecular compartment in femora indicated that *Omd* deficiency does not influence the trabecular bone mass in any analyzed group. Similarly, the study by Zappia *et al.* demonstrated that BV/TV of trabecular compartment in proximal tibial metaphysis was not significantly altered in *Omd*-deficient male mice compared to wildtype controls up to the age of 16 months [56].

The same study also proposed a model that OMD is able to sequester RANKL in extracellular matrix, thus inhibiting osteoclastogenesis. The absence of OMD could induce uncoupled bone remodeling, which leads to increased osteoclastogenesis and subsequently induced bone formation [56]. However, this hypothesis for the binding of OMD to RANKL was only based on *in vitro* experiments. Besides, the level of TRAP in serum was significantly higher in 16-month-old *Omd*-deficient male mice compared to controls, while the P1NP level was not significantly different. This is contradictory with their structural histomorphometric findings by µCT, where BV/TV was not significantly different between *Omd*-deficient and wildtype mice. In my investigation, since there was no significant difference regarding trabecular bone mass in all analyzed conditions, I did not perform cellular histomorphometric analysis to measure the activity of osteoblastogenesis and osteoclastogenesis. Collectively, the cellular mechanism of OMD *in vivo* remains to be explored.

Cell culture results demonstrated that OMD deficiency could not influence the mineralization capacity of bone marrow-derived osteoblasts until day 15 of osteogenic differentiation, which is in line with the analyses of trabecular bone of different sites. In contrast, previous studies observed that knockdown or silencing of *Omd* by siRNA or shRNA in human dental pulp stem cells could significantly decrease the expression of osteogenesis related genes and transcription factors (such as *Dmp1*, *Alpl*, *Sp7* and *Runx2*) as well as the mineralization capacity during osteogenic differentiation [50,52]. However, the effect of OMD on mesenchymal stem cells and dental pulp stem cells is most likely different and it might be worthwhile to evaluate the dental phenotype of OMD-deficient mice in future studies

Interestingly, in my cell culture experiments, expression analysis of osteoblast-associated marker genes by qRT-PCR revealed significantly reduced expression of *Runx2* and *Wnt16* in *Omd*-deficient primary osteoblasts. Considering *Runx2* is an early osteoblast transcription factor, the difference of its expression at this relative late stage may not cause different mineralization in a longer culture of osteoblasts. WNT16 was reported to be involved in the normal development of cortical bone [69], which might explain the connection between OMD deficiency and the subsequently observed change in long bone geometry. However, this hypothesis needs to be verified by more *in vivo* investigations.

The cortical diameter is directly influenced by the cortical bone formation rate. The slender long bone phenotype was not fully developed in *Omd*-deficient mice at 6 weeks of age, but stable from the age of 12 weeks onwards. Moreover, when comparing the age-dependent change of cortical diameters, the change from 12 weeks to 24 weeks of age was similar in both genotypes. These findings indicate that the cortical bone formation might be similar in adult mice but different in young mice. Thus, dynamic histomorphometric analysis of femoral cortical bone was performed in 6-week-old female mice. There was no significant difference regarding all parameters on the endosteal surface. Unfortunately, the periosteal region was partially damaged in some samples, preventing a conclusive evaluation. Therefore, the difference of cortical bone formation could not be determined here due to technical issues. Since frozen sectioning is able to achieve higher integrity of the samples, it may be a better option for this measurement for the future studies.

Since OMD is able to regulate the assembly of collagen I fibrils *in vitro*, it was reasonable to speculate that it can influence the mechanical properties of the bone matrix. Although we observed significantly increased flexural strength in female 12-week-old *Omd*-deficient mice as measured by three-point-bending test, these were expected in the context of different cortical geometry (i.e. cortical thickness and diameters), and are not indicative of altered material properties. Since material stiffness, as well as hardness and modulus measured by nanoindentation were all unchanged, it was concluded that *Omd* deficiency has no influence on the inherent mechanical properties of the bone matrix, at least in the settings tested in this thesis.

Despite the lack of changes in the overall mechanical properties of the bone matrix, nanostructural analysis by atomic force microscopy revealed that *Omd* deficiency led to higher heterogeneity and more loosely packing of collagen fibrils on cortical surfaces. However, since this influence was moderate, it is plausible that the bone material property was not significantly altered, as this heterogeneity did not translate into a difference at microstructural level in polarized microscopy analysis.

In summary, the trabecular architecture was not influenced by *Omd* deficiency. Interestingly and importantly, *Omd* deficiency caused a unique slender long bone phenotype without affecting cortical porosity and longitudinal bone growth. At the nanostructural level, it was found that *Omd* deficiency results in a moderate alteration of collagen fibrils.

4.2.2 The influence of *Omd* deficiency on the osteoanabolic effect of WNT1

As stated above, one of the main aims of my thesis is to investigate if *Omd* deficiency could influence the osteoanabolic effect of WNT1. Apparently, Omd deficiency did not affect the bone formation in both trabecular and cortical bone after the induction of WNT1. Interestingly, when WNT1 was induced, the flexural strength of femora was significantly increased in the absence of OMD as measured by three-point-bending. Since there was no significant difference regarding cortical geometry in this analysis, these results indicated that the bone material property was indeed changed by *Omd* deficiency during WNT1 induction. In contrast, *Omd* deficiency alone did not significantly change bone material properies. Thus, I propose that the potential effect of *Omd* deficiency was amplified by the massive change of bone matrix during WNT1 induction. Therefore, OMD may have a moderate effect on maintaining the inherent bone matrix mechanical properties under specific conditions, such as enhanced bone formation. This may be relevant also in the context of fracture healing, an aspect that may be worthwhile of future investigation.

4.3 Investigation of the putative receptor of WNT1

Screening and verification of the potential receptor of WNT1 was another focus of my thesis. As mentioned before, we speculated that FZD4 acts as a potential receptor for WNT1. A previous study demonstrated that osteoblast-specific deficiency of FZD4 resulted in significantly decreased trabecular bone mass in mouse femora [32]. Considering that WNT1 might also regulate bone anabolism via cells other than osteoblasts, we took advantage of globally *Fzd4*-deficient mice for further investigation. Unfortunately, *Fzd4* deficiency displayed very high lethality in new born mice, which was more severe than previously reported [70]. Therefore, I was not able to collect sufficient mice to perform reliable statistical analyses. Nonetheless, the existing data clearly demonstrate that the deficiency of FZD4 did not impair the bone-anabolic effect of WNT1.

Therefore, I continued screening for the receptor of WNT1. FZD2 is a receptor with known skeletal relevance. Pathogenic variants of FZD2 can lead to autosomal-dominant omodysplasia type 2, a rare skeletal dysplasia characterized by shortened humeri, short first metacarpals, craniofacial dysmorphism, radial head dislocation as well as genitourinary anomalies [71,72]. Although there are some differences between the manifestations and those in the patients carrying pathogenic variants of WNT1, it was still worthwhile to evaluate if FZD2 mediates the osteoanabolic effect of WNT1. Thus, preliminary investigations were performed using siRNA to knockdown *Fzd2* expression in ST2 cells. Interestingly, knockdown of *Fzd2* alone could significantly increase the expression of *Omd*, and reWNT1/SFRP1 stimulation even further significantly induced *Apcdd1* and *Omd* expression when *Fzd2* was knocked down, which indicates that canonical WNT-signaling was further induced. Therefore, FZD2 might even be a negative regulator of WNT1-signaling, although the underlying molecular mechanism has not been investigated.

A recent study identified that WNT7 interacts with brain endothelial cells independent of FZD receptors, through a different receptor termed RECK [80]. For other WNT ligands, it is also possible that they could bind cells independent of FZD receptors. Thus, the search for the relevant receptor for WNT1 in the skeleton may need to be expanded to include potential receptors beyond the FZD family.

4.4 The influence of *Sfrp1* deficiency on WNT1-induced trabecular bone foramtion

To investigate if SFRP1 is necessary for the osteoanabolic function of WNT1 was another aim of my thesis. Here, the data clearly demonstrate that the deficiency of *Sfrp1* did not reduce the bone mass increase after WNT1 induction. While SFRP1 was always classified as an antagonist of WNT-signaling [15,18], it is absolutely essential for the biological activity of recombinant WNT1 *in vitro*. Therefore, the question arose, if a similar function is also present *in vivo*. A previous study observed significantly increased BV/TV in femora and a non-significant tendency towards trabecular bone mass in vertebral bodies of *Sfrp1*-deficient mice older than 35 weeks [81]. In my experiment, no difference was observed regarding trabecular bone mass of vertebral bodies L3 and L4 between female *Sfrp1*-deficient and wildtype mice at the age of 12 weeks. Probably the inhibition of SFRP1 on WNT-signaling is not very strong or relevant at that age so that the absence of SFRP1 was not able to elevate trabecular bone mass in young mice. In addition, *Sfrp1* deficiency did not further enhance bone formation after WNT1 induction. Possible reasons could be that the bone formation activity induced by WNT1 already reached maximum capacity and could not be further promoted, or that SFRP1 was also not expressed under these conditions in wildtype mice.

4.5 Conclusion

In this thesis, I thoroughly evaluated the skeletal phenotype of *Omd*-deficient mice. The trabecular bone was not affected by *Omd* deficiency, while the absence of *Omd* caused a unique slender long bone phenotype characterized by significantly decreased transversal size without influencing the longitudinal bone length or cortical porosity. Moreover, *Omd* deficiency had a moderate influence on the collagen fibrils at the nanostructural level. However, the detailed molecular mechanism of the *in vivo* function of OMD remains to be further investigated. Importantly, my results clearly demonstrated that OMD is not required for the osteoanabolic effect of WNT1.

Furthermore, preliminary findings have excluded FZD4 as the receptor of WNT1 and indicated that FZD2 may act as a negative regulator of WNT1 in ST2 cells. Besides, in contrast to the *in vitro* effect, SFRP1 was not required for the *in vivo* bone-anabolic function of WNT1. Overall, there still remain numerous questions regarding the detailed mechanism of WNT1 in bone formation that warrant further investigations in order to better understand and ultimately modulate this highly relevant pathway.

5. Summary

WNT1 is an essential factor in bone remodeling and critical for skeletal integrity. However, the detailed mechanism of WNT1 in bone anabolism is still unclear. The investigation of the mechanism is able to provide new insights into WNT-signaling system, and potentially enables development of new treatment for skeletal disorders. Based on previous findings, I hypothesized OMD as a downstream target of WNT1 in bone formation and FZD4 as a potential receptor for WNT1. Another aim was to test if SFRP1 is required for the bone anabolic function of WNT1 *in vivo*.

In this thesis, I thoroughly evaluated the skeletal phenotype of *Omd*-deficient mice. The trabecular bone was not affected by *Omd* deficiency, while the absence of *Omd* caused a unique slender long bone phenotype characterized by significantly decreased transversal size without influencing the longitudinal bone length or cortical porosity. Moreover, *Omd* deficiency had a moderate influence on the collagen fibrils at the nanostructural level. However, the detailed molecular mechanism of the *in vivo* function of OMD remains to be further investigated. Importantly, my results clearly demonstrated that OMD is not required for the osteoanabolic effect of WNT1.

Furthermore, preliminary findings have excluded FZD4 as the receptor of WNT1 and indicated that FZD2 may act as a negative regulator of WNT1 in ST2 cells. Besides, in contrast to the *in vitro* effect, SFRP1 was not required for the *in vivo* bone-anabolic function of WNT1. Overall, there still remain numerous questions regarding the detailed mechanism of WNT1 in bone formation that warrant further investigations in order to better understand and ultimately modulate this highly relevant pathway.

6. Zusammenfassung

WNT1 ist ein essentieller Faktor in dem Prozess der Knochenremodellierung und wichtig für die Skelettintegrität. Der genaue Mechanismus von WNT1 im Knochenanabolismus ist jedoch noch nicht vollständig aufgeklärt. Die Untersuchung des Mechanismus kann neue Einblicke in das WNT-Signalsystem liefern und ermöglicht möglicherweise die Entwicklung neuer Behandlungsmethoden für Skeletterkrankungen. Basierend auf früheren Erkenntnissen habe ich OMD als möglichen Effektor von WNT1 bei der Knochenbildung und FZD4 als potenziellen Rezeptor für WNT1 identifiziert. Ein weiteres Ziel war es zu testen, ob SFRP1 für die knochenanabole Funktion von WNT1 in vivo erforderlich ist.

In dieser Arbeit habe ich den Skelettphänotyp von *Omd*-defizienten Mäusen eingehend untersucht. Der trabekuläre Knochen war von der *Omd*-Defizienz nicht betroffen, während das Fehlen von *Omd* in den Röhrenknochen zu einem ungewöhnlichen, schlanken Knochenphänotyp führte, der durch eine deutlich verringerte transversale Größe gekennzeichnet war, ohne Unterschiede in der longitudinalen Knochenlänge oder der kortikale Porosität. Darüber hinaus hatte die *Omd*-Defizienz einen moderaten Einfluss auf die Nanostruktur von Kollagenfibrillen. Der detaillierte molekulare Mechanismus der in vivo-Funktion von OMD muss jedoch noch weiter untersucht werden. Wichtig ist, dass meine Ergebnisse eindeutig zeigten, dass OMD für die osteoanabole Wirkung von WNT1 nicht erforderlich ist.

Darüber hinaus haben vorläufige Ergebnisse FZD4 als Rezeptor von WNT1 ausgeschlossen und darauf hingewiesen, dass FZD2 als negativer Regulator von WNT1 in ST2-Zellen wirken könnte. Im Gegensatz zum in vitro-Effekt war SFRP1 außerdem für die knochenanabole Funktion von WNT1 in vivo nicht erforderlich. Insgesamt bleiben noch zahlreiche Fragen zum detaillierten Mechanismus von WNT1 bei der Knochenbildung offen, die weitere Untersuchungen erfordern, um diesen hochrelevanten Signalweg besser zu verstehen und letztendlich zu modulieren.

7. Abbreviations

AFM	Atomic Force Microscope
Alpl/ALPL	Alkaline phosphatase
Apcdd1	Adenomatosis polyposis coli down-regulated 1 protein
Aspn / ASPN	Asporin
BFR/BS	Bone formation rate
Bglap	Bone gamma-carboxyglutamic acid-containing protein
BMP 2	Bone morphogenetic protein 2
BV/TV	Bone volume/tissue volume
Ct. Por	Cortical porosity
Ct. Th	Cortical thickness
DKK1	Dickkopf-related protein 1
Dlx5	Distal-less homeobox 5
Dmp1	Dentin matrix acidic phosphoprotein 1
Dox	Doxycycline
Dspp	Dentin sialophosphoprotein
EOOP	Early-onset osteoporosis
FZD	Frizzled
LRP	Low density lipoprotein receptor-related protein
MAR	Mineral apposition rate
M-CSF	Macrophage colony-stimulating factor
MS/BS	Mineralizing Surface/Bone Surface
OI	Osteogenesis imperfecta
Omd / OMD	Osteomodulin
OPPG	Osteoporosis-pseudoglioma syndrome
P1NP	Procollagen Type I Intact N-terminal Propeptide
PCR	Polymerase chain reaction
Postn / POSTN	Periostin
qBEI	Quantitative backscattered electron imaging
qRT-PCR	Quantitative real-time PCR
RANKL	Receptor activator of nuclear factor kappa-B ligand
Runx2	Runt-related transcription factor 2
SFRPs	secreted frizzled-related proteins
Sfrp1 / SFRP1	Secreted frizzled related protein-1
siRNA	Small interfering RNA
SLRP	Small leucine-rich repeat proteoglycan
SOST	Sclerostin
Sp7	Transcription factor Sp7
Tb.N	Trabecular number
Tb.Sp	Trabecular separation
Tb.Th	Trabecular thickness
Tb.TMD	Trabecular Tissue mineral density

TCF/LEF	T cell factor/lymphoid enhancer factor
Tnfrsf11b	Tumor necrosis factor receptor superfamily member 11b
Tnfsf11	Tumor necrosis factor ligand superfamily member 11
TRAP	Tartrate-resistant acid phosphatase
VBD	Van Buchem disease
WIF1	WNT inhibitory factor 1
WNT-Ca^{2+} pathway	WNT-calcium pathway
WNT-PCP pathway	WNT-planar cell polarity pathway
αMEM	Minimum Essential Medium Eagle - Alpha Modification

8. References

1. Wein MN, Kronenberg HM. Regulation of Bone Remodeling by Parathyroid Hormone. Cold Spring Harbor perspectives in medicine 2018;8.
2. Datta HK, Ng WF, Walker JA, Tuck SP, Varanasi SS. The cell biology of bone metabolism. Journal of clinical pathology 2008;61:577-87.
3. Berendsen AD, Olsen BR. Bone development. Bone 2015;80:14-8.
4. Fukumoto S, Martin TJ. Bone as an endocrine organ. Trends in endocrinology and metabolism: TEM 2009;20:230-6.
5. Clarke B. Normal bone anatomy and physiology. Clinical journal of the American Society of Nephrology : CJASN 2008;3 Suppl 3:S131-9.
6. Florencio-Silva R, Sasso GR, Sasso-Cerri E, Simoes MJ, Cerri PS. Biology of Bone Tissue: Structure, Function, and Factors That Influence Bone Cells. BioMed research international 2015;2015:421746.
7. Salhotra A, Shah HN, Levi B, Longaker MT. Mechanisms of bone development and repair. Nature reviews Molecular cell biology 2020;21:696-711.
8. Armas LA, Recker RR. Pathophysiology of osteoporosis: new mechanistic insights. Endocrinology and metabolism clinics of North America 2012;41:475-86.
9. Aspray TJ, Hill TR. Osteoporosis and the Ageing Skeleton. Sub-cellular biochemistry 2019;91:453-76.
10. Bilezikian JP, Martin TJ, Clemens TL, Rosen C. Principles of Bone Biology: Elsevier Science; 2019.
11. Maeda K, Kobayashi Y, Koide M, et al. The Regulation of Bone Metabolism and Disorders by Wnt Signaling. International journal of molecular sciences 2019;20.
12. Liu J, Xiao Q, Xiao J, et al. Wnt/beta-catenin signalling: function, biological mechanisms, and therapeutic opportunities. Signal transduction and targeted therapy 2022;7:3.
13. MacDonald BT, Tamai K, He X. Wnt/beta-catenin signaling: components, mechanisms, and diseases. Developmental cell 2009;17:9-26.
14. Zhao W. Molecular control of bone matrix quality by Wnt1 [Doctoral thesis]: University of Hamburg; 2022.
15. Baron R, Kneissel M. WNT signaling in bone homeostasis and disease: from human mutations to treatments. Nature medicine 2013;19:179-92.
16. Clevers H, Nusse R. Wnt/beta-catenin signaling and disease. Cell 2012;149:1192-205.
17. Lerner UH, Ohlsson C. The WNT system: background and its role in bone. Journal of internal medicine 2015;277:630-49.
18. Saito-Diaz K, Chen TW, Wang X, et al. The way Wnt works: components and mechanism. Growth factors 2013;31:1-31.
19. Ng LF, Kaur P, Bunnag N, et al. WNT Signaling in Disease. Cells 2019;8.

20. van Amerongen R, Nusse R. Towards an integrated view of Wnt signaling in development. Development 2009;136:3205-14.
21. Maupin KA, Droscha CJ, Williams BO. A Comprehensive Overview of Skeletal Phenotypes Associated with Alterations in Wnt/beta-catenin Signaling in Humans and Mice. Bone Res 2013;1:27-71.
22. Sebastian A, Loots GG. Genetics of Sost/SOST in sclerosteosis and van Buchem disease animal models. Metabolism: clinical and experimental 2018;80:38-47.
23. Luther J, Yorgan TA, Rolvien T, et al. Wnt1 is an Lrp5-independent bone-anabolic Wnt ligand. Science translational medicine 2018;10.
24. Yorgan TA, Rolvien T, Sturznickel J, et al. Mice Carrying a Ubiquitous R235W Mutation of Wnt1 Display a Bone-Specific Phenotype. Journal of bone and mineral research : the official journal of the American Society for Bone and Mineral Research 2020;35:1726-37.
25. Vollersen N, Zhao W, Rolvien T, et al. The WNT1(G177C) mutation specifically affects skeletal integrity in a mouse model of osteogenesis imperfecta type XV. Bone Res 2021;9:48.
26. Keupp K, Beleggia F, Kayserili H, et al. Mutations in WNT1 cause different forms of bone fragility. American journal of human genetics 2013;92:565-74.
27. Laine CM, Joeng KS, Campeau PM, et al. WNT1 mutations in early-onset osteoporosis and osteogenesis imperfecta. The New England journal of medicine 2013;368:1809-16.
28. Tong J, Kishi H, Matsuda T, Muraguchi A. A bone marrow-derived stroma cell line, ST2, can support the differentiation of fetal thymocytes from the CD4+ CD8+ double negative to the CD4+ CD8+ double positive differentiation stage in vitro. Immunology 1999;97:672-8.
29. Bonnet N, Gineyts E, Ammann P, Conway SJ, Garnero P, Ferrari S. Periostin deficiency increases bone damage and impairs injury response to fatigue loading in adult mice. PloS one 2013;8:e78347.
30. Kudo A. Periostin in Bone Biology. Advances in experimental medicine and biology 2019;1132:43-7.
31. Tashima T, Nagatoishi S, Sagara H, Ohnuma S, Tsumoto K. Osteomodulin regulates diameter and alters shape of collagen fibrils. Biochemical and biophysical research communications 2015;463:292-6.
32. Kushwaha P, Kim S, Foxa GE, et al. Frizzled-4 is required for normal bone acquisition despite compensation by Frizzled-8. Journal of cellular physiology 2020;235:6673-83.
33. de Almeida Magalhaes T, Liu J, Chan C, et al. Extracellular carriers control lipid-dependent secretion, delivery, and activity of WNT morphogens. Developmental cell 2024;59:244-61 e6.
34. Sommarin Y, Wendel M, Shen Z, Hellman U, Heinegard D. Osteoadherin, a cell-binding keratan sulfate proteoglycan in bone, belongs to the family of

leucine-rich repeat proteins of the extracellular matrix. The Journal of biological chemistry 1998;273:16723-9.

35. Wendel M, Sommarin Y, Heinegard D. Bone matrix proteins: isolation and characterization of a novel cell-binding keratan sulfate proteoglycan (osteoadherin) from bovine bone. The Journal of cell biology 1998;141:839-47.

36. Shen Z, Gantcheva S, Sommarin Y, Heinegard D. Tissue distribution of a novel cell binding protein, osteoadherin, in the rat. Matrix biology : journal of the International Society for Matrix Biology 1999;18:533-42.

37. Ramstad VE, Franzen A, Heinegard D, Wendel M, Reinholt FP. Ultrastructural distribution of osteoadherin in rat bone shows a pattern similar to that of bone sialoprotein. Calcified tissue international 2003;72:57-64.

38. Ninomiya K, Miyamoto T, Imai J, et al. Osteoclastic activity induces osteomodulin expression in osteoblasts. Biochemical and biophysical research communications 2007;362:460-6.

39. Sugars RV, Olsson ML, Marchner S, Hultenby K, Wendel M. The glycosylation profile of osteoadherin alters during endochondral bone formation. Bone 2013;53:459-67.

40. Petersson U, Hultenby K, Wendel M. Identification, distribution and expression of osteoadherin during tooth formation. European journal of oral sciences 2003;111:128-36.

41. Nikdin H, Olsson ML, Hultenby K, Sugars RV. Osteoadherin accumulates in the predentin towards the mineralization front in the developing tooth. PloS one 2012;7:e31525.

42. Buchaille R, Couble ML, Magloire H, Bleicher F. Expression of the small leucine-rich proteoglycan osteoadherin/osteomodulin in human dental pulp and developing rat teeth. Bone 2000;27:265-70.

43. Zhu Z, Huang F, Gao M, et al. Osteogenic-Like Microenvironment of Renal Interstitium Induced by Osteomodulin Contributes to Randall's Plaque Formation. Advanced science 2024:e2405875.

44. Skenteris NT, Seime T, Witasp A, et al. Osteomodulin attenuates smooth muscle cell osteogenic transition in vascular calcification. Clinical and translational medicine 2022;12:e682.

45. Goncalves I, Oduor L, Matthes F, et al. Osteomodulin Gene Expression Is Associated With Plaque Calcification, Stability, and Fewer Cardiovascular Events in the CPIP Cohort. Stroke 2022;53:e79-e84.

46. Papadaki V, Asada K, Watson JK, et al. Two Secreted Proteoglycans, Activators of Urothelial Cell-Cell Adhesion, Negatively Contribute to Bladder Cancer Initiation and Progression. Cancers 2020;12.

47. National Center for Biotechnology Information (NCBI), National Library of Medicine (US), National Center for Biotechnology Information. at https://www.ncbi.nlm.nih.gov/gene/27047/?report=expression.)

48. Tashima T, Nagatoishi S, Caaveiro JMM, et al. Molecular basis for

governing the morphology of type-I collagen fibrils by Osteomodulin. Communications biology 2018;1:33.

49. Hamaya E, Fujisawa T, Tamura M. Osteoadherin serves roles in the regulation of apoptosis and growth in MC3T3‑E1 osteoblast cells. International journal of molecular medicine 2019;44:2336-44.

50. Lin W, Zhu X, Gao L, Mao M, Gao D, Huang Z. Osteomodulin positively regulates osteogenesis through interaction with BMP2. Cell death & disease 2021;12:147.

51. Rehn AP, Cerny R, Sugars RV, Kaukua N, Wendel M. Osteoadherin is upregulated by mature osteoblasts and enhances their in vitro differentiation and mineralization. Calcified tissue international 2008;82:454-64.

52. Lin W, Gao L, Jiang W, et al. The role of osteomodulin on osteo/odontogenic differentiation in human dental pulp stem cells. BMC oral health 2019;19:22.

53. Kodama H, Yamasaki A, Nose M, et al. Congenital osteoclast deficiency in osteopetrotic (op/op) mice is cured by injections of macrophage colony-stimulating factor. The Journal of experimental medicine 1991;173:269-72.

54. Wiktor-Jedrzejczak W, Bartocci A, Ferrante AW, Jr., et al. Total absence of colony-stimulating factor 1 in the macrophage-deficient osteopetrotic (op/op) mouse. Proceedings of the National Academy of Sciences of the United States of America 1990;87:4828-32.

55. Rehn AP, Chalk AM, Wendel M. Differential regulation of osteoadherin (OSAD) by TGF-beta1 and BMP-2. Biochemical and biophysical research communications 2006;349:1057-64.

56. Zappia J, Tong Q, Van der Cruyssen R, et al. Osteomodulin downregulation is associated with osteoarthritis development. Bone Res 2023;11:49.

57. Dempster DW, Compston JE, Drezner MK, et al. Standardized nomenclature, symbols, and units for bone histomorphometry: a 2012 update of the report of the ASBMR Histomorphometry Nomenclature Committee. Journal of bone and mineral research : the official journal of the American Society for Bone and Mineral Research 2013;28:2-17.

58. Edgar R, Domrachev M, Lash AE. Gene Expression Omnibus: NCBI gene expression and hybridization array data repository. Nucleic acids research 2002;30:207-10.

59. Oliver WC, Pharr GM. An improved technique for determining hardness and elastic modulus using load and displacement sensing indentation experiments. Journal of Materials Research 1992;7:1564-83.

60. Schneider CA, Rasband WS, Eliceiri KW. NIH Image to ImageJ: 25 years of image analysis. Nature methods 2012;9:671-5.

61. Rezakhaniha R, Agianniotis A, Schrauwen JT, et al. Experimental investigation of collagen waviness and orientation in the arterial adventitia using confocal laser scanning microscopy. Biomechanics and modeling in mechanobiology 2012;11:461-73.

62. Oheim R, Zimmerman K, Maulding ND, et al. Human Heterozygous ENPP1 Deficiency Is Associated With Early Onset Osteoporosis, a Phenotype Recapitulated in a Mouse Model of Enpp1 Deficiency. Journal of bone and mineral research : the official journal of the American Society for Bone and Mineral Research 2020;35:528-39.
63. Faul F, Erdfelder E, Buchner A, Lang AG. Statistical power analyses using G*Power 3.1: tests for correlation and regression analyses. Behavior research methods 2009;41:1149-60.
64. Shimomura Y, Agalliu D, Vonica A, et al. APCDD1 is a novel Wnt inhibitor mutated in hereditary hypotrichosis simplex. Nature 2010;464:1043-7.
65. Hu L, Chen W, Qian A, Li YP. Wnt/beta-catenin signaling components and mechanisms in bone formation, homeostasis, and disease. Bone Res 2024;12:39.
66. Kaur N, Chettiar S, Rathod S, et al. Wnt3a mediated activation of Wnt/beta-catenin signaling promotes tumor progression in glioblastoma. Molecular and cellular neurosciences 2013;54:44-57.
67. Ford CE, Punnia-Moorthy G, Henry CE, et al. The non-canonical Wnt ligand, Wnt5a, is upregulated and associated with epithelial to mesenchymal transition in epithelial ovarian cancer. Gynecologic oncology 2014;134:338-45.
68. Kreft L, Soete A, Hulpiau P, Botzki A, Saeys Y, De Bleser P. ConTra v3: a tool to identify transcription factor binding sites across species, update 2017. Nucleic acids research 2017;45:W490-W4.
69. Moverare-Skrtic S, Henning P, Liu X, et al. Osteoblast-derived WNT16 represses osteoclastogenesis and prevents cortical bone fragility fractures. Nature medicine 2014;20:1279-88.
70. Wang Y, Huso D, Cahill H, Ryugo D, Nathans J. Progressive cerebellar, auditory, and esophageal dysfunction caused by targeted disruption of the frizzled-4 gene. The Journal of neuroscience : the official journal of the Society for Neuroscience 2001;21:4761-71.
71. Saal HM, Prows CA, Guerreiro I, et al. A mutation in FRIZZLED2 impairs Wnt signaling and causes autosomal dominant omodysplasia. Human molecular genetics 2015;24:3399-409.
72. Nagasaki K, Nishimura G, Kikuchi T, et al. Nonsense mutations in FZD2 cause autosomal-dominant omodysplasia: Robinow syndrome-like phenotypes. American journal of medical genetics Part A 2018;176:739-42.
73. Langdahl BL. Overview of treatment approaches to osteoporosis. British journal of pharmacology 2021;178:1891-906.
74. Misof BM, Fratzl-Zelman N. Bone Quality and Mineralization and Effects of Treatment in Osteogenesis Imperfecta. Calcified tissue international 2024.
75. Forlino A, Cabral WA, Barnes AM, Marini JC. New perspectives on osteogenesis imperfecta. Nature reviews Endocrinology 2011;7:540-57.
76. Forlino A, Marini JC. Osteogenesis imperfecta. Lancet 2016;387:1657-71.

77. Marini JC, Forlino A, Bachinger HP, et al. Osteogenesis imperfecta. Nature reviews Disease primers 2017;3:17052.
78. Rosato S, Unger S, Campos-Xavier B, et al. Clinical and Molecular Diagnosis of Osteocraniostenosis in Fetuses and Newborns: Prenatal Ultrasound, Clinical, Radiological and Pathological Features. Genes 2022;13.
79. Clayton PE, Hanson D, Magee L, et al. Exploring the spectrum of 3-M syndrome, a primordial short stature disorder of disrupted ubiquitination. Clinical endocrinology 2012;77:335-42.
80. Eubelen M, Bostaille N, Cabochette P, et al. A molecular mechanism for Wnt ligand-specific signaling. Science 2018;361.
81. Bodine PV, Zhao W, Kharode YP, et al. The Wnt antagonist secreted frizzled-related protein-1 is a negative regulator of trabecular bone formation in adult mice. Molecular endocrinology 2004;18:1222-37.

9. Acknowledgements

First of all, I would like to thank our director Prof. Dr. Michael Amling and my supervisor Prof. Dr. Thorsten Schinke for giving me the opportunity to join this outstanding department five years ago. I spent two years to finish my MD degree and continued for my medical PhD degree here. It was really a happy and unforgettable time to work with the colleagues at the department and the collaborators from other groups. I would like to thank my supervisor Prof. Dr. Thorsten Schinke for the earnest supervision throughout my study, and thank my co-supervisor PD. Dr. Timur Yorgan for all the help on science and daily life. It was a great pleasure to meet and work with my colleagues at AG Schinke. Although Dr. Nannan Liao has finished her work and left our group long time ago, I still want to express my gratitude to her again, for all the help and suggestions for me when I just arrived at Hamburg. And other great colleagues of mine, Dr. Laura Brylka, Dr. Julia Luther, Dr. Armelle Carreau, Mona Neven, Lana Rosenthal, thank you all for the help, and it was very pleasant to work with you all. I also want to thank my colleague Dr. Simon von Kroge, who contributed a lot to our projects. A big thank you to our colleagues at Lottestraße especially Olga Winter and Andrea Thieke for their excellent technical support. Also, many thanks to our secretary Frau Claudia Reymers for always taking care of our administrative issues. In addition, to my new colleague Yihao Zhu, wish you a successful study at IOBM.

I would like to thank my co-colleagues from AG Keller, including Prof. Dr. Dr. Johannes Keller and Dr. Anke Baranowsky for their help. And thank the students at AG Keller especially my friends Shan Jiang and Dr. Weixin Xie for the interesting and helpful communications on science and daily life.

Friends are always a treasure in peoples' life. I am very grateful to all my good friends in Hamburg. Without the friends, life will not be such wonderful and colorful.

Furthermore, I would like to thank my families who always support and encourage me. Thank my roommate, also as a teammate, for supporting me and becoming better together.

Time really flies in these five years. The experience in Hamburg will always be remembered. A new stage of life is coming. Hope myself could be stronger and more knowledgeable in the future.

10. Lebenslauf

Lebenslauf wurde aus datenschutzrechtlichen Gründen entfernt.

11. Eidesstattliche Versicherung

Ich versichere ausdrücklich, dass ich die Arbeit selbständig und ohne fremde Hilfe, insbesondere ohne entgeltliche Hilfe von Vermittlungs- und Beratungsdiensten, verfasst, andere als die von mir angegebenen Quellen und Hilfsmittel nicht benutzt und die aus den benutzten Werken wörtlich oder inhaltlich entnommenen Stellen einzeln nach Ausgabe (Auflage und Jahr des Erscheinens), Band und Seite des benutzten Werkes kenntlich gemacht habe. Das gilt insbesondere auch für alle Informationen aus Internetquellen.

Soweit beim Verfassen der Dissertation KI-basierte Tools („Chatbots“) verwendet wurden, versichere ich ausdrücklich, den daraus generierten Anteil deutlich kenntlich gemacht zu haben. Die „Stellungnahme des Präsidiums der Deutschen Forschungsgemeinschaft (DFG) zum Einfluss generativer Modelle für die Text- und Bilderstellung auf die Wissenschaften und das Förderhandeln der DFG“ aus September 2023 wurde dabei beachtet. Ferner versichere ich, dass ich die Dissertation bisher nicht einem Fachvertreter an einer anderen Hochschule zur Überprüfung vorgelegt oder mich anderweitig um Zulassung zur Promotion beworben habe.

Ich erkläre mich damit einverstanden, dass meine Dissertation vom Dekanat der Medizinischen Fakultät mit einer gängigen Software zur Erkennung von Plagiaten überprüft werden kann.

Datum Unterschrift